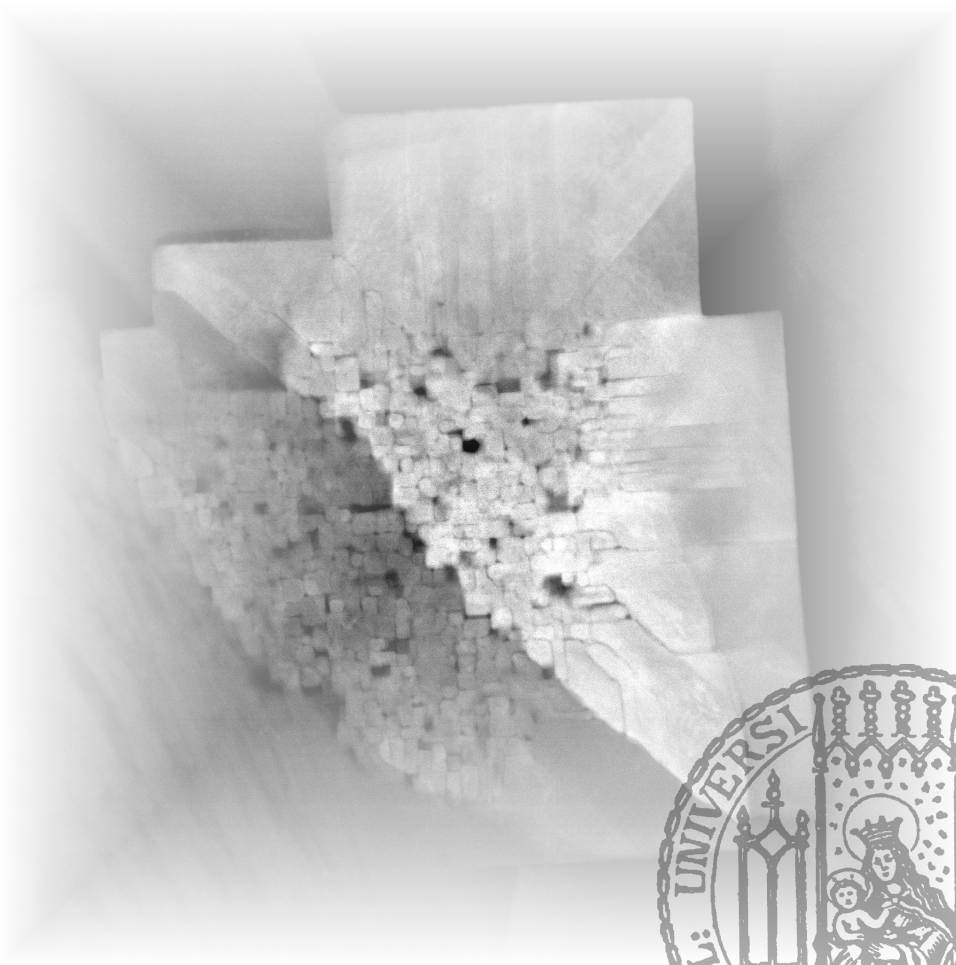

1D TiO₂ Nanostructures Probed by 2D Transmission Electron Microscopy – While Paving the Way for Their 3D Reconstruction

Andreas Wisnet



München 2014

Dissertation zur Erlangung des Doktorgrades
der Fakultät für Chemie und Pharmazie
der Ludwig–Maximilians–Universität München

**1D TiO₂ Nanostructures Probed by
2D Transmission Electron Microscopy
– While Paving the Way for Their
3D Reconstruction**

von
Andreas Wisnet
aus Burghausen, Deutschland

2014

Erklärung

Diese Dissertation wurde im Sinne von §7 der Promotionsordnung vom 28. November 2011 von Frau Prof. Dr. Christina Scheu betreut.

Eidesstattliche Versicherung

Diese Dissertation wurde eigenständig und ohne unerlaubte Hilfe erarbeitet.

München, den 14.11.2014

(Andreas Wisnet)

Dissertation eingereicht am: 14.11.2014

Erstgutachterin: Prof. Dr. Christina Scheu

Zweitgutachter: Prof. Dr. Lukas Schmidt-Mende (Universität Konstanz)

Tag der mündlichen Prüfung: 19.12.2014

Contents

Abstract	ix
1 Introduction	1
Bibliography	4
2 Material and Application	6
2.1 Titanium dioxide	6
2.2 Hybrid Solar Cells	8
Bibliography	9
3 Characterization and Experimental Details	14
3.1 Transmission Electron Microscopy	14
3.2 Electron Tomography	23
3.3 TEM Sample Preparation	27
Bibliography	29
4 Nanoscale Investigation on Large Crystallites in TiO₂ Nanotube Arrays and Implications for High-Quality Hybrid Photodiodes	32
Bibliography	43
5 Model for Hydrothermal Growth of Rutile Wires and the Associated Development of Defect Structures	46
Bibliography	56
6 Defeating Loss Mechanisms in 1D TiO₂-Based Hybrid Solar Cells	59
Concluding Remarks on Pathways to More Efficient Hybrid Solar Cell Devices .	75
Bibliography	76
7 Electron Tomography as Key to the Understanding of Particle Properties at the Nanoscale	78
7.1 DART Reconstruction of a Gold Nanoparticle	78
7.2 Reconstruction of Multiple Iron-Based Particles on Few Trenched Layers of Graphene	82
Bibliography	85

8	Summary and Outlook	87
9	Addendum	90
9.1	Cryfinder	90
9.2	Step-by-Step Instructions for Tomography	92
	Appendix	97

One of the greatest tragedies of life is the murder of a beautiful theory by a gang of brutal facts.
- Benjamin Franklin

Abbreviations

4-MP.....	4-mercaptopyridine
ADF.....	Annular dark field
ART.....	Algebraic reconstruction technique
BF.....	Bright field
BP.....	Backprojection
CBED.....	Convergent beam electron diffraction
CCD.....	Charge-coupled device
CTAB.....	Cetyltrimethylammonium bromide
CTEM.....	Conventional TEM
CTF.....	Contrast transfer function
DART.....	Discrete algebraic reconstruction technique
DDA.....	Discrete dipole approximation
DF.....	Dark field
DSSC.....	Dye-sensitized solar cell
ED.....	Electron diffraction
EDX.....	Energy dispersive X-ray spectroscopy
EELS.....	Electron energy loss spectroscopy
EFTEM.....	Energy filtered TEM
ELNES.....	Energy-loss near edge structure
EMS.....	Electron Microscopy Image Simulation
EQE.....	External quantum efficiency
EXELFS.....	Extended energy-loss fine structure
FBP.....	Filtered backprojection
FEG.....	Field emission gun
FF.....	Fill factor
FFT.....	Fast Fourier transformation
FLG.....	Few-layered graphene
FTO.....	Flourine-doped tin oxide
GUI.....	General user interface
HAADF.....	High-angle annular dark field
HOMO.....	Highest occupied molecular orbital
HR.....	High resolution
HRTEM.....	High resolution TEM
HT.....	High temperature
IRF.....	Instrument Response Function
ITO.....	Tin-doped indium oxide
IS.....	Impedance spectroscopy
LSPR.....	Localized surface plasmon resonance
LUMO.....	Lowest unoccupied molecular orbital
MBA.....	4-mercaptobenzoic acid
NP.....	Nano particle
OD.....	Optical density
OLED.....	Organic light-emitting diode
P3HT.....	Poly(3-hexylthiophene)
PCE.....	Power-conversion efficiency
PEDOT-PSS.....	Poly(3,4-ethylenedioxythiophene)- polystyrenesulfonic acid
PL.....	Photoluminescence spectroscopy
SA(E)D.....	Selected area (electron) diffraction
SEM.....	Scanning electron microscopy
SERS.....	Surface-enhanced Raman spectroscopy
SIRT.....	Simultaneous iterative reconstruction technique

Spiro-OMeTAD	2,2',7,7'-tetrakis-(N,N-di-p-methoxyphenylamine)9,9'-spirobifluorene
ss-DSSC	Solid-state dye-sensitized solar cell
STEM	Scanning TEM
<i>t</i> BP	4- <i>tert</i> -butylpyridine
TCSPC	Time-correlated single photon counting
TEM	Transmission electron microscopy
.....	Transmission electron microscope
TPC	Transient photocurrent decay
TPV	Transient photovoltage decay
UV	Ultraviolet
WBP	Weighted backprojection
XRD	X-ray diffraction

Symbols

<i>a</i> , <i>b</i> , <i>c</i>	Cell parameters
C_s	Spherical aberration coefficient
C_μ	Chemical capacitance
<i>d</i>	Lattice plane spacing
<i>E</i>	Energy
E_{hkl}	Surface energy
δf	Defocus value
<i>hkl</i>	Miller indices
<i>I</i>	Current
I_L	Laser fluence
I_{PL}	Intensity of PL signal
<i>J</i>	Current density
J_{SC}	Short-circuit current density
J_{MP}	Current density at maximum power
k_e	Wave vector
<i>k</i>	Ray of projection
k_{rad}	Radiative decay rate
$k_{non-rad}$	Non-radiative decay rate
<i>L</i>	Camera length
<i>N</i>	Grid points included in a ray
<i>n</i>	Order of diffraction
<i>P</i>	Projection
P_i	Power of incident light
Q_{PL}	PL quantum yield
<i>q</i>	Iteration
<i>R</i>	Intensity/integrated optical density
<i>r</i>	Resolution
R_{Rec}	Recombination resistance
R_S	Series resistance
R_T	Transmission resistance
<i>t</i>	Time
<i>t</i>	Thickness
<i>u</i>	Spatial frequency
uvw	Viewing axis
<i>V</i>	Voltage

$V_{\text{substance}}$	Volume
V_{OC}	Open-circuit voltage
V_{MP}	Voltage at maximum power
x	Position
Z	Atomic number
α	Power law coefficient (Quality factor)
β	Power law coefficient
δf	defocus value
δ_{hkl}	Surface atom density
η	Efficiency
Θ	Bragg angle
λ	Electron wavelength
ρ	Density of pixel/voxel/point
τ	Lifetime
Φ	Phase difference
.....	Tilt angle
ϕ	angle increments
Ψ	Exit wave function of the electron
Ψ_0	Amplitude of the wave function
ω	Weighting factor
ω_e	Angular frequency

Abstract

Hybrid solar cells based on nanoparticulate TiO_2 , dye and poly(3-hexylthiophene) are a common benchmark in the field of solid-state dye-sensitized solar cells. One-dimensionally nanostructured titanium dioxide is expected to enhance power-conversion efficiency (PCE) due to a high surface area combined with a direct path for electrons from the active interface to the back electrode. However, current devices do not meet those expectations and cannot surpass their mesoporous counterparts. This work approaches the problem by detailed investigation of diverse nanostructures on a nanoscale by advanced transmission electron microscopy (TEM). Anodized TiO_2 nanotubes are analyzed concerning their crystallinity. An unexpectedly large grain size is found, and its implication is shown by corresponding solar cell characteristics which feature an above-average fill factor. Quasi-single crystalline rutile nanowires are grown hydrothermally, and a peculiar defect structure consisting of free internal surfaces is revealed. A growth model based on Coulombic repulsion and steric hindrance is developed to explain the resulting V-shaped defect cascade. The influence of the defects on solar cell performance is investigated and interpreted by a combination of TEM, electronic device characterization and photoluminescence spectroscopy, including lifetime measurements. A specific annealing treatment is proposed to counter the defects, suppressing several loss mechanisms and resulting in an improvement of PCEs by 35 %. Simultaneously, a process is developed to streamline electron-tomographic reconstruction of complex nanoparticles. Its suitability is demonstrated by the reconstruction of a gold nanostar and a number of iron-based particles distributed on few-layered graphene.

Note: The animation at the lower right shows the reconstruction of the gold nanostar described in Section 7.1.

Chapter 1

Introduction

What to write for the introduction of a PhD thesis about the inner structure of nanoscopic small particles, which are used, amongst others, in photovoltaics and photocatalysis? There is no doubt that there is an ever growing world wide energy consumption,¹ involving an hitherto pollutive conventional energy supply² which is culminating in the worst possible technology of nuclear power.^{3,4} Not to mention the vision of fusion reactors, which are predicted to be available in 20 to 50 years – a prediction being constantly declared and upheld since the 1940s, although more optimistic statements persist as well.^{5,6} It is evident that, for lack of alternatives or even out of pure rationality, researching renewable energy sources is mandatory. Apart from wind energy, geothermal energy, hydroelectric power and bio energy, there is the ultimate source of renewable energy: solar energy, or, simplified, the sun.^{7,8} There are valid arguments to promote solar energy, like the huge quantity of it reaching the earth every day ($\approx 3 \cdot 10^{15}$ kWh/day at the surface),⁹ or the availability at nearly any place on earth. The production of electricity from solar heat involves considerably more mechanical maintenance¹⁰ than photovoltaics.¹¹ The consequential flexibility of photovoltaic devices renders them a potent candidate to help contain the problem of insufficient energy supply. Alternatively, a solution might be photocatalysis to split water into O_2 and H_2 , or maybe convert CO_2 to CH_4 , providing convenient fuel for fuel cells.¹²⁻¹⁴ To play an important part in the world-wide energy supply, technology has to be driven to the extreme. Silicon-based photovoltaics is on the market for years, but cost and the exorbitant demand for resources dampen its distribution.¹¹ How to solve these problems?

Enter Nanotechnology.

Granted, nanotechnology has been around some decades now, but with the beginning of the new millennium development on this field inexorably accelerated.¹⁵ The most important characteristic of nanostructured materials with regard to large-scale application is its strongly enhanced surface area.¹⁶ Thereby, the thickness of working layers of a device can be significantly reduced, resulting in an equally reduced consumption of material. In this regard, solar cell research has been considerably affected by the implementation of



the dye-sensitized solar cell (DSSC) by O'Regan and Grätzel in 1991,¹⁷ which opened the possibility to fabricate solar cells at considerably decreased costs in comparison to Si-based devices.^{18,19} The underlying combination of nanostructured metal-oxide electrode, dye and electrolyte has been open for steady advancement since. In particular, the exchange of the liquid electrolyte for solid organics lead to all-solid-state dye-sensitized solar cells (ss-DSSCs), which are hybrid solar cells due to the combination of inorganic and organic materials.²⁰ The originally implemented metal-oxide was titanium-dioxide (TiO_2), and still is in many cases. Morphologies for solar cells are still dominated by randomly arranged particles in mesoporous films, as their surface is maximized and the complexity of synthesis minimized this way.²¹ At the same time, bottom-up approaches are devised which can grow a remarkable variety of semi-ordered and/or arrayed geometries.²² The way for this development was paved by adding larger single-crystalline particles like nanorods to the mesoporous matrix.²³ However, as all these methods of fabrication are contrived and advanced, the performance of the resulting morphology has to be tested. First of all, devices are built, measured and evaluated. But before conclusions for the next generation of a device can be drawn, it is important to understand, why it is working – or not working – the way it is. Apart from electrical characterization, a whole range of examination methods is at hand, like X-ray diffraction (XRD), scanning electron microscopy (SEM) or photoluminescence spectroscopy (PL). However, there is one method which stands out as it is able to give information about morphology, crystallinity and chemistry in an unequaled quality, even on a most local scale: Transmission electron microscopy (TEM).²⁴ Finishing this chain of thought, using in-depth TEM is the obvious choice to analyze nanostructures and understand their performance.

And yet, other points should also be emphasized. Most scientists have an urge to learn. Having a TEM at hand is a most intriguing aspect when taking a look at the world. The possibility to determine size and shapes of particles and structures which can not be resolved by light, let alone with the naked eye.²⁵ Seeing the periodicity of a crystal, the fascinating homogeneity of matter squeezed into shape by physical forces on an atomic scale.²⁶ Being able to determine the exact position of elements in a crystal lattice, and their interactions within a confined space.^{27,28} This is why we do science. We want to understand. And we want to be amazed.

Aim of the Thesis

Still, there is purpose. The aim of this thesis is to understand why hybrid solar cells based on one-dimensionally arrayed TiO_2 electrodes still do not live up to the expectations. Whether anatase nanotubes or rutile nanowires, the arrays are deemed to provide "electron highways" from active interfaces to substrates.²⁹ However, the according devices with a $\text{TiO}_2/\text{dye}/\text{P3HT}^{\text{i}}$ setup are stuck at approx. 2 % power-conversion efficiency while their mesoporous counterparts reach up to 3.2 %.³⁰ Transmission electron microscopy

ⁱpoly(3-hexylthiophene)

is applied in various ways, with a focus on high-resolution TEM and scanning TEM to understand the crystal properties of nanotubes and nanowires on an atomic scale. Special attention is devoted to the investigation of features like grain boundaries, which can interfere with charge transport and can not be investigated concerning their atomic arrangement by methods like XRD or SEM. Based on this analysis, a growth mechanism for rutile nanowires is developed to explain the formation of internal surfaces which have a detrimental effect on devices. These effects are then investigated with a focus on performance of hybrid solar cells. Finally, ways are devised to remove these defects and their effectiveness is proven.

Additionally, reconstructions of electron-tomography series are performed. A process sequence is developed to obtain high-quality tomograms, which were in part used for subsequent calculations of an electro-optical response by cooperators. This work on electron tomography is intended as a starting point for future reconstructions of TiO_2 based systems.

Outline of the Thesis

Following the introduction, Chapter 2 gives an overview of TiO_2 phases and nanostructured morphologies, as well as a short summary about hybrid solar cells. Chapter 3 provides a basic understanding of TEM techniques, such as conventional TEM (CTEM) imaging modes, scanning TEM (STEM) and chemical analysis, and electron tomography, including acquisition, reconstruction algorithms and a code of practice. Chapter 4 is a study on crystal sizes within TiO_2 nanotube arrays which were fabricated by anodization, as well as their influence on device performance. Chapter 5 explains the nature of defects found in hydrothermally-synthesized rutile nanowires, i.e. a finger structure caused by free internal surfaces. Hereupon, a growth model is developed which is based on a partly Coulombic, partly steric hindrance during growth. Chapter 6 shows the detrimental influence of the aforementioned defects on device performance and suggests a solution based on annealing at elevated temperatures, increasing device performance by 35 %. The details about two tomographic reconstructions and their results are given in Chapter 7. One is a gold nanostar, whose morphology was then correlated to its optical properties, and the second is a sample of few-layered graphene which has been catalytically treated by Fe-based nanoparticles. After the Summary and Outlook in Chapter 8, the Addendum in Chapter 9 provides a description of "cryfinder", a program written to reliably calculate and find possible lattice planes for values extracted from TEM data of given materials. Furthermore, there are detailed step-by-step instructions to obtain DART reconstructions from projection series.



Bibliography

- [1] BP, “Statistical Review of World Energy 2014.” <http://www.bp.com/content/dam/bp/pdf/Energy-economics/statistical-review-2014/BP-statistical-review-of-world-energy-2014-full-report.pdf>, 2014. [Online; accessed 16-October-2014].
- [2] U.S. Energy Information Administration, “Carbon Dioxide Emissions From Energy Consumption by Source.” http://www.eia.gov/totalenergy/data/monthly/pdf/sec12_3.pdf, 2014. [Online; accessed 16-October-2014].
- [3] Greenpeace International, “Nuclear Power: dirty, dangerous and expensive.” <http://www.greenpeace.org/usa/PageFiles/391717/Nuclear%20Power.pdf>, 2014. [Online; accessed 16-October-2014].
- [4] K. Stierstadt, *Atommüll - wohin damit?* Harri Deutsch 2010, 2nd ed., 2010.
- [5] National Resources Defense Council, C. E. Paine and M. McKinzie, “When Peer Review Fails – The Roots of the National Ignition Facility (NIF) Debacle.” <http://www.nrdc.org/nuclear/nif2/findings.asp>, 2014. [Online; accessed 16-October-2014].
- [6] FuseNet, “Lockheed Martin announces compact Fusion Reactor plans.” <http://www.fusenet.eu/node/400>, 2014. [Online; accessed 16-October-2014].
- [7] D. Ginley, M. A. Green, and R. Collins, “Solar energy conversion toward 1 terawatt,” *MRS Bulletin*, vol. 33, pp. 355–364, 4 2008.
- [8] F. Manzano-Agugliaro, A. Alcayde, F. Montoya, A. Zapata-Sierra, and C. Gil, “Scientific production of renewable energies worldwide: An overview,” *Renewable and Sustainable Energy Reviews*, vol. 18, pp. 134 – 143, 2013.
- [9] Institut für Wärmetechnik, TU Graz, “Sonnenenergienutzung.” http://lamp.tu-graz.ac.at/~iwt/downloads/skripten/Teil2_Grundlagen.pdf, 2014. [Online; accessed 14-October-2014].
- [10] B. Dobritzsch, M. Gehling, and S. Ackermann, “Solarthermische Kraftwerke.” http://www.gehl-ing.de/papers/MasterEE_Projektarbeit_SolarthermischeKraftwerke.pdf, 2009. [Online; accessed 16-October-2014].
- [11] M. A. Green, “Third generation photovoltaics: Ultra-high conversion efficiency at low cost,” *Progress in Photovoltaics: Research and Applications*, vol. 9, no. 2, pp. 123–135, 2001.
- [12] A. Mills and S. L. Hunte, “An overview of semiconductor photocatalysis,” *Journal of Photochemistry and Photobiology A: Chemistry*, vol. 108, no. 1, pp. 1–35, 1997.
- [13] A. Dhakshinamoorthy, S. Navalon, A. Corma, and H. Garcia, “Photocatalytic CO₂ reduction by TiO₂ and related titanium containing solids,” *Energy & Environmental Science*, vol. 5, pp. 9217–9233, 2012.
- [14] S. N. Habisreutinger, L. Schmidt-Mende, and J. K. Stolarczyk, “Photocatalytic reduction of CO₂ on TiO₂ and other semiconductors,” *Angewandte Chemie International Edition*, vol. 52, no. 29, pp. 7372–7408, 2013.
- [15] Y. Dang, Y. Zhang, L. Fan, H. Chen, and M. Roco, “Trends in worldwide nanotechnology patent applications: 1991 to 2008,” *Journal of Nanoparticle Research*, vol. 12, no. 3, pp. 687–706, 2010.
- [16] F. Rosei, “Nanostructured surfaces: challenges and frontiers in nanotechnology,” *Journal of Physics: Condensed Matter*, vol. 16, no. 17, p. S1373, 2004.
- [17] B. O’Regan and M. Grätzel, “A low-cost, high-efficiency solar cell based on dye-sensitized colloidal TiO₂ films,” *Nature*, vol. 353, pp. 737–740, 1991.
- [18] M. Grätzel, “Dye-sensitized solar cells,” *Journal of Photochemistry and Photobiology C: Photochemistry Reviews*, vol. 4, no. 2, pp. 145–153, 2003.
- [19] B. E. Hardin, H. J. Snaith, and M. D. McGehee, “The renaissance of dye-sensitized solar cells,” *Nature Photonics*, vol. 6, pp. 162–169, 2012.
- [20] S. Günes and N. S. Sariciftci, “Hybrid solar cells,” *Inorganica Chimica Acta*, vol. 361, no. 3, pp. 581–588, 2008.

-
- [21] H. J. Snaith and L. Schmidt-Mende, "Advances in liquid-electrolyte and solid-state dye-sensitized solar cells," *Advanced Materials*, vol. 19, no. 20, pp. 3187–3200, 2007.
- [22] Y. Ye, C. Jo, I. Jeong, and J. Lee, "Functional mesoporous materials for energy applications: solar cells, fuel cells, and batteries," *Nanoscale*, vol. 5, pp. 4584–4605, 2013.
- [23] T.-W. Zeng, H.-H. Lo, C.-H. Chang, Y.-Y. Lin, C.-W. Chen, and W.-F. Su, "Hybrid poly (3-hexylthiophene)/titanium dioxide nanorods material for solar cell applications," *Solar Energy Materials and Solar Cells*, vol. 93, no. 6-7, pp. 952–957, 2009.
- [24] K. Durose, S. E. Asher, W. Jaegermann, D. Levi, B. E. McCandless, W. Metzger, H. Moutinho, P. Paulson, C. L. Perkins, J. R. Sites, G. Teeter, and M. Terheggen, "Physical characterization of thin-film solar cells," *Progress in Photovoltaics: Research and Applications*, vol. 12, no. 2-3, pp. 177–217, 2004.
- [25] R. Leary, P. A. Midgley, and J. M. Thomas, "Recent advances in the application of electron tomography to materials chemistry," *Accounts of Chemical Research*, vol. 45, no. 10, pp. 1782–1791, 2012.
- [26] J. Meurig Thomas and P. A. Midgley, "High-resolution transmission electron microscopy: the ultimate nanoanalytical technique," *Chemical Communications*, pp. 1253–1267, 2004.
- [27] R. Wirth, "Focused ion beam (FIB) combined with SEM and TEM: Advanced analytical tools for studies of chemical composition, microstructure and crystal structure in geomaterials on a nanometre scale," *Chemical Geology*, vol. 261, no. 3-4, pp. 217–229, 2009.
- [28] S. Venkatesan, M. H. Madsen, H. Schmid, P. Krogstrup, E. Johnson, and C. Scheu, "Direct observation of interface and nanoscale compositional modulation in ternary III-As heterostructure nanowires," *Applied Physics Letters*, vol. 103, no. 6, 2013.
- [29] J. Tian, Z. Zhao, A. Kumar, R. I. Boughton, and H. Liu, "Recent progress in design, synthesis, and applications of one-dimensional TiO₂ nanostructured surface heterostructures: a review," *Chemical Society Reviews*, vol. 43, pp. 6920–6937, 2014.
- [30] P. Docampo, S. Guldin, T. Leijtens, N. K. Noel, U. Steiner, and H. J. Snaith, "Lessons learned: From dye-sensitized solar cells to all-solid-state hybrid devices," *Advanced Materials*, vol. 26, no. 24, pp. 4013–4030, 2014.



Chapter 2

Material and Application

2.1 Titanium dioxide

TiO₂ is a semiconductor with a band gap of around 3 eV, depending on its crystal modification.¹ Low-cost production and non-toxicity enable a wide range of applications as photocatalyst,²⁻⁴ electrode in devices⁵ and others,^{6,7} even as food additive E171.⁸ In the past decades, special interest arose in nanostructuring of TiO₂.⁹⁻¹¹

Crystal Modifications and Material Properties

Titanium dioxide mainly appears in three bulk phases: **anatase**, **rutile** and **brookite**. Apart from that, extreme temperature and pressure may induce additional metastable phases with stoichiometric or substoichiometric composition.¹⁴ Rutile is the stable phase of TiO₂, while anatase and brookite represent metastable phases with phase transformations to rutile for bulk material around ≈ 1090 °C and ≈ 930 °C, respectively.¹⁵ Thin film TiO₂ can be transformed from an amorphous

Table 2.1: Crystal parameters of the three phases of TiO₂ with lattice parameters a, b and c in Å.^{12,13}

	Anatase	Rutile	Brookite
Crystal symmetry	tetragonal	tetragonal	orthorhombic
a	3.80	4.59	9.18
b	3.80	4.59	5.43
c	9.44	2.96	5.16

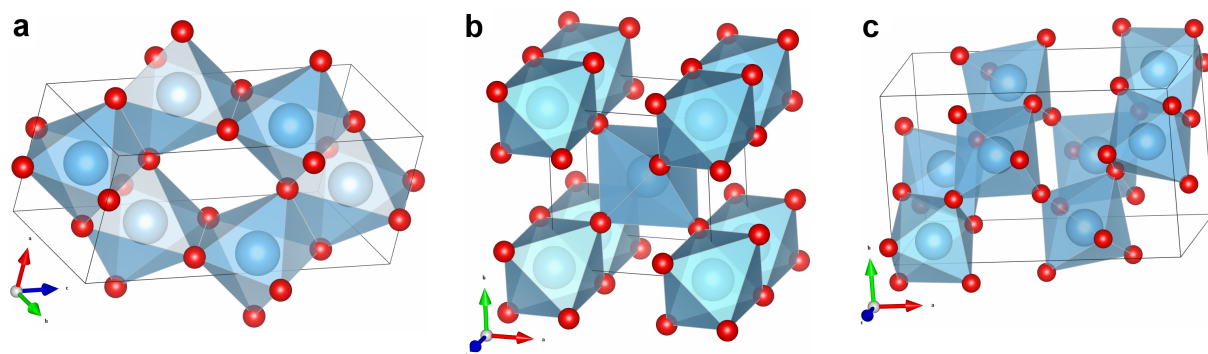


Figure 2.1: Main crystal phases of TiO₂, showing Ti atoms (blue) surrounded by O atoms (red) forming typical octahedrons. a) anatase, b) rutile and c) brookite.

state to anatase beginning at 400 °C and starts to transform into rutile at 800 °C.¹⁶ This roughly also applies to TiO₂ nanoparticles.¹⁷ Figure 2.1 shows that all three of the main crystal modifications are based on octahedrons formed by a Ti atom surrounded by six O atoms. Different alignment of these octahedrons lead to tetragonal (anatase, rutile) and orthorhombic (brookite) crystal symmetries, as denoted in table 2.1. Focus is generally put on anatase and rutile, while research on brookite is running behind.

As the surface characteristics play a major role for applications, it is important to pay heed to the facets shown at TiO₂ crystals or particles.^{20–22} The most prevalent ones are {101} and {001} for anatase, and {110}, {101} and {001} for rutile.²³ Wulff shapes for anatase and rutile are presented in Figure 2.2.^{18,19} However, it is possible to produce TiO₂ nanoparticles presenting different facets like rutile wires with distinct {111} facets at the tips.^{24–26} Most investigation has been performed on rutile {110} surfaces, as it is most common and suitable for functionalizing, e.g. by organic molecules.^{20,21,27–29} Another important characteristic specifically for devices like solar cells, where charge transport is of capital importance, is the electron mobility. TiO₂ covers a wide range from 10⁻⁵ cm²/Vs for porous anatase³⁰ to 10⁻² cm²/Vs for porous polycrystalline rutile³¹ to 1 cm²/Vs at the maximum for single-crystalline rutile.³¹ Porous TiO₂ films made from sintered nanoparticles are most common for applications like dye-sensitized solar cells,^{32–35} but top-down approaches to obtain single-crystalline porous materials were developed to benefit from higher electron mobilities.³⁶ While rutile features a direct band gap of 3.06 eV, anatase has an indirect band gap of 3.23 eV.³⁷ These values are subject to change when the particle size approaches the nanometer size, primarily due to quantum confinement.^{38–40} The band alignment of adjacent rutile and anatase is still being discussed, with a slight tendency to put the conduction band of anatase ≈0.2 eV above that of rutile.^{41–44}

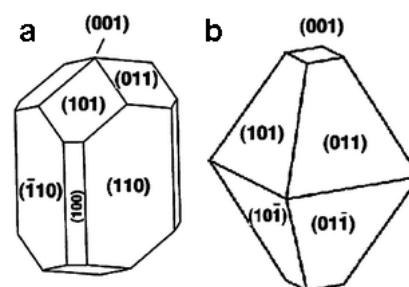


Figure 2.2: Wulff shapes of rutile (a) and anatase (b).^{18,19}

Morphologies and Synthesis Methods

There is a vast number of possibilities to obtain nanostructured TiO₂.⁴⁵ A widespread and straight-forward way is the sintering of nanoparticles like P25 or P123 to obtain a mesoporous TiO₂ film.^{46,47} It has been shown that this starting material consists of anatase and rutile agglomerates, rendering further treatment advisable.⁴⁸ Their large surface area and ease of use makes them a common electrode material for photocatalysis⁴⁹ and dye-sensitized solar cells.^{50,51} However, more sophisticated methods of preparation were developed to enhance surface area, electron transport and even light scattering properties.⁵ Especially for direct charge transport from an interface, where charge separation occurs, to the back electrodes, one-dimensional nanostructures offer evident advantages for solar cell applications.^{52–54} But these structures can also be of use in other devices like

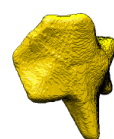


photo-electrochemical cells.^{55,56} 1D TiO_2 nanostructures can be summarized in two categories: nanowires and nanotubes. To obtain free-standing arrays of nanowires, methods involve template-based fabrication,^{57–59} direct oxidation of a Ti foil⁶⁰ and hydrothermal growth.^{61,62} Some of these procedures can also be used to grow nanotubes, for example the template-based synthesis making use of atomic layer deposition,^{63–65} as well as the anodic oxidation of thin Ti foils.⁶⁶

2.2 Hybrid Solar Cells

Many of thin-film solar-cell architectures are competing to dethrone Si-based photovoltaics, whether inorganic, organic or hybrid (organic-inorganic), solid or liquid, with and without dye.⁶⁷ Hybrid solar cells are usually made up from a solid organic p-type semiconductor and a solid inorganic n-type semiconductor.⁵² The most common representative of the latter group clearly is TiO_2 , in all its morphologies discussed above.^{68,69} The p-type semiconductor might be an absorber on its own, like poly(3-hexylthiophene) (P3HT), or dedicated hole conductors like a molecule answering to the unwieldy name of 2,2',7,7'-tetrakis-(N,N-dip-methoxyphenylamine)9,9'-spirobifluorene (Spiro-OMeTAD). Additional layers like organic dyes or inorganic absorbers at the organic/inorganic junction may be applied. Two examples of hybrid solar cells are shown in Figure 2.3a and b. Both are based on a TiO_2 /P3HT junction with an intermediary dye like ruthenium-based Z907 or organic SQ2 for light harvesting.^{70,71} For charge collection, the TiO_2 electrode is connected to a transparent conductive oxide, flourine-doped tin oxide (FTO) on a glass substrate, while the P3HT is in contact with an Ag back electrode. The difference of the two cases is the use of a mesoporous TiO_2 film in Figure 2.3a, which features higher surface area but lower electron mobility due to a multitude of grain boundaries, and one-dimensional TiO_2 wires/tubes in Fig-

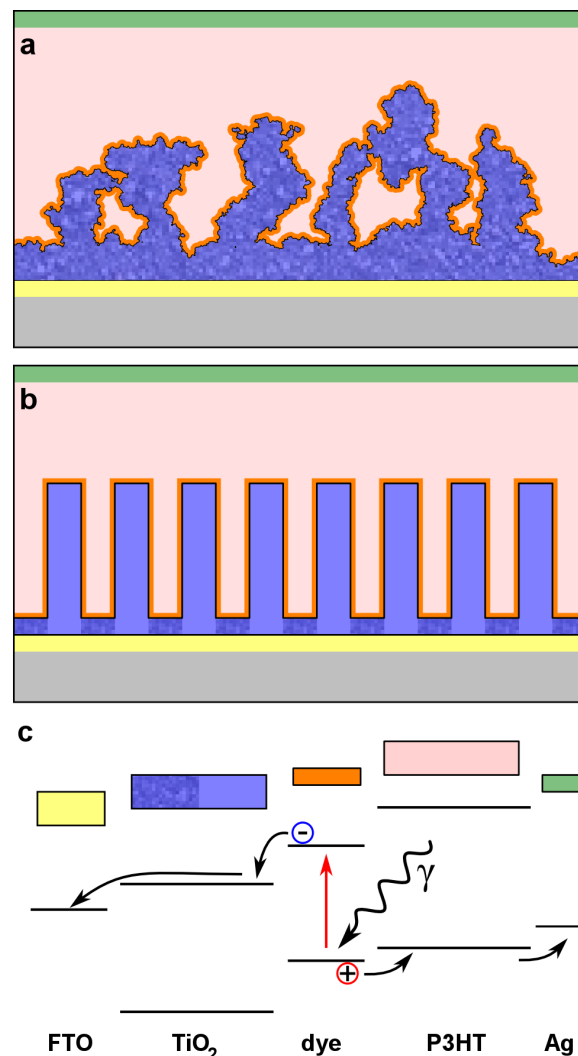


Figure 2.3: Schematics for hybrid solar cells based on mesoporous (a)) and nanowired/nanotubular TiO_2 arrays (b)). c) Gives a schematic of the band alignment for both cases. The γ quantum's energy is of the visible range.

ure 2.3b, which have a lower surface area but feature a direct path for electrons towards the FTO. The principle of the band alignment and thus solar cell functionality, however, are similar in both cases and sketched in Figure 2.3c. Incident light in form of a photon with an energy around 2 eV passes the substrate, FTO and TiO₂ layer (which gives the device the name of an *inverted* solar cell), and gets absorbed by the dye. There it excites an electron, depending on the form of the absorber, either from valence to conduction band (for inorganic absorbers) or from the highest occupied molecular orbital (HOMO) to the lowest unoccupied molecular orbital (LUMO)(for molecular organic absorbers), creating a hole in the valence band or HOMO, respectively. Ideally, an immediate charge separation of the electron-hole pair takes place by injection of the electron into the conduction band of the TiO₂ electrode and transfer of the hole into the valence band of the p-type organic semiconductor (in this case P3HT). The charges are then forwarded to the outer electrodes where they can be collected. Power-conversion efficiencies (PCEs) range around 2.5 % for TiO₂ nanowires/dye/P3HT cells, which was achieved by a core shell structure involving an Sn-doped TiO₂ shell layer.⁷² The highest achieved efficiency with a TiO₂/dye/P3HT combination is 3.2 % with an organic dye and a mesoporous TiO₂ layer.⁷³ The best hybrid solar cell so far was achieved by a mesoporous TiO₂ layer, a Co-based dye and Spiro-OMeTAD with a peak efficiency of 7.2 %.^{69,74}

A final word ought to be written about solar cell characteristics in general. First and foremost, the PCE, or efficiency (η) in short, is used to determine the quality of a given device. It can be extracted from a J-V (current density-voltage) diagram which was taken under standard illumination, as drawn in Figure 2.4.⁷⁵ Related to that are the open-circuit voltage V_{OC} , which is the voltage obtained in a working cell when no current is flowing, and the short-circuit current density J_{SC} , which is obtained while no voltage is present at a working device. The fill factor (FF) is the ratio of the maximum power ($J_{MP} \cdot V_{MP}$) divided by the theoretically possible power ($J_{SC} \cdot V_{OC}$) and is an indicator for loss mechanisms like charge traps and recombination.

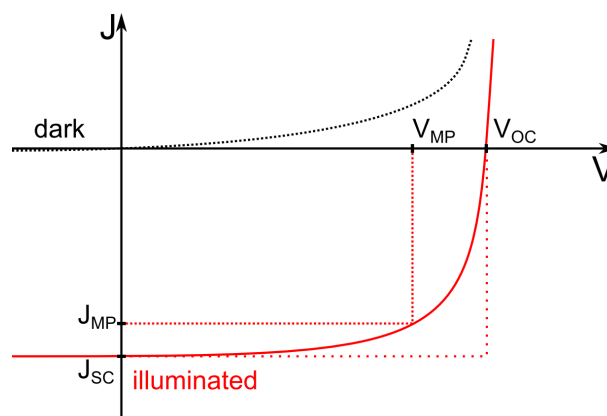
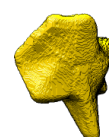


Figure 2.4: Schematic J-V curves of a solar cell with (illuminated) and without (dark) illumination. The important characteristics are open-circuit voltage (V_{OC}), short-circuit current density (J_{SC}) and voltage/current density at maximum power (V_{MP} , J_{MP}).

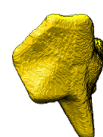
Bibliography

- [1] M. Grätzel and F. P. Rotzinger, “The influence of the crystal lattice structure on the conduction band energy of oxides of titanium(IV),” *Chemical Physics Letters*, vol. 118, no. 5, pp. 474–477, 1985.
- [2] K. Nakata and A. Fujishima, “TiO₂ photocatalysis: Design and applications,” *Journal of Photochemistry and Photobiology C: Photochemistry Reviews*, vol. 13, no. 3, pp. 169–189, 2012.



- [3] S. Banerjee, S. C. Pillai, P. Falaras, K. E. O'Shea, J. A. Byrne, and D. D. Dionysiou, "New insights into the mechanism of visible light photocatalysis," *The Journal of Physical Chemistry Letters*, vol. 5, no. 15, pp. 2543–2554, 2014.
- [4] Y. Ma, X. Wang, Y. Jia, X. Chen, H. Han, and C. Li, "Titanium dioxide-based nanomaterials for photocatalytic fuel generations," *Chemical Reviews*, 2014. doi:10.1021/cr500008u.
- [5] Q. Zhang and G. Cao, "Nanostructured photoelectrodes for dye-sensitized solar cells," *Nano Today*, vol. 6, no. 1, pp. 91–109, 2011.
- [6] J. Bai and B. Zhou, "Titanium dioxide nanomaterials for sensor applications," *Chemical Reviews*, 2014. doi:10.1021/cr400625j.
- [7] T. Rajh, N. M. Dimitrijevic, M. Bissonnette, T. Koritarov, and V. Konda, "Titanium dioxide in the service of the biomedical revolution," *Chemical Reviews*, 2014. doi:10.1021/cr500029g.
- [8] World Health Organization, "Codex Alimentarius." <http://www.codexalimentarius.org>, 2014. [Online; accessed 07-October-2014].
- [9] X. Chen and S. S. Mao, "Titanium dioxide nanomaterials: Synthesis, properties, modifications, and applications," *Chemical Reviews (Washington, DC, U. S.)*, vol. 107, no. 7, pp. 2891–2959, 2007.
- [10] D. Fattakhova-Rohlfing, A. Zaleska, and T. Bein, "Three-dimensional titanium dioxide nanomaterials," *Chemical Reviews*, 2014. doi:10.1021/cr500201c.
- [11] K. Lee, A. Mazare, and P. Schmuki, "One-dimensional titanium dioxide nanomaterials: Nanotubes," *Chemical Reviews*, 2014. doi:10.1021/cr500061m.
- [12] R. Restori, D. Schwarzenbach, and J. R. Schneider, "Charge density in rutile, TiO₂," *Acta Crystallographica Section B*, vol. 43, no. 3, pp. 251–257, 1987.
- [13] I. Djerdj and A. M. Tonejc, "Structural investigations of nanocrystalline TiO₂ samples," *Journal of Alloys and Compounds*, vol. 413, no. 1-2, pp. 159–174, 2006.
- [14] Q.-J. Liu, N.-C. Zhang, F.-S. Liu, and Z.-T. Liu, "Structural, elastic, electronic and optical properties of various mineral phases of TiO₂ from first-principles calculations," *Physica Scripta*, vol. 89, no. 7, p. 075703, 2014.
- [15] T. Mitsuhashi and O. J. Kleppa, "Transformation enthalpies of the TiO₂ polymorphs," *Journal of the American Ceramic Society*, vol. 62, no. 7-8, pp. 356–357, 1979.
- [16] Y. U. Ahn, E. J. Kim, H. T. Kim, and S. H. Hahn, "Variation of structural and optical properties of sol-gel TiO₂ thin films with catalyst concentration and calcination temperature," *Materials Letters*, vol. 57, no. 30, pp. 4660–4666, 2003.
- [17] M. Pal, J. García Serrano, P. Santiago, and U. Pal, "Size-controlled synthesis of spherical TiO₂ nanoparticles: Morphology, crystallization, and phase transition," *The Journal of Physical Chemistry C*, vol. 111, no. 1, pp. 96–102, 2007.
- [18] M. Ramamoorthy, D. Vanderbilt, and R. D. King-Smith, "First-principles calculations of the energetics of stoichiometric TiO₂ surfaces," *Physical Reviews B*, vol. 49, pp. 16721–16727, Jun 1994.
- [19] M. Lazzeri, A. Vittadini, and A. Selloni, "Structure and energetics of stoichiometric TiO₂ anatase surfaces," *Physical Reviews B*, vol. 63, p. 155409, Mar 2001.
- [20] U. Diebold, "The surface science of titanium dioxide," *Surface Science Reports*, vol. 48, no. 5-8, pp. 53–229, 2003.
- [21] T. L. Thompson and J. T. Yates, "Surface science studies of the photoactivation of TiO₂ - new photochemical processes," *Chemical Reviews*, vol. 106, no. 10, pp. 4428–4453, 2006.
- [22] H. G. Yang, C. H. Sun, S. Z. Qiao, J. Zou, G. Liu, S. C. Smith, H. M. Cheng, and G. Q. Lu, "Anatase TiO₂ single crystals with a large percentage of reactive facets," *Nature*, vol. 453, pp. 638–641, 2008.
- [23] A. S. Barnard and L. A. Curtiss, "Prediction of TiO₂ nanoparticle phase and shape transitions controlled by surface chemistry," *Nano Letters*, vol. 5, no. 7, pp. 1261–1266, 2005.
- [24] X. Huang and C. Pan, "Large-scale synthesis of single-crystalline rutile TiO₂ nanorods via a one-step solution route," *Journal of Crystal Growth*, vol. 306, no. 1, pp. 117–122, 2007.

- [25] K. Kakiuchi, E. Hosono, H. Imai, T. Kimura, and S. Fujihara, “{111}-faceting of low-temperature processed rutile TiO₂ rods,” *Journal of Crystal Growth*, vol. 293, no. 2, pp. 541–545, 2006.
- [26] L. Sun, Y. Qin, Q. Cao, B. Hu, Z. Huang, L. Ye, and X. Tang, “Novel photocatalytic antibacterial activity of TiO₂ microspheres exposing 100% reactive {111} facets,” *Chemical Communications*, vol. 47, pp. 12628–12630, 2011.
- [27] G. Lu, A. Linsebigler, and J. T. Yates Jr, “Ti³⁺ defect sites on TiO₂(110): Production and chemical detection of active sites,” *Journal of Physical Chemistry*, vol. 98, pp. 11733–11738, 1994.
- [28] R. Wang, N. Sakai, A. Fujishima, T. Watanabe, and K. Hashimoto, “Studies of surface wettability conversion on TiO₂ single-crystal surfaces,” *The Journal of Physical Chemistry B*, vol. 103, no. 12, pp. 2188–2194, 1999.
- [29] M. A. Henderson, W. S. Epling, C. H. F. Peden, and C. L. Perkins, “Insights into photoexcited electron scavenging processes on TiO₂ obtained from studies of the reaction of O₂ with OH groups adsorbed at electronic defects on TiO₂(110),” *The Journal of Physical Chemistry B*, vol. 107, no. 2, pp. 534–545, 2003.
- [30] T. Dittrich, E. A. Lebedev, and J. Weidmann, “Electron drift mobility in porous TiO₂ (anatase),” *physica status solidi (a)*, vol. 165, no. 2, pp. R5–R6, 1998.
- [31] E. Hendry, M. Koeberg, B. O’Regan, and M. Bonn, “Local field effects on electron transport in nanostructured TiO₂ revealed by terahertz spectroscopy,” *Nano Letters*, vol. 6, no. 4, pp. 755–759, 2006.
- [32] F. Cao, G. Oskam, G. J. Meyer, and P. C. Searson, “Electron transport in porous nanocrystalline TiO₂ photoelectrochemical cells,” *The Journal of Physical Chemistry*, vol. 100, no. 42, pp. 17021–17027, 1996.
- [33] A. Kay and M. Grätzel, “Low cost photovoltaic modules based on dye sensitized nanocrystalline titanium dioxide and carbon powder,” *Solar Energy Materials and Solar Cells*, vol. 44, no. 1, pp. 99–117, 1996.
- [34] S. Yanagida, Y. Yu, and K. Manseki, “Iodine/iodide-free dye-sensitized solar cells,” *Accounts of Chemical Research*, vol. 42, no. 11, pp. 1827–1838, 2009.
- [35] J. Tian, R. Gao, Q. Zhang, S. Zhang, Y. Li, J. Lan, X. Qu, and G. Cao, “Enhanced performance of CdS/CdSe quantum dot cosensitized solar cells via homogeneous distribution of quantum dots in TiO₂ film,” *The Journal of Physical Chemistry C*, vol. 116, no. 35, pp. 18655–18662, 2012.
- [36] E. J. W. Crossland, N. Noel, V. Sivaram, T. Leijtens, J. A. Alexander-Webber, and H. J. Snaith, “Mesoporous TiO₂ single crystals delivering enhanced mobility and optoelectronic device performance,” *Nature*, vol. 495, pp. 215–219, 2013.
- [37] G. Kühn, “Landolt-Börnstein, III: Kristall- und Festkörperphysik, Band 17. Halbleiter: Physik der nicht tetraedrisch gebundenen Elemente und binären Verbindungen: I,” *Crystal Research and Technology*, vol. 19, no. 3, 1984.
- [38] K. M. Reddy, S. V. Manorama, and A. R. Reddy, “Bandgap studies on anatase titanium dioxide nanoparticles,” *Materials Chemistry and Physics*, vol. 78, no. 1, pp. 239–245, 2003.
- [39] C. B. Almquist and P. Biswas, “Role of synthesis method and particle size of nanostructured TiO₂ on its photoactivity,” *Journal of Catalysis*, vol. 212, no. 2, pp. 145–156, 2002.
- [40] N. Satoh, T. Nakashima, K. Kamikura, and K. Yamamoto, “Quantum size effect in TiO₂ nanoparticles prepared by finely controlled metal assembly on dendrimer templates,” *Nature Nanotechnology*, vol. 3, pp. 106–111, 2008.
- [41] T. Kawahara, Y. Konishi, H. Tada, N. Tohge, J. Nishii, and S. Ito, “A patterned TiO₂(anatase)/TiO₂(rutile) bilayer-type photocatalyst: Effect of the anatase/rutile junction on the photocatalytic activity,” *Angewandte Chemie International Edition*, vol. 41, no. 15, pp. 2811–2813, 2002.
- [42] J. Kang, F. Wu, S.-S. Li, J.-B. Xia, and J. Li, “Calculating band alignment between materials with different structures: The case of anatase and rutile titanium dioxide,” *The Journal of Physical Chemistry C*, vol. 116, no. 39, pp. 20765–20768, 2012.



- [43] V. Pfeifer, P. Erhart, S. Li, K. Rachut, J. Morasch, J. Brötz, P. Reckers, T. Mayer, S. Rühle, A. Zaban, I. Mora Seró, J. Bisquert, W. Jaegermann, and A. Klein, "Energy band alignment between anatase and rutile TiO₂," *The Journal of Physical Chemistry Letters*, vol. 4, no. 23, pp. 4182–4187, 2013.
- [44] D. O. Scanlon, C. W. Dunnill, J. Buckeridge, S. A. Shevlin, A. J. Logsdail, S. M. Woodley, C. R. A. Catlow, M. J. Powell, R. G. Palgrave, I. P. Parkin, G. W. Watson, T. W. Keal, P. Sherwood, A. Walsh, and A. A. Sokol, "Band alignment of rutile and anatase TiO₂," *Nature Materials*, vol. 12, pp. 798–801, 2013.
- [45] M. Cargnello, T. R. Gordon, and C. B. Murray, "Solution-phase synthesis of titanium dioxide nanoparticles and nanocrystals," *Chemical Reviews*, vol. 114, no. 19, pp. 9319–9345, 2014.
- [46] K. Vinodgopal, S. Hotchandani, and P. V. Kamat, "Electrochemically assisted photocatalysis: titania particulate film electrodes for photocatalytic degradation of 4-chlorophenol," *The Journal of Physical Chemistry*, vol. 97, no. 35, pp. 9040–9044, 1993.
- [47] S. Ngamsinlapasathian, T. Sreethawong, Y. Suzuki, and S. Yoshikawa, "Single- and double-layered mesoporous TiO₂/P25 TiO₂ electrode for dye-sensitized solar cell," *Solar Energy Materials and Solar Cells*, vol. 86, no. 2, pp. 269–282, 2005.
- [48] T. Ohno, K. Sarukawa, K. Tokieda, and M. Matsumura, "Morphology of a TiO₂ photocatalyst (degussa, P-25) consisting of anatase and rutile crystalline phases," *Journal of Catalysis*, vol. 203, no. 1, pp. 82–86, 2001.
- [49] A. A. Ismail and D. W. Bahnemann, "Mesoporous titania photocatalysts: preparation, characterization and reaction mechanisms," *Journal of Materials Chemistry*, vol. 21, pp. 11686–11707, 2011.
- [50] A. Hagfeldt, G. Boschloo, L. Sun, L. Kloo, and H. Pettersson, "Dye-sensitized solar cells," *Chemical Reviews*, vol. 110, no. 11, pp. 6595–6663, 2010.
- [51] A. K. Chandiran, P. Comte, R. Humphry-Baker, F. Kessler, C. Yi, M. K. Nazeeruddin, and M. Grätzel, "Evaluating the critical thickness of TiO₂ layer on insulating mesoporous templates for efficient current collection in dye-sensitized solar cells," *Advanced Functional Materials*, vol. 23, no. 21, pp. 2775–2781, 2013.
- [52] J. Weickert, R. B. Dunbar, H. C. Hesse, W. Wiedemann, and L. Schmidt-Mende, "Nanostructured organic and hybrid solar cells," *Advanced Materials*, vol. 23, no. 16, pp. 1810–1828, 2011.
- [53] J. Qu and C. Lai, "One-dimensional TiO₂ nanostructures as photoanodes for dye-sensitized solar cells," *Journal of Nanomaterials*, vol. 2013, 2013.
- [54] H. Wang, Z. Guo, S. Wang, and W. Liu, "One-dimensional titania nanostructures: Synthesis and applications in dye-sensitized solar cells," *Thin Solid Films*, vol. 558, pp. 1–19, 2014.
- [55] K. Shankar, J. I. Basham, N. K. Allam, O. K. Varghese, G. K. Mor, X. Feng, M. Paulose, J. A. Seabold, K.-S. Choi, and C. A. Grimes, "Recent advances in the use of TiO₂ nanotube and nanowire arrays for oxidative photoelectrochemistry," *The Journal of Physical Chemistry C*, vol. 113, no. 16, pp. 6327–6359, 2009.
- [56] Y. L. Pang, S. Lim, H. C. Ong, and W. T. Chong, "A critical review on the recent progress of synthesizing techniques and fabrication of TiO₂-based nanotubes photocatalysts," *Applied Catalysis A: General*, vol. 481, pp. 127–142, 2014.
- [57] S. Liu and K. Huang, "Straightforward fabrication of highly ordered TiO₂ nanowire arrays in {AAM} on aluminum substrate," *Solar Energy Materials and Solar Cells*, vol. 85, no. 1, pp. 125–131, 2005.
- [58] K. P. Musselman, G. J. Mulholland, A. P. Robinson, L. Schmidt-Mende, and J. L. MacManus-Driscoll, "Low-temperature synthesis of large-area, free-standing nanorod arrays on ITO/glass and other conducting substrates," *Advanced Materials*, vol. 20, no. 23, pp. 4470–4475, 2008.
- [59] X. Ren, T. Gershon, D. C. Iza, D. Muñoz-Rojas, K. Musselman, and J. L. MacManus-Driscoll, "The selective fabrication of large-area highly ordered TiO₂ nanorod and nanotube arrays on conductive transparent substrates via sol-gel electrophoresis," *Nanotechnology*, vol. 20, no. 36, p. 365604, 2009.
- [60] J.-M. Wu, "Low-temperature preparation of titania nanorods through direct oxidation of titanium with hydrogen peroxide," *Journal of Crystal Growth*, vol. 269, no. 2-4, pp. 347–355, 2004.

- [61] X. Feng, K. Shankar, O. K. Varghese, M. Paulose, T. J. Latempa, and C. A. Grimes, "Vertically aligned single crystal TiO₂ nanowire arrays grown directly on transparent conducting oxide coated glass: Synthesis details and applications," *Nano Letters*, vol. 8, no. 11, pp. 3781–3786, 2008.
- [62] B. Liu and E. S. Aydil, "Growth of oriented single-crystalline rutile TiO₂ nanorods on transparent conducting substrates for dye-sensitized solar cells," *Journal of the American Chemical Society*, vol. 131, no. 11, pp. 3985–3990, 2009.
- [63] H. Shin, D.-K. Jeong, J. Lee, M. M. Sung, and J. Kim, "Formation of TiO₂ and ZrO₂ nanotubes using atomic layer deposition with ultraprecise control of the wall thickness," *Advanced Materials*, vol. 16, no. 14, pp. 1197–1200, 2004.
- [64] T. R. B. Foong, Y. Shen, X. Hu, and A. Sellinger, "Template-directed liquid ALD growth of TiO₂ nanotube arrays: Properties and potential in photovoltaic devices," *Advanced Functional Materials*, vol. 20, no. 9, pp. 1390–1396, 2010.
- [65] L. K. Tan, M. K. Kumar, W. W. An, and H. Gao, "Transparent, well-aligned TiO₂ nanotube arrays with controllable dimensions on glass substrates for photocatalytic applications," *ACS Applied Materials & Interfaces*, vol. 2, no. 2, pp. 498–503, 2010.
- [66] J. Weickert, C. Palumbiny, M. Nedelcu, T. Bein, and L. Schmidt-Mende, "Controlled growth of TiO₂ nanotubes on conducting glass," *Chemistry of Materials*, vol. 23, no. 2, pp. 155–162, 2011.
- [67] K. L. Chopra, P. D. Paulson, and V. Dutta, "Thin-film solar cells: an overview," *Progress in Photovoltaics: Research and Applications*, vol. 12, no. 2-3, pp. 69–92, 2004.
- [68] X. Fan, M. Zhang, X. Wang, F. Yang, and X. Meng, "Recent progress in organic-inorganic hybrid solar cells," *Journal of Materials Chemistry A*, vol. 1, pp. 8694–8709, 2013.
- [69] P. Docampo, S. Guldin, T. Leijtens, N. K. Noel, U. Steiner, and H. J. Snaith, "Lessons learned: From dye-sensitized solar cells to all-solid-state hybrid devices," *Advanced Materials*, vol. 26, no. 24, pp. 4013–4030, 2014.
- [70] L. Schmidt-Mende, S. M. Zakeeruddin, and M. Grätzel, "Efficiency improvement in solid-state-dye-sensitized photovoltaics with an amphiphilic ruthenium-dye," *Applied Physics Letters*, vol. 86, no. 1, 2005.
- [71] J. Weickert, E. Zimmermann, J. B. Reindl, T. Pfadler, J. A. Dorman, A. Petrozza, and L. Schmidt-Mende, "Synergistic effects of interfacial modifiers enhance current and voltage in hybrid solar cells," *APL Materials*, vol. 1, no. 4, 2013.
- [72] J. A. Dorman, J. Weickert, J. B. Reindl, M. Putnik, A. Wisnet, M. Noebels, C. Scheu, and L. Schmidt-Mende, "Control of recombination pathways in TiO₂ nanowire hybrid solar cells using Sn⁴⁺ dopants," *The Journal of Physical Chemistry C*, vol. 118, no. 30, pp. 16672–16679, 2014.
- [73] L. Yang, U. B. Cappel, E. L. Unger, M. Karlsson, K. M. Karlsson, E. Gabrielsson, L. Sun, G. Boschloo, A. Hagfeldt, and E. M. J. Johansson, "Comparing spiro-OMeTAD and P3HT hole conductors in efficient solid state dye-sensitized solar cells," *Physical Chemistry Chemical Physics*, vol. 14, pp. 779–789, 2012.
- [74] J. Burschka, A. Dualeh, F. Kessler, E. Baranoff, N.-L. Cevey-Ha, C. Yi, M. K. Nazeeruddin, and M. Grätzel, "Tris(2-(1H-pyrazol-1-yl)pyridine)cobalt(III) as p-type dopant for organic semiconductors and its application in highly efficient solid-state dye-sensitized solar cells," *Journal of the American Chemical Society*, vol. 133, no. 45, pp. 18042–18045, 2011.
- [75] H. J. Snaith, "How should you measure your excitonic solar cells?," *Energy & Environmental Science*, vol. 5, pp. 6513–6520, 2012.



Chapter 3

Characterization and Experimental Details

3.1 Transmission Electron Microscopy

The principles of the transmission electron microscope (TEM) were developed mainly by Ernst Ruska during the early 1930s.¹ After exploring – and dismissing – the potential of electrostatic electron lenses in his diploma thesis 1930 at the University of Berlin, he was able to construct the first polepiece lenses based on magnetic fields in 1933. This resulted in the possibility to build electron microscopes which make use of the far smaller wavelength of electrons in comparison to visible light.² Consequently, towards the end of the 1930s the resolution of transmission electron micrographs surpassed the maximum resolution of light microscopes, which at this time was constrained by the Abbe limit at few hundred nanometers.

Figure 3.1 shows a basic schematic of a TEM. Starting at the top, the electron source is either a thermionic emitter (tungsten hair pin filament or LaB₆ tip), or a field emission gun (FEG).^{3–5} There are two sorts of FEGs, namely cold FEGs where electrons are extracted only with use of a strong electric field, and Schottky emitters, where a tungsten tip is additionally heated to increase the number of extracted electrons. While thermionic emitters allow for a simpler buildup and vacuum system, FEGs

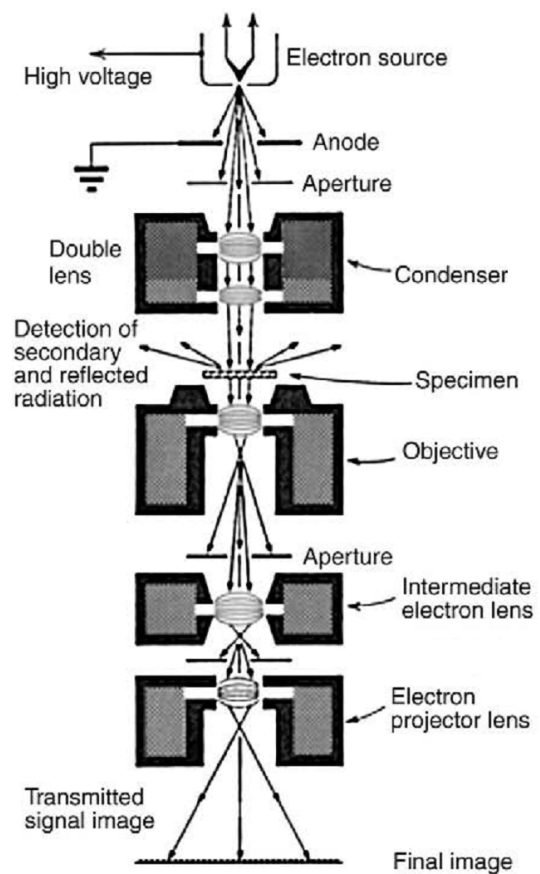


Figure 3.1: Simplified drawing of the electron path within a TEM and the basic setup of apertures and electron lenses.²

enable a narrower width of energies of the extracted electrons. Schottky emitters trade in some of the superior energy resolution for a higher intensity. The FEI Titan 80-300 S/TEM electron microscope preferentially used in this work is equipped with a Schottky emitter. Shortly below the emitter the electrons are accelerated by an electrical field to energies of several hundred keV. The section up to here is referred to as electron gun.

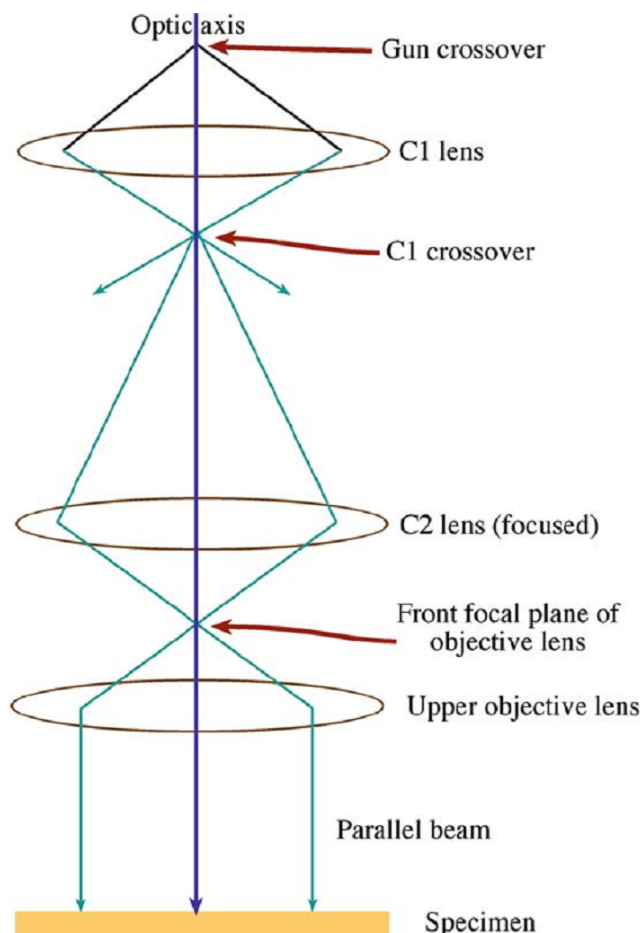


Figure 3.2: Electron beam condenser system before specimen. The lenses C1 and C2 condense the beam in a narrower spot along the optical axis, the upper objective lens is used to switch between parallel and convergent illumination of the sample.⁵ (left)

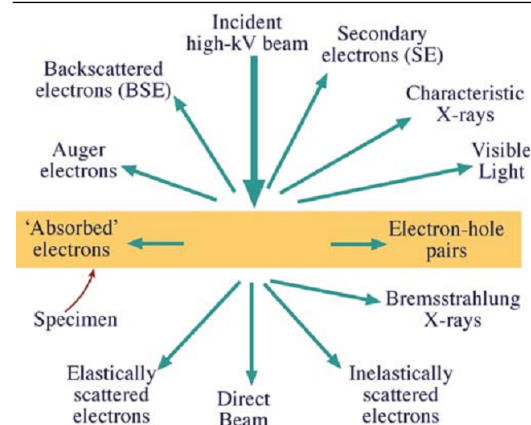


Figure 3.3: Interactions of the incident electron beam with the specimen. Information is extracted directly or indirectly from elastically scattered electrons (CTEM, HRTEM, ED, STEM), inelastically scattered electrons (EELS), and characteristic X-rays (EDX). Less frequent is the use of backscattered-electron (BSE) detectors and secondary-electron (SE) detectors in the TEM.⁵

Below the electron gun, the electrons are focused by a condenser system built up from electron lenses and apertures. This is depicted in Figure 3.2. Different excitations of the upper objective lens (also referred to as C3 lens) enable convergent and parallel electron beam illumination. Parallel beams provide a homogeneous illumination needed for most imaging modes and selected area electron diffraction (SAED). A convergent beam is used if the electron dose has to be confined to a small defined area, as for example in convergent beam electron diffraction (CBED), scanning transmission electron microscopy (STEM) and specifically in chemical analysis like energy-dispersive X-ray spectroscopy (EDX) and electron energy loss spectroscopy (EELS). When the electrons hit the sample, elastic and inelastic scattering events take place. Figure 3.3 gives an overview of signals which can be collected. They will be discussed in more detail below.

Apart from STEM mode, there are two basic operational modes the TEM can work in. Figure 3.4a shows the optical path in diffraction mode. Here, the intermediate lens is operated with a strength so that the diffracted electrons' pattern obtained in the back focal



plane of the objective lens is magnified and formed in the image plane (see Section 3.1), which then is further magnified and displayed on the screen. An optional selected area aperture limits the area of the sample which contributes to the diffraction pattern, so local differences can be explored. The conventional TEM imaging mode is depicted in Figure 3.4b. Here, the first image is further magnified and projected on the screen. An objective aperture can be used to select the direct or diffracted electrons to influence the information given in the image (see Sections 3.1 and 3.1).

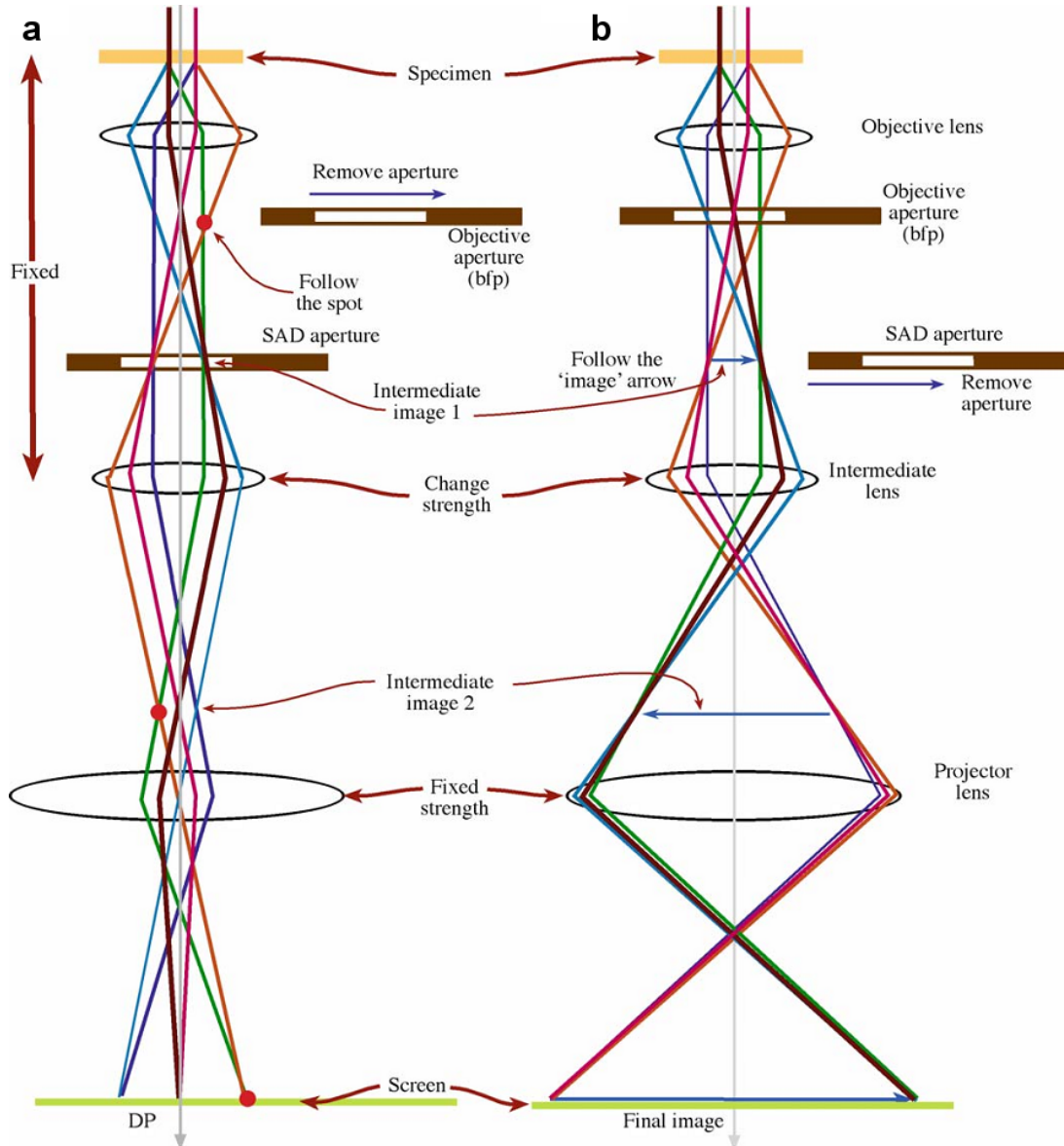


Figure 3.4: Ray diagram of the electrons for the different operation modes. The intermediate lens is used to switch between electron diffraction (a) and imaging mode (b). The SAD aperture can be inserted to select a specific area of the illuminated sample used for obtaining the diffraction pattern. The objective aperture is used to block out certain reflexes in the diffraction pattern to obtain bright-field or dark-field images.⁵

The diversity of imaging modes gives rise to a variety of possibilities to investigate and analyze materials on a local scale ranging down to sub-Ångström. These methods will be discussed in the following section.

High-Resolution Transmission Electron Microscopy

HRTEM When a parallel illumination of the sample is used, with an excitation of the lenses as shown in Figure 3.4b and without an objective aperture, the mode is referred to as high-resolution transmission electron microscopy.⁵ Since all of the diffracted electrons are used for the image formation, an HRTEM image contains all high spatial frequency information collected by the electron beam while transmitting the sample. For thin samples dominates the phase contrast (compared to the amplitude contrast) which arises from the interference between the different diffracted beams. Thus, especially the periodicity of the specimen can be depicted. However, HRTEM image contrast is always a convolution of the exit wave function of the electron, $\Psi(x, t)$,

$$\Psi(x, t) = \Psi_0 \cdot e^{i(k_e x - \omega_e t + \Phi)}, \quad (3.1)$$

where Ψ_0 is the amplitude, ω_e the angular frequency, t the time, k_e the wave vector, x the position and Φ the phase difference, with the contrast transfer function $CTF(u)$ of the microscope

$$CTF(u) = \sin \chi(u) \quad (3.2)$$

$$\text{with } \chi(u) = \frac{2\pi}{\lambda} \cdot \left(\frac{1}{4} C_s \lambda^4 u^4 + \frac{1}{2} \delta f \lambda^2 u^2 \right),$$

where u is the spatial frequency, C_s is the spherical aberration coefficient, λ the electron wavelength and δf the defocus value. Note that these equations are kept in one dimension for simplicity and that the weak phase object approximation is applied for the aforementioned exit wave function (Ψ_0 is unchanged). An important consequence of the image formation is that the absolute atom positions cannot simply be derived from an HRTEM image. For that, HRTEM simulations have to be performed, for example via the software package JEMS.⁶ In any case, the micrographs can readily be used to extract informations about the lattice plane d-spacing of depicted crystals, as well as corresponding angles between different planes. This is usually performed by a fast Fourier transformation (FFT) of selected areas of the image.

Low-Magnification High-Resolution Transmission Electron Microscopy

LM If the HRTEM conditions are used to image a sample at resolutions below the range of lattice planes, it can be referred to as low-magnification high-resolution transmission electron microscopy. To omit the objective lens can be advantageous in cases where the high contrast condition of the bright-field mode (see Section 3.1) leads to a decreased ability to recognize details when a major part of the electron beam is scattered at thick objects of interest in zone axis.



Electron Diffraction

ED Electron diffraction is a method making use of Bragg diffraction so that the crystallinity of the sample can be depicted and crystal parameters calculated.⁴ A setup of the TEM in parallel illumination as well as a lens excitation as shown in Figure 3.4a generates a diffraction pattern similar to X-ray diffraction patterns. A selected area diffraction aperture may be inserted to collect information from a certain location of the sample ranging down to a circular area of around 150 nm in diameter.

The Bragg equation

$$2d \sin \Theta = n\lambda \quad (3.3)$$

with lattice spacing d , Bragg angle Θ between lattice planes and incident electron beam, n as diffraction order and the λ in this case electron – wavelength λ , has to be fulfilled to obtain constructive interference. Figure 3.5 shows the simple case where an incident beam I is diffracted at an angle of 2Θ to give a diffracted beam D at the first order of diffraction ($n = 1$). As the electron wavelength is smaller than that of X-rays, the resulting angles Θ are reduced to a few degrees at the most. The crystalline nature of the sample is represented in the electron diffraction pattern. A diffuse circular halo occurs for amorphous materials, where the mean distance between neighboring atoms can be deduced. Defined rings are observed for polycrystalline materials, where the lattice plane distances can be calculated, and a periodic pattern of reflections is formed for single crystalline materials in zone axis, which enable the determination of lattice plane distances and angles between the planes, so that phase and orientation of the crystal are assignable. The presence of different materials within the selected area ensures a challenging effort of interpretation of a diffraction pattern.

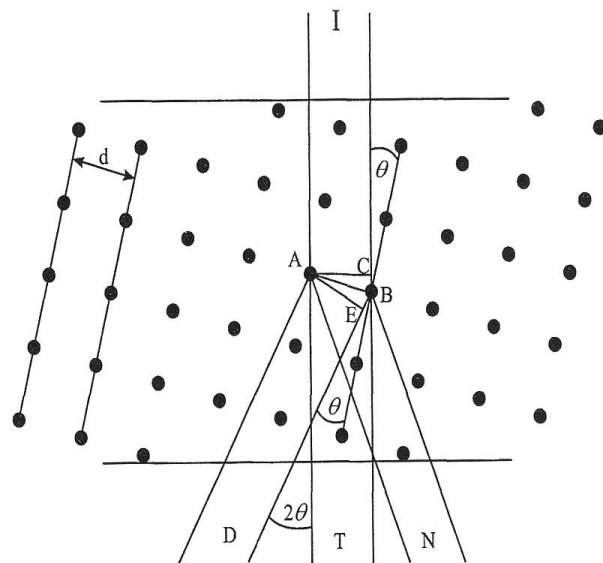


Figure 3.5: A crystalline specimen is hit by an incident electron beam (I). Non-diffracted electrons pass straight through the sample (T), while others are scattered in different directions. If the Bragg equation 3.3 is met (D), constructive interference is giving spots in the diffraction pattern. Other directions are non-constructive (N).⁴

Bright-Field Imaging

BF When the objective aperture is inserted in the backfocal plane of the objective lens in imaging mode (Figure 3.4b), bright field images can be obtained.⁵ In this mode, the aperture has to be centered around the direct beam to block most of the electrons which were diffracted. As most of the remaining electrons did not interact with the sample, phase contrast is strongly reduced and the amplitude contrast predominates. In

particular, all high-frequency information is omitted, so that crystalline details cease to be distinguishable. Instead, larger objects with different mass, thickness or orientation drastically gain in contrast so that morphology becomes more apparent. Since crystals which are oriented near zone axis lead to a stronger diffraction, the concerned areas appear considerably darker. Likewise, materials with higher density and/or thickness increase the fraction of scattered electrons, so that the corresponding areas decrease in brightness.

Dark-Field Imaging

DF When the objective aperture is centered around one of the reflections in the diffraction pattern, an off-axis dark field image is created.⁵ Consequently, only the electrons which are diffracted with a specific angle and direction contribute to the image, and areas of the sample can be highlighted which comprise of the respective crystal. This leads to an easy way for detecting crystal grains and determining their size and orientation. Since the image-giving electron beam leaves the sample by an angle with regard to the optical axis, aberrations can be amplified. These problems of the so-called off-axis dark field imaging can be prevented by tilting the electron beam prior to its impact on the sample, which accordingly has to be set up for each selected reflection separately.

Scanning Transmission Electron Microscopy

STEM Scanning transmission electron microscopy can be done either by a dedicated STEM, or by setting the appropriate illumination conditions in the condenser system in a TEM (see above), provided that a corresponding scanning- and detector system is present. In any case, the electron beam is focused with a high convergence angle, in such a way that the illuminated area of the specimen is as small as possible.^{3,5} This means that highest elaborateness has to be followed at calibrating the instrument. Simultaneously, the intensity has to be balanced between needed signal output, focus and possible beam damage of the sample. Deflector coils are employed to scan the beam across the specimen while a circular detector counts electrons which have been scattered during transmission. Depending on the position of the detector or the chosen camera length, a certain angular range of scattered electrons is detected. For angles below 10 mrad, a STEM BF image is acquired which information content largely equals a conventional BF image. The electrons collected in a range of 10 to 50 mrad constitute an annular dark field (ADF) image, which is characterized by elastically, coherently (Bragg) scattered electrons. This equals a combination of all possible conventional DF images. Electrons scattered at angles higher than 50 mrad, predominantly by incoherent Rutherford scattering, create a high-angle annular dark field (HAADF) image. A strong dependency of intensity to the roughly squared atomic number gives them the name of Z-contrast images. However, sample thickness and density also play a role in contrast. HAADF is mainly used for the detection of heavy elements within a sample. This can be especially rewarding when atomic resolution is desired. A small beam size can be achieved, so that sub-Ångström resolution is possible,



which means that the beam diameter is smaller than the distance between the atomic columns. Thus, the atomic configuration of crystals can be identified. Figure 3.6 gives two schematics of possible detection alignments. The first one, mainly found at dedicated STEMs, possesses several fixed detectors which cover defined angular ranges. The second one is installed at TEM/STEM instruments and works by using different camera lengths L for a single annular detector, which leads to an appropriate selection of the angular range and is changed by a lens system.

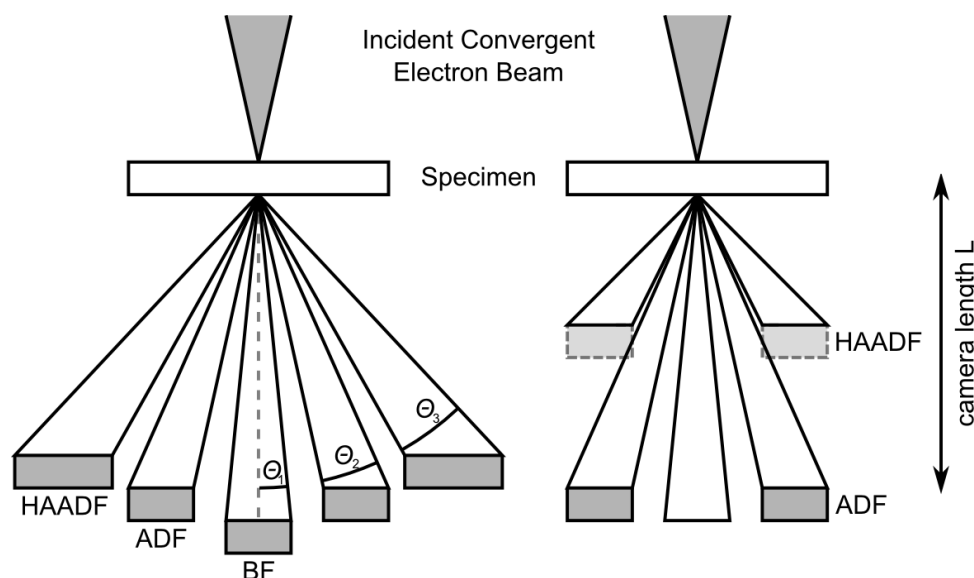


Figure 3.6: Schematic of STEM detection ranges. The BF detector collects electrons from the direct beam and those which are scattered at very low angle ($\Theta_1 < 10$ mrad). ADF and HAADF detectors collect electrons with larger scattering angles ($10 \text{ mrad} < \Theta_2 < 50$ mrad and $\Theta_3 > 50$ mrad). ADF and HAADF modes can also be achieved using only one ring-shaped detector which is illuminated at different camera lengths L to change the collector angle, as seen on the right schematic.³

STEM mode is also highly beneficial for the analytical methods energy-dispersive X-ray spectroscopy and electron energy loss spectroscopy, as the area of interests can be selected with a high spatial resolution. HAADF is also the most commonly used method to obtain data for electron tomography, which will be elucidated in detail in Section 3.2.

Secondary-Electron Transmission Electron Microscopy

SETEM A less conventional use of STEM is the detection of secondary electrons which are released by the primary electron beam.⁵ Shell electrons, and those from valence or conduction band, which are excited above the vacuum level are able to exit the sample as long as they are generated a few ten nanometers below the surface. This gives rise to a signal which can provide a three-dimensional impression in images much like an SEM micrograph.

Energy-Dispersive X-Ray Spectroscopy

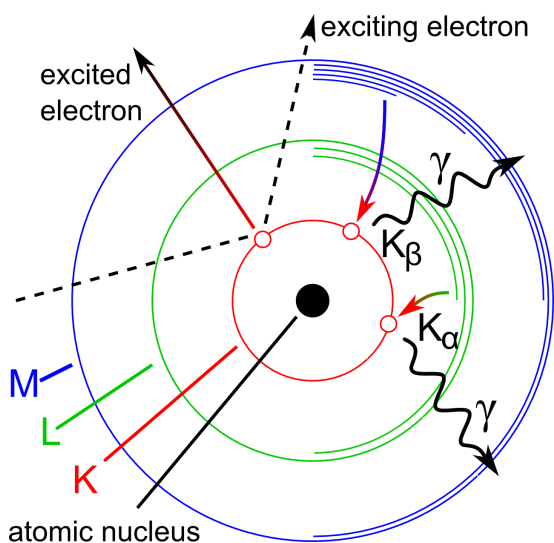


Figure 3.7: Schematic of the origin of characteristic X-rays.

EDX As indicated in Figure 3.3, characteristic X-ray emission of a sample can be detected to obtain information concerning its elemental composition.^{5,7} Due to the high involved energies, the incident electron beam excites inner shell electrons of the atoms to higher unoccupied states, or ionizes them (see Figure 3.7). When the vacant state is filled by an electron from an outer shell, possibly leading to a cascade, the energy difference can be released by the emission of a photon. This γ -quantum is usually within the X-ray band, at an energy of one to several keV, and strongly dependent on the element. The emission is isotropic in all directions, so a – usually silicon-based – detector

is introduced into the microscope column as near as possible above the specimen to detect a large amount of the X-rays. Counting the X-rays with a certain energy dispersion allows an inference on the elemental composition of the sample. Certain care has to be taken of the superimposed background of Bremsstrahlung (which arises from deceleration of electrons within the Coulomb-field of the atoms), as well as a possible overlap of the element-specific lines. A careful background subtraction and Gaussian curve fitting of the peaks allows quantification of the elements within certain limits. An application of EDX in STEM mode enables the collection of EDX spectra with high spatial precision and even the generation of larger maps to understand the elemental distribution within selected areas of the specimen. As EDX detectors usually absorb low-energy X-rays below 1 keV, the detection of elements lighter than boron is not feasible. This problem is intensified as the low energy photons have a low fluorescence yield and can be easily absorbed in the sample.

Electron Energy Loss Spectroscopy

EELS While detection of light elements is problematic with an EDX detector, EELS is a possibility to close this gap.⁷⁻⁹ When the beam electrons transmit the sample, several inelastic scattering mechanisms can take place as denoted in Figure 3.3. Mainly two of them contribute to the EEL spectrum, namely the excitation of plasmons and the excitation of shell electrons. Beam electrons can lose a small part of their energy in such an incident. A setup as shown simplified in Figure 3.8 can disperse the electrons by a magnetic prism according to their energy and collect a spectrum with a detector array (usually a charged-coupled device, CCD). As the detection range is roughly limited to an energy loss below 2 keV due to its low signal above this value, this method is much more expedient to the de-



tection of light elements. In general, an EEL spectrum is separated into low-loss and core-loss regions. Low-loss comprises the zero-loss peak, the electrons which did not lose any energies, and the plasmon peak. A good microscope utilizing a monochromator can extract the values of semiconductor band gaps from their offset. In addition, single valence electron transitions occur in this regime with energies of inter and intra band transitions. The plasmon intensity can be used to calculate sample thicknesses. The core-loss regions feature element-specific edges. While the onset of the edge is the main identifier for the according element, its fine structure (energy-loss near edge structure, ELNES, and extended energy-loss fine structure, EXELFS) contains information about crystal phases and bonding states. To enable a high quality spectrum, and thus deeper understanding, the energy dispersion is to be kept below 0.3 eV.

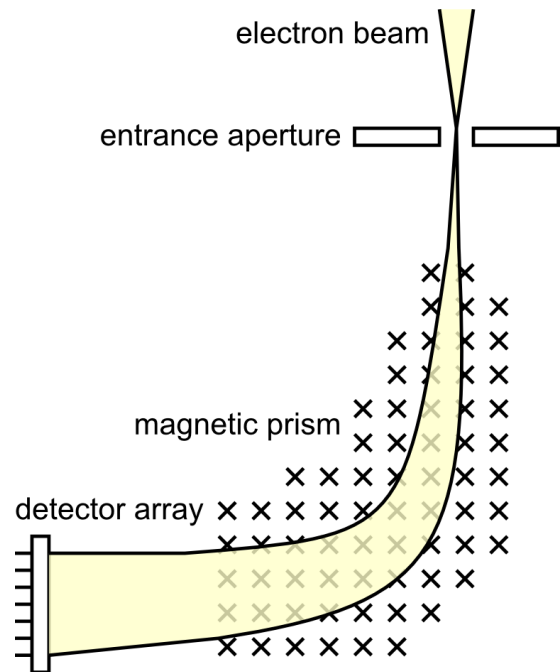


Figure 3.8: Schematic of an EELS detector system. The entrance aperture is located after the viewing screen. After that, the electrons are dispersed by a magnetic prism according to their energy. The detector array is usually a CCD.

Energy-Filtered Transmission Electron Microscopy

EFTEM By inserting an aperture into the dispersed electron beam between magnetic prism and CCD, all electrons except those with a defined energy can be blocked out. Using the three window method, where a set of two images with energy windows before the edge (calculation of background) and one image with an energy window at the edge (relevant signal) are taken, elements can be mapped.¹⁰

3.2 Electron Tomography

Despite that the establishment of algorithms concerning projectional tomography goes way back to the middle of the 20th century, only for the last 20 years a broad availability of potent computing capacity paved the way for a sophisticated use of electron tomography. Due to an unsurpassed potential resolution, electron tomography is one of the most promising techniques to gain a deep understanding of morphologies at the nanoscopic range.¹¹ Even the distribution of chemical compositions within a given sample can be investigated by elaborate techniques like EFTEM tomography.¹² Adding the capability of localizing dislocations,¹³ reconstructing a tomogram with atomic resolution^{14,15} and even the possibility of time-resolved measurement,¹⁶ it is obvious that electron tomography is

a much valued source of information concerning not only morphologies, but also – taking into account the appropriate scientific interpretation – chemical and electronic behavior of nano materials.

Acquisition

Contrary to other imaging techniques like magnetic resonance tomography or atom probes, the data acquisition in the TEM can not be carried out slice-wise, but has to be achieved by tilting the sample along an axis perpendicular to the optical path of the electrons. Figure 3.9 gives a schematic of the acquisition of a series of projections. To obtain quantitative data and maximize contrast, STEM mode is mostly chosen over CTEM in material science. Usually, an HAADF detector is employed for the acquisition of a projection series, but the usage of the STEM BF detector is possible as well. STEM micrographs are taken at different tilt angles. Depending on the

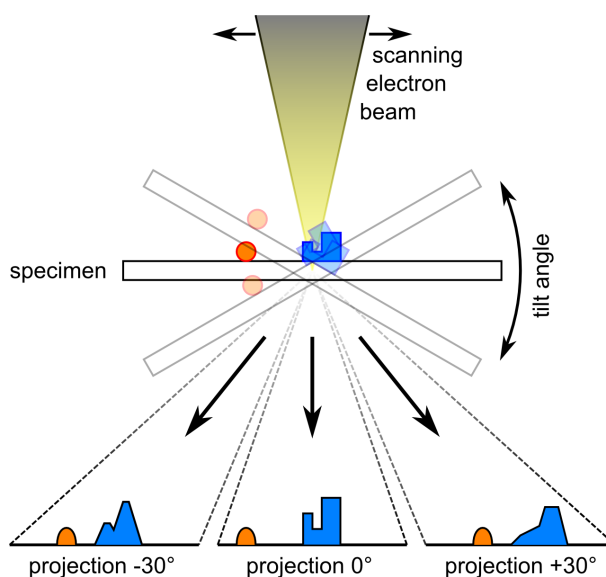


Figure 3.9: Schematic of the acquisition setup for electron tomography.

stability of the specimen, the number of projections is kept as high as possible, meaning that the tilt increment per projection has to be small. As the tomography sample holder is physically restricted to certain limits (between ± 70 to 80°), some tilt angles can not be set. This is called the *missing wedge* and leads to anisotropic resolution.¹⁷ Techniques are developed to overcome this problem, namely double-tilt sample holders which reduce it to a *missing pyramid*,¹⁸ and 360° setups¹⁹ where a sample is specifically prepared in a focused ion beam to obtain a copped tip at the area of interest. Sometimes the Saxton scheme is applied, where the tilt increments at the outer limits are reduced in accordance to improve the amount of available data near the missing wedge.²⁰ This is especially expedient for roughly two dimensional samples. The angle increments ϕ are calculated by $\phi = (r/t) \cdot \cos(\Phi)$, starting at $\Phi = 0^\circ$ with r/t as loose factor of desired resolution r and sample thickness t . Examples for possible Saxton schemes is given in the box at the right. The acquisition itself can be carried out manually or automatically, provided a drift correction is possible. However, as the particle of interest mostly lies apart from the center of the

Saxton scheme for $t/r = 3$:

$0^\circ, \pm 19.1^\circ, \pm 37.1^\circ, \pm 52.4^\circ, \pm 64.0^\circ, \pm 78.2^\circ$

Simplified Saxton scheme:

Start at an acquisition angle of -70° with tilt increments of 1° up to -50° . Then increments of 2° up to $+50^\circ$. From $+50^\circ$ to $+70^\circ$ again increments of 1° . This gives projection angles as follows:

$-70^\circ, -69^\circ, -68^\circ, \dots, -52^\circ, -51^\circ, -50^\circ, -48^\circ, -46^\circ, -44^\circ, \dots, +44^\circ, +46^\circ, +48^\circ, +50^\circ, +51^\circ, +52^\circ, \dots, +68^\circ, +69^\circ, +70^\circ$



tilting axis, focus has to be adjusted after each step. The advantage of manual alignment are reliable focus adjustment and drift correction (automatic drift correction needs distinct sample areas for orientation), whereas the automatic series acquisition benefits from a sped-up process and thus less sample illumination and beam damage.²¹ To extenuate the latter, manual focusing is done adjacent to the area of interest.

Algorithms

The variety of reconstruction algorithms for electron tomography is constantly growing. Figure 3.10 shows a schematic of the arithmetical origin of the projections. The illuminating rays collect information about the sample along the arrows which are then combined to projections. The simplest possibility to extract a reconstruction from these projections is backprojection (BP) based on the Radon transform.²² Here, the data of each point of a projection is evenly distributed over the reconstruction volume, in principle retracing the illuminating ray. Variations of this method are the filtered backprojection (FBP),²³ where filters are applied to the projections before reconstruction, and the weighted backprojection (WBP),^{24,25} where a weighting function is convoluted with the projection or its Fourier transform. More powerful – but also more time consuming – reconstruction algorithms rely on an iterative comparison of the original projections with calculated reprojections from the derived reconstructions. The original algebraic reconstruction technique²⁶ (ART) is based on the Kaczmarz method²⁷ and treats the projections and their reconstruction as a linear system of equations which are solved numerically. Its core equations are as follows:

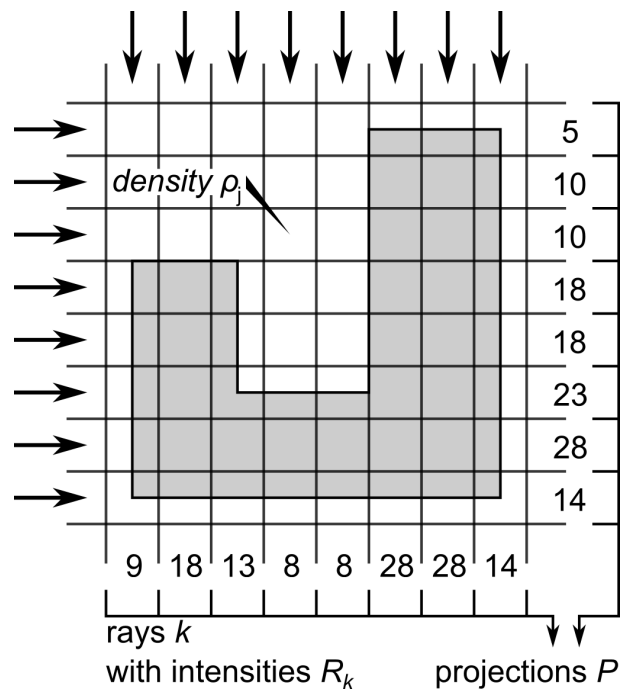


Figure 3.10: Schematic of the acquired projections.

with R_{kP}^q as the intensity (integrated optical density) of ray k of projection P at iteration q (R_{kP} would be the numbers in Figure 3.10), N_{kP} the grid points included in ray (k, P) and ρ_j^q the q th iterate of the density (point/pixel/voxel) ρ_j . Two methods are feasible. The direct multiplicative method determines the next iteration of ρ_j^q as

$$\rho_j^{q+1} = \left(\frac{R_{kP}}{R_{kP}^q} \right) \rho_j^q, \quad (3.5)$$

the direct additive method as

$$\rho_j^{q+1} = \max[\rho_j^q + (R_{kP} - R_{kP}^q)/N_{kP}, 0]. \quad (3.6)$$

Both methods adopt the change of a ρ_j^q in each subsequent step, so that the algorithm enables fast converging reconstructions. However, this fact also renders ART susceptible to the inclusion of reconstruction artifacts. Nowadays more commonly used is the simultaneous iterative reconstruction technique (SIRT).^{28,29} It is based on ART but includes two important changes: First, the reconstruction is only updated after all projections ρ_j^q of the volume have been accounted for. Second, the data points ρ_j and the rays k are allocated a certain area. This means that the influence of the rays are weighted based on the overlap of these two areas, as shown by the red (weight w_{jkP} within the ray) and yellow (outside of the ray) parts of the voxel marked in Figure 3.11. The unconstrained additive SIRT algorithm including weighting is as follows:³⁰

$$\rho_j^{q+1} = \rho_j^q + \frac{1}{\sum_{k,P} w_{jkP}} \sum_{k,P} \frac{w_{jkP}}{\sum_{N_{kP}} w_{N_{kP}}} (R_{kP} - R_{kP}^q). \quad (3.7)$$

$\frac{1}{\sum_{k,P} w_{jkP}}$ normalizes the pixel correction over all contributing rays of all projections, while the term $\frac{w_{jkP}}{\sum_{N_{kP}} w_{N_{kP}}}$ is responsible to allocate the ratio of the correcting residual $R_{kP} - R_{kP}^q$ from one ray to all voxels N_{kP} it penetrates.

To give a meaningful model of the object of interest, all reconstructions obtained from the algorithms so far (BP, FBP, WBP, ART and SIRT) have to be segmented. This can be done based on the histogram of the reconstruction or manually by determining the best possible shape representing the initial projections. However, a more elegant way is to calculate the reconstruction by the discrete algebraic reconstruction technique (DART).^{31,32} This is based on SIRT and utilizes a starting model derived from a SIRT reconstruction. DART implements two important criteria: First, it is assumed that the object of interest is build from a finite number (mostly < 5) of densities, which means a number of distinct gray values. These have to be derived from the preceding SIRT algorithms and can be enhanced in their quality by additional techniques like masked SIRT etc.³² Each voxel of the DART reconstruction is only allowed to take one of the preassigned gray values. Second, the actual reconstruction is restricted to voxels which are not surrounded only by neighbors with the same gray value. This means a severe reduction of computing power, as the voxels in the bulk of an object as well as within the vacuum are not considered at every iteration.

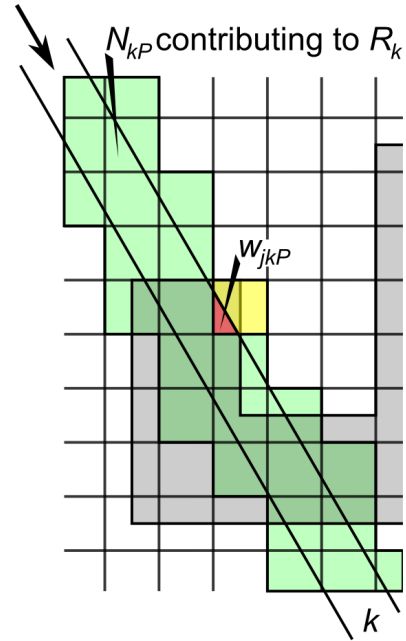


Figure 3.11: Weighting for SIRT. The red part of the voxel is the weight of it with regard to ray k . The green voxels N_{kP} contribute to ray R_k .



Procedure

The general procedure to obtain a tomogram from an object of interest is as follows. First, a region has to be found on the sample which contains an adequate object as well as few other interfering material, which would complicate reconstruction due to background disturbances. **Time studies** have to be performed concerning contamination and beam damage of the object to determine suitable parameters to avoid or at least minimize these issues. Provided that satisfying results are found, the **projection series** can be recorded. Depending on the sample this can be performed automatically or manually, and with a number of projections ranging from about 10 to 100. After each increment of the tilt series, stable conditions have to be achieved and the image has to be focused anew. Provided that the resulting projection series is sufficient, it has to be aligned and the background is subtracted. These two actions are vital. **Background subtraction** is normally achieved by projection-wise subtracting the average of an homogeneous part of the image which does depict "nothing" (carbon film or vacuum). For the **alignment**, several techniques are possible. Amongst the most popular ones are cross-correlation of the images,³³ tracking of fiducial markers,³⁴ tracking of the center of mass (*barycenter*),³² contrast-³⁵ and landmark-based alignments.³⁶ The method of alignment is carefully chosen depending on the nature of the sample. Generally it is more simple to align a single particle than a larger distribution of low-density inhomogeneous organic material. After the alignment is optimized, the actual **reconstruction** takes place. Depending on series and algorithm, this can be done in one step (BP, FBP, WBP, ART, SIRT) or several (SIRT+DART, including the generation of a mask). Finally, the reconstruction is refined by fine-tuning some of the reconstruction parameters like alignment or segmentation and re-running of the reconstruction algorithm. A detailed step-by-step instruction for the reconstruction of a projection series can be found in Section 9.2.

3.3 TEM Sample Preparation

Carbon-Coated Metal Grids

The easiest way to prepare TEM samples is the use of metal grids. These grids can be coated by continuous, holey or lacy carbon films. For the grids themselves, a wide range of materials like Cu, Ni, Mo, Au etc., and morphologies differing in mesh sizes or implemented labels are available. Figure 3.12a shows one of the grids which have a diameter of 3.05 mm and are few hundredths of a millimeter thick. Figure 3.12b is a more detailed image of one of the segments covered by an holey carbon film. Handling has to be cautious, as small bends or damages can induce drift during the measurements and impede high-quality results.

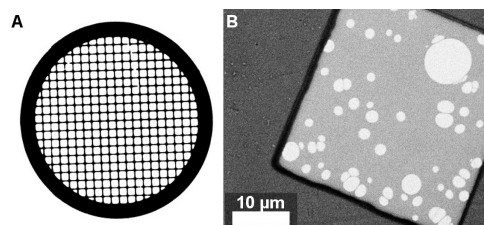


Figure 3.12: a) Schematic of a metal grid. b) A single sector coated by a holey carbon film.³⁷

Two major techniques can be used to prepare material on these grids. The simpler one is to scrape material loose from the sample and carefully dab the grid on it. This is the fastest way to procure a TEM sample, as no time has to be spent for drying the sample. This is compulsory at the second technique, where material is removed from the specimen chemically or mechanically and dissolved in a solvent like ethanol. Ultrasonification ensures a homogeneous distribution of material within the solution. Next, few droplets of the solution are dripped onto the grid. The drying period can last from 30 minutes to several hours, before the sample can safely be used in the TEM.

Cross-Sectional TEM Sample Preparation

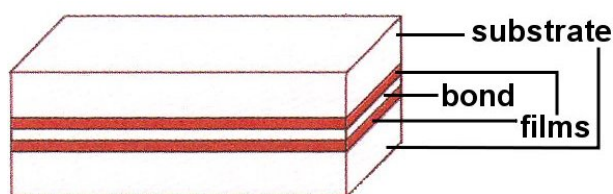


Figure 3.13: Cross-section sandwich structure.³

Apart from the possibility to grind down bulk materials like metals or metal-oxides, conventional cross-section samples are specifically useful to determine properties of layered systems, especially with regard to interfaces. Thin films, whether compact, porous, nanowired, nanotubular or more complex, can be examined in the

TEM by preparing cross sections based on the instructions from Strecker et al.:³⁸ The substrate is cut together with the films into bars like depicted in Figure 3.13 by a diamond saw (Wells). The structure is substrate/films/bond/films/substrate with a bond like Vishay M-bond 610 or Gatan G1 epoxy. The resulting bar is then glued into a $\varnothing 3$ mm brass tube with Gatan G1 Epoxy. Then, a slice with a thickness of around 0.3 mm is cut out, ground and polished to 60-100 μm . The resulting disk is sketched in Figure 3.14.

Dimples are introduced to both sides by mechanical dimpling (Gatan Dimple Grinder), so that the resulting thickness at the center of the disk is below 25 μm . Additional polishing ensures a defect free surface. This is important, as the next step – ion milling – inherits the asperity throughout the process. The ion milling is performed by a Gatan PIPS and, depending

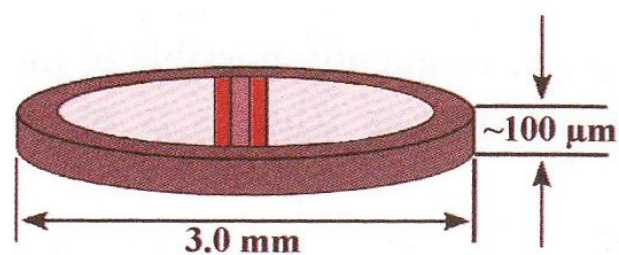
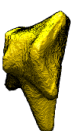


Figure 3.14: Cross-section slice.³

on the requirements of the sample, often under liquid nitrogen cooling. This process is observed visually by camera or microscope to determine the time to stop. Decisive is in this case the electron transparency of the area of interest. A wedge-shaped fringe has to be as thin as possible, at a low wedge angle of about 8° . This can be influenced by the impact angle of the argon ions. Electron transparency is achieved when the region is thinner than about 100 nm, depending on the material composition within the sample.



Focused Ion Beam Sample Preparation

FIB sample preparation is a highly sophisticated method to obtain cross sections from site-specific regions and from samples which are not suitable for conventional cross-section sample preparation. It is preeminent when specified nanometer-sized objects have to be selected and prepared for TEM. Also when certain sample areas or specific orientations are sought, the precision of site-specific sample preparation is unequalled. In this preparation method, the sample is usually inserted into a combined SEM/FIB instrument. SEM is used to search a suitable sample area and to survey the milling process. The focused Ga ion beam itself is used to cut away the material around the region of interest. Then the remaining lamella is mechanically extracted and glued on a special FIB sample grid. Then it is thinned down by the ion beam to reach electron transparency. This is an elegant way to obtain TEM samples of bulk material, stacked films and nanostructures.

Bibliography

- [1] E. Ruska, "The development of the electron microscope and of electron microscopy," *Reviews of Modern Physics*, vol. 59, no. 3, p. 627, 1987.
- [2] L. E. Murr, "Imaging systems and materials characterization," *Materials Characterization*, vol. 60, pp. 397–414, 2009.
- [3] D. Brandon and W. D. Kaplan, *Microstructural Characterization of Materials*. John Wiley & Sons, Ltd., 2nd ed., 2008.
- [4] P. J. Goodhew, J. Humphreys, and R. Beanland, *Electron Microscopy and Analysis*. Taylor & Francis, 3rd ed., 2001.
- [5] D. B. Williams and C. B. Carter, *Transmission Electron Microscopy*. Springer Science, New York, 2009.
- [6] Pierre Stadelmann, "JEMS - Electron Microscopy Software, Java Version." <http://cimewww.epfl.ch/people/stadelmann/jemsWebSite/jems.html>, 2014. [Online; accessed 14-October-2014].
- [7] R. Schneider, "High-resolution analytical TEM of nanostructured materials," *Analytical and Bioanalytical Chemistry*, vol. 374, no. 4, pp. 639–645, 2002.
- [8] R. Brydson, *Electron Energy Loss Spectroscopy*. BIOS Scientific Publishers Limited, 2001.
- [9] S. Casciardi, R. Sisto, and M. Diociaiuti, "The analytical transmission electron microscopy: A powerful tool for the investigation of low-dimensional carbon nanomaterials," *Journal of Nanomaterials*, vol. 2013, p. 506815, 2013.
- [10] L. Reimer, I. Fromm, P. Hirsch, U. Plate, and R. Rennekamp, "Combination of EELS modes and electron spectroscopic imaging and diffraction in an energy-filtering electron microscope," *Ultramicroscopy*, vol. 46, no. 1-4, pp. 335–347, 1992.
- [11] P. A. Midgley and R. E. Dunin-Borkowski, "Electron tomography and holography in materials science," *Nature Materials*, vol. 8, pp. 271–280, 2009.
- [12] P. A. Midgley, E. P. W. Ward, A. B. Hungria, and J. M. Thomas, "Nanotomography in the chemical, biological and materials sciences," *Chemical Society Reviews*, vol. 36, pp. 1477–1494, 2007.
- [13] C.-C. Chen, C. Zhu, E. R. White, C.-Y. Chiu, M. Scott, B. Regan, L. D. Marks, Y. Huang, and J. Miao, "Three-dimensional imaging of dislocations in a nanoparticle at atomic resolution," *Nature*, vol. 496, pp. 74–77, 2013.
- [14] S. V. Aert, K. J. Batenburg, M. D. Rossell, R. Erni, and G. Van Tendeloo, "Three-dimensional atomic imaging of crystalline nanoparticles," *Nature*, vol. 470, pp. 374–377, 2011.
- [15] Z. Saghi and P. A. Midgley, "Electron tomography in the (S)TEM: From nanoscale morphological analysis to 3D atomic imaging," *Annual Review of Materials Research*, vol. 42, pp. 59–79, 2012.

- [16] O.-H. Kwon and A. H. Zewail, “4D electron tomography,” *Science*, vol. 328, no. 5986, pp. 1668–1673, 2010.
- [17] P. A. Midgley, M. Weyland, T. Yates, I. Arslan, R. Dunin-Borkowski, and J. Thomas, “Nanoscale scanning transmission electron tomography,” *Journal of Microscopy*, vol. 223, pp. 185–190, 2006.
- [18] P. Penczek, M. Marko, K. Buttle, and J. Frank, “Double-tilt electron tomography,” *Ultramicroscopy*, vol. 60, no. 3, pp. 393 – 410, 1995.
- [19] M. Duchamp, A. Ramar, A. Koács, T. Kasama, F. J. Haug, S. B. Newcomb, C. Ballif, and R. E. Dunin-Borkowski, “Conventional and 360 degree electron tomography of a micro-crystalline silicon solar cell,” *Journal of Physics: Conference Series*, vol. 326, no. 1, p. 012057, 2011.
- [20] W. O. Saxton, W. Baumeister, and M. Hahn, “Three-dimensional reconstruction of imperfect two-dimensional crystals,” *Ultramicroscopy*, vol. 13, no. 1-2, pp. 57–70, 1984.
- [21] J.-J. Fernandez, “Computational methods for materials characterization by electron tomography,” *Current Opinion in Solid State and Materials Science*, vol. 17, no. 3, pp. 93 – 106, 2013.
- [22] J. Radon, “Über die Bestimmung von Funktionen durch ihre Integralwerte längs gewisser Mannigfaltigkeiten,” *Berichte über die Verhandlungen der Königlich-Sächsischen Akademie der Wissenschaften zu Leipzig, Mathematisch-Physische Klasse*, vol. 5, no. 4, pp. 170–176, 1917.
- [23] K. M. Hanson, “On the optimality of the filtered backprojection algorithm,” *Journal of Computer Assisted Tomography*, vol. 4, no. 3, pp. 361–363, 1980.
- [24] E. Tanaka, “Quantitative image reconstruction with weighted backprojection for single photon emission computed tomography,” *Journal of Computer Assisted Tomography*, vol. 7, no. 4, pp. 692–700, 1983.
- [25] M. Radermacher, T. Wagenknecht, A. Verschoor, and J. Frank, “A new 3-D reconstruction scheme applied to the 50S ribosomal subunit of E. COLI,” *Journal of Microscopy*, vol. 141, no. 1, pp. RP1–RP2, 1986.
- [26] R. Gordon, R. Bender, and G. T. Herman, “Algebraic reconstruction techniques (ART) for three-dimensional electron microscopy and X-ray photography,” *Journal of Theoretical Biology*, vol. 29, no. 3, pp. 471 – 481, 1970.
- [27] S. Kaczmarz, “Angenäherte Auflösung von Systemen linearer Gleichungen,” *Bulletin International de l’Académie Polonaise des Sciences et des Lettres*, vol. 35, pp. 355–357, 1937.
- [28] P. Gilbert, “Iterative methods for the three-dimensional reconstruction of an object from projections,” *Journal of theoretical Biology*, vol. 36, pp. 105–117, 1972.
- [29] A. V. Lakshminarayanan and A. Lent, “Methods of least squares and SIRT in reconstruction,” *Journal of theoretical Biology*, vol. 76, pp. 267–295, 1979.
- [30] J. M. Gregor and T. Benson, “Computational analysis and improvement of SIRT,” *IEEE Transactions on Medical Imaging*, vol. 27, no. 7, pp. 918–924, 2008.
- [31] K. Batenburg, S. Bals, J. Sijbers, C. Kübel, P. Midgley, J. Hernandez, U. Kaiser, E. Encina, E. Coronado, and G. V. Tendeloo, “3D imaging of nanomaterials by discrete tomography,” *Ultramicroscopy*, vol. 109, no. 6, pp. 730 – 740, 2009.
- [32] A. Zürner, M. Döblinger, V. Cauda, R. Wei, and T. Bein, “Discrete tomography of demanding samples based on a modified SIRT algorithm,” *Ultramicroscopy*, vol. 115, pp. 41 – 49, 2012.
- [33] J. Frank and B. McEwen, “Alignment by cross-correlation,” in *Electron Tomography* (J. Frank, ed.), pp. 205–213, Springer US, 1992.
- [34] Z. Jing and F. Sachs, “Alignment of tomographic projections using an incomplete set of fiducial markers,” *Ultramicroscopy*, vol. 35, no. 1, pp. 37 – 43, 1991.
- [35] L. Houben and M. B. Sadan, “Refinement procedure for the image alignment in high-resolution electron tomography,” *Ultramicroscopy*, vol. 111, no. 9-10, pp. 1512 – 1520, 2011.
- [36] C. Sorzano, C. Messaoudi, M. Eibauer, J. Bilbao-Castro, R. Hegerl, S. Nickell, S. Marco, and J. Carazo, “Marker-free image registration of electron tomography tilt-series,” *BMC Bioinformatics*, vol. 10, no. 1, p. 124, 2009.



- [37] Plano, “Plano catalogue online, Chapter 1.” <http://www.cp-download.de/plano11/Kapitel-1.pdf>, 2014. [Online; accessed 14-October-2014].
- [38] A. Strecker, U. Salzberger, and J. Mayer, “Specimen preparation for tem. reliable method for cross-sections and brittle materials,” *Praktische Metallographie*, vol. 30, no. 10, pp. 482–95, 1993.

Chapter 4

Nanoscale Investigation on Large Crystallites in TiO₂ Nanotube Arrays and Implications for High-Quality Hybrid Photodiodes

This chapter has been published as follows:

A. Wisnet, M. Thomann, J. Weickert, L. Schmidt-Mende and C. Scheu; *Journal of Materials Science*, **2012**, 47(17), 6459-6466

Introduction

TiO₂ is a versatile metal oxide which has tunable optical and electronic properties depending on its different structures and can be produced by various fabrication routes. In recent years, several fields of application are more and more using nanostructured TiO₂, often to maximize surface areas and accordingly interface areas when combined with other materials.¹ A very important example are anodized TiO₂ nanotube arrays, amongst others used in thin-film solar cells,²⁻⁸ lithium-ion batteries,⁹ hydrogen sensors^{10,11} and water photolysis.^{12,13} A consequence of downsizing structures is a change in physical and chemical properties, which again cause modification of important electronic properties, especially the mobility of electrons along and between tubes.¹ In this regard, electron trap states have been identified to be a limiting factor.¹⁴ TiO₂ nanotube arrays have been analyzed via intensity-modulated photocurrent and intensity-modulated photovoltage spectroscopy and the elec-

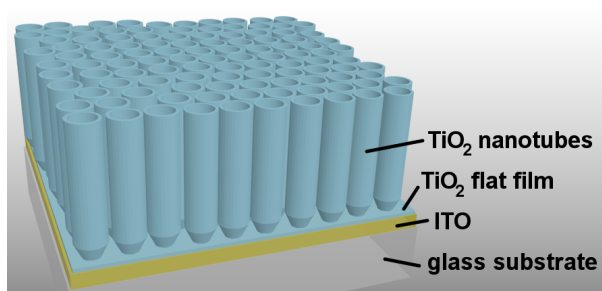


Figure 4.1: Scheme of the sample. The nanotubes are composed of anatase, while the TiO₂ flat film has rutile structure. ITO was used as conducting glass.



trons' crossing at grain boundaries was found to be severely affected by these trap states. Hence, large crystallites along the tubes are surmised to facilitate excellent electron transport.^{15,16}

The present study aims on an elucidation of the material properties of anodized nanotubes forming an array on conducting glass. A scheme of the studied layer system is shown in Figure 4.1. As previously shown in a detailed scanning electron microscopy (SEM) study, dimensions of these nanotubular arrays can be directly controlled by adjusting the conditions of electrochemical anodization, in particular the anodization bath temperature and the anodization voltage.¹⁷ Four different voltages (10 V, 15 V, 20 V and 25 V) have been applied during fabrication. They were chosen to receive inner tube diameters of around 30 nm, which is in the range of the exciton diffusion length in semiconducting polymers like poly(3-hexylthiophene) (P3HT),¹⁸ rendering them particularly interesting for applications in solid-state dye sensitized hybrid solar cells. Since an anodization voltage of 10 V resulted in a partially dissolved array composed of damaged tubes, it is not studied further.

Up to now, SEM and X-ray diffraction (XRD) were used as standard analysis methods for TiO₂ nanotube arrays, while transmission electron microscopy (TEM) has been applied on single nanotubes or dissolved arrays.^{15,19-21} Here, TEM has been chosen as primary method for analysis to gain local information about tube morphology, phase purity, crystal grain size and crystal orientation within the tubes in context of the intact array. The results are correlated to properties by fabricating hybrid solar cells composed of the TiO₂ nanotube arrays, a common ruthenium dye and P3HT. This design is adequate to gain basic information while maintaining simplicity and comparability, so that results can be appraised in context of already existent work. Current-voltage measurements have been carried out to characterize electronic behavior, with a focus on the fill factor which is influenced by electron mobility and charge recombination.

Experimental Section

TiO₂ nanotubes were synthesized on tin-doped indium oxide (ITO) coated glass substrates. ITO substrates were successively cleaned in ultrasonic baths of acetone and isopropanol for 30 min each, dried in N₂ stream and subjected to a 7 min cleaning in an O₂ plasma. Substrates were transferred to the main chamber of a NanoSystems Gamma 1000C sputter system with a base pressure of 3·10⁻⁸ Torr. Approximately 40 nm TiO₂ and 400 nm Ti were DC sputtered at 500 °C and at Ar pressures of 5 and 4 mTorr, respectively. Samples were anodized in an ethylene glycol-based electrolyte containing 0.4 wt% NH₄F and 2 vol% deionized water. Anodizations were carried out in a two electrode setup vs. a Pt counter electrode at room temperature and different anodization voltages. Anodization was stopped after complete consumption of the Ti feed substrate but before corrosion of the underlying ITO as described elsewhere.¹⁷ After anodization, samples were excessively rinsed with EtOH, slowly dried in air and annealed on a hotplate at 450 °C

in ambient air for 1 h with heating and cooling rates of 5 and 2.5 °C/min, respectively.

TEM cross-section specimens have been prepared via standard route by gluing a sandwich of the layers into a brass tube, cutting of slices, grinding, dimpling and ion milling according to Strecker et al.²² For TEM investigation, a Jeol JEM 2011 operated at 200 kV and a FEI Titan (S)TEM 80-300 operated at 300 kV have been used. The Titan is equipped with an EDAX detector for electron dispersive X-ray analysis. Off-axis dark-field (DF) images have been taken without use of beam-tilting.

Hybrid solar cells were fabricated based on TiO₂ nanotube arrays anodized at 25 V as described above. The anodized and annealed nanotubes of 500-600 nm length were immersed for 18 h in a 0.4 mM ethanol solution of the ruthenium dye Z907.²³ Subsequently, samples were rinsed with ethanol and dried in ambient air. P3HT was deposited on top of the nanostructures as hole conductor. It was prepared as a 30 mg/ml solution in chlorobenzene and spincoated at 1200 rpm for 1 min after leaving the solution on the substrate for 2 min in order to achieve sufficient wetting of the nanotubes. Immediately after spincoating, the films were annealed at 150 °C for 1 min in ambient air. Then, an approximately 50 nm thick layer of poly(3,4-ethylenedioxythiophene)-polystyrenesulfonic acid (PEDOT:PSS) was spray-deposited onto the P3HT as described previously.²⁴ In brief, PEDOT:PSS was diluted in 2-propanol at a ratio of 1:10 and the substrate was wetted with the solution via spraying. Subsequently, the film was spincoated at 800 rpm for 1 min. Solar cells were finalized by DC sputtering Ag top contacts through a shadow mask, resulting in an active area of 0.125 cm². Solar cells were tested in the dark and under illumination with a LOT-Oriel LS0106 AM 1.5g solar simulator. The light intensity was adjusted to 100 mW/cm² with a Fraunhofer Institute certified Si solar cell as a reference. Current density-voltage (I-V) characteristics were recorded using a Keithley Sourcemeter 2400 controlled by a self-written LabView program.

Results

Bright-field (BF) overview images were taken to get information about the tube length, ranging from 475 nm to 575 nm for increasing voltage (Figure 4.2). The values are in accordance to the results from SEM analysis, which has been performed earlier, although the tube length at the 15 V sample is slightly larger than expected.¹⁷ The increasing length at higher anodization voltages could be confirmed. Wall thicknesses have been measured in slightly higher magnified BF images (not shown) and result in averages of 9(±1), 9(±2) and

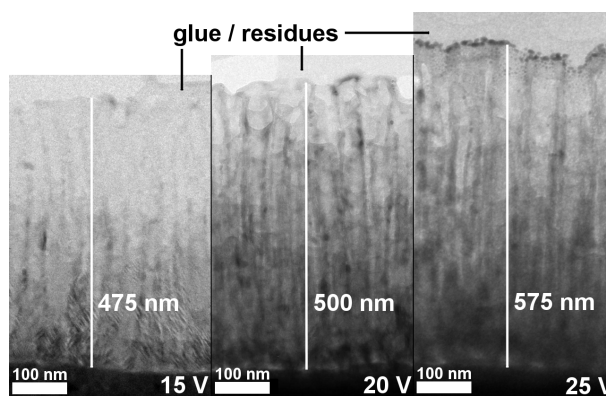


Figure 4.2: Comparison of TiO₂ tube length of three samples anodized at different voltages. Higher voltages lead to increasing length. Note the gold particles stemming from SEM characterization at the top of the 20 V and 25 V samples.



34.4. Nanoscale Investigation on Large Crystallites in TiO₂ Nanotube Arrays

12(\pm 2) nm for 15, 20 and 25 V anodization voltages, respectively. Due to the sample thickness, pore diameters were hardly distinguishable, but exemplary areas showed inner diameters of around 30 nm for all anodization voltages with a slight tendency to increase at higher voltages. Energy dispersive X-ray analysis (not shown) exhibits that the tubes contain mainly titanium and oxygen, with some traces of sodium in all samples and calcium in the 15 V sample only, which are probably residues from the sample preparation.

For a better understanding of electronic behavior, further investigation of the crystalline structure and phases was performed. Electron diffraction (ED) patterns show polycrystalline anatase. At specific areas, DF images were taken to determine crystal sizes. Figure 4.3 shows BF images, their corresponding ED patterns and DF images. The ED patterns, which have been taken at circular areas of about 650 nm diameter, show distinguishable major reflections in all cases, contrary to ring-like structures which would have been expected for fully polycrystalline samples. In accordance, the DF images taken with the indicated (200), (101) and (101) reflections of anatase confirm that a large grain size along the tube wall and a similar orientation over several nanotubes is present. Thus, although these areas show no single crystal, they appear to be composed of larger grains (including slight rotations) and some smaller grains filled in between. The crystalline appearance along the tube walls is assumed to be one of the most important features allowing a high conductivity parallel to the tube axis. For the present samples, the results indicate that the grain size along this axis is several 100 nm for individual tubes. These large crystals can only be distinguished when they are oriented near a zone axis and were observed at various positions within the sample. Groups of nanotubes with similar crystal orientation extend up to 500 nm in diameter, like the one shown in Figure 4.3c. Thus, adjacent tubes often appear with the same orientation.

BF images typically show Moiré patterns in wide areas which indicate crystallites slightly rotated by few degrees against each other. Since reflections with nearly similar angle cannot be separated by the objective aperture in ED patterns, these overlapping grains contribute to DF images, resulting in Moiré patterns here as well. Due to their appearance in clearly distinguishable nanotubes, like the one marked by an arrow in Figure 4.3c, it is assumed that the crystals of the transmitted front and back tube walls are slightly rotated with respect to each other. In addition to these findings, a trend to larger grain size at higher anodization voltages is observable. The mean length of the ten largest crystals found for each voltage are 210 nm (160-260 nm; 15 V), 260 nm (230-310 nm; 20 V) and 320 nm (250-360 nm; 25 V).

For further proof of the large crystal size, a series of HRTEM micrographs have been taken at various tubes. An exemplary one is given in Figure 4.4. The left BF image shows large parts of a nanotube which has been cut at the top during ion milling. Its darker appearance hints at an orientation parallel to a zone axis. At the closed end just below box 4, Moiré patterns are visible again, so nearly similar crystal orientations are present. Boxes numbered from 1 to 4 are set at the positions where the corresponding HRTEM micrographs, shown at the right side of Figure 4.4, have been taken. At all four

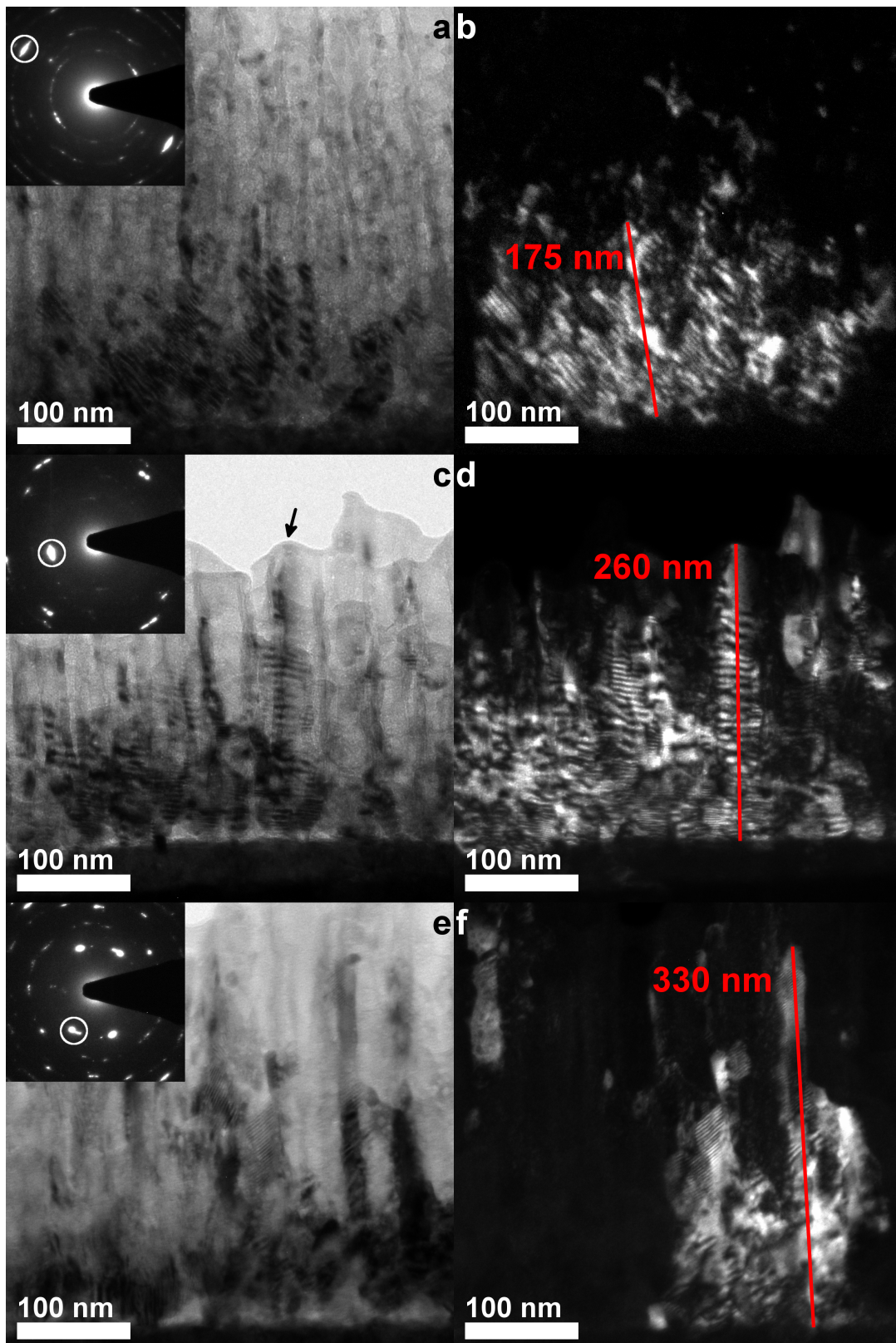


Figure 4.3: BF (left) and DF (right) images show typical grains found in samples anodized at 15 V (a, b), 20 V (c, d) and 25 V (e, f). The arrow in image c shows that the sample has been cut at this position. Corresponding ED patterns are given as insets in the BF images and the reflections which have been taken for the according DF image, namely (200) (15 V), (101) (20 V) and (101) (25 V) of anatase, are marked. Crystals which are slightly rotated to each other, but whose reflections still lie within the aperture, appear bright in the DF image. Moiré patterns are visible here, too. Selected area diffraction aperture for ED patterns corresponds to a sample area of about $0.3 \mu\text{m}^2$.



36 4. Nanoscale Investigation on Large Crystallites in TiO₂ Nanotube Arrays

positions, the lattice planes indexed as (101), (10 $\bar{1}$) and (002) are clearly visible, resulting in a view along the $\langle 010 \rangle$ zone axis. Due to the thickness of the sample, the quality of their appearance is decreasing from top to bottom, or 1 to 4, respectively. For further illustration of the similar crystalline orientation, fast Fourier transforms (FFT) have been calculated from images 1 to 4. Their center details are shown as insets in the HRTEM images. Apart from their similarity, two features deserve attention:

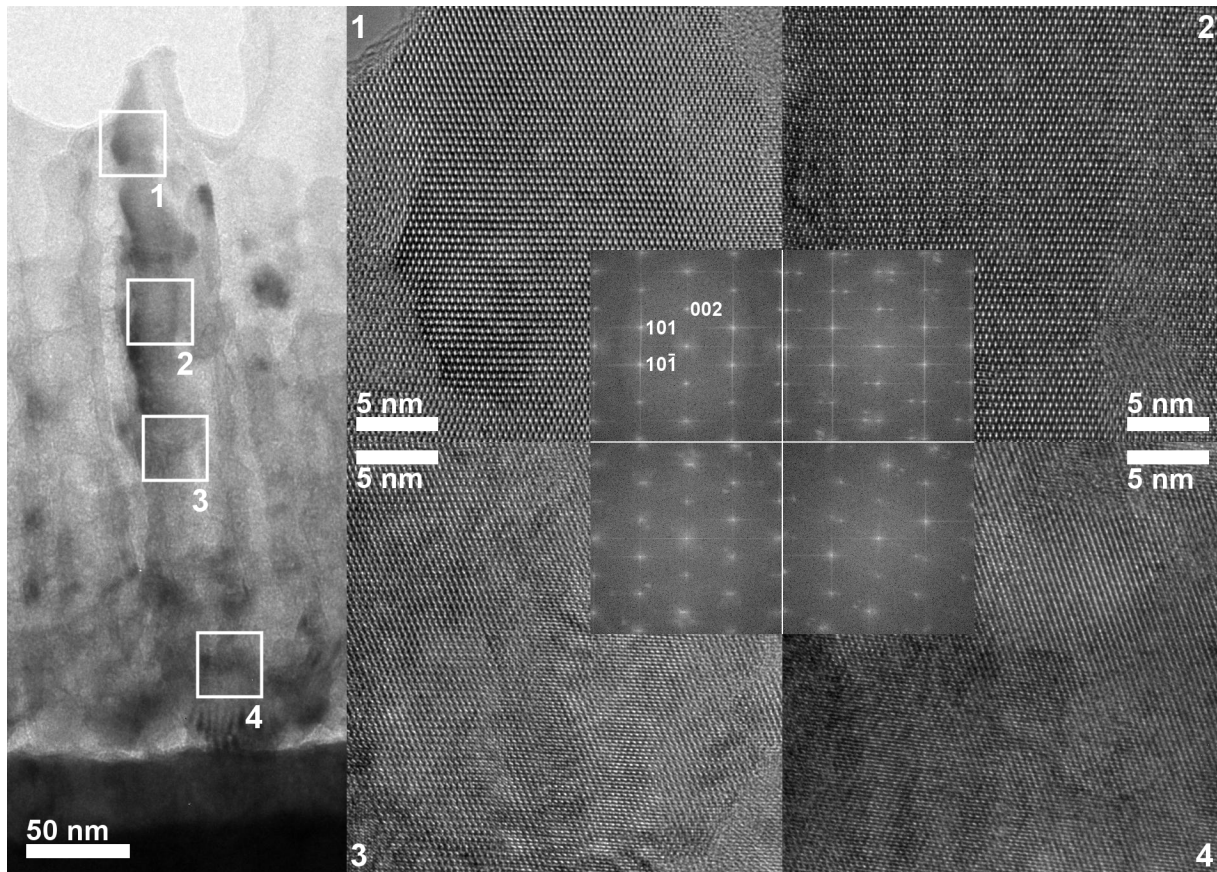


Figure 4.4: Crystallinity of a tube wall. The left side shows a BF image of a nanotube from the 20 V sample which appears to be cut in half lengthwise and has an orientation close to $\langle 010 \rangle$ zone axis. HRTEM micrographs 1-4 have been taken along the tube and details of their FFTs in the middle show a similar orientation. In area 4 the crystal is rotated about 2° compared to the first three areas.

First, the FFT in image 2 shows spots adjacent to (002) and its related reflections. This is accounted to the slightly rotated area at the left side of the HRTEM image which is partly hidden by the FFT inset. As it is visible in the BF image, this part is near the edge of the nanotube, which points towards some changes in crystal orientation in this part of the tube wall. The second interesting feature is visible when comparing the FFT of image 4 to the other three FFTs. It is rotated by 2° , which means that the bottom of the tube is composed of a crystal slightly rotated compared to the rest of the tube. The remaining reflections which do not belong to the main lattice show presence of smaller crystallites which can be part of the tube wall or may be located in front or behind the investigated tube.

To get further impressions about the crystallographic appearance of the tube walls,

areas have been sought where these parts were visible edge-on. Figure 4.5a shows an area of the 25 V sample where the tube wall is clearly recognizable. The viewing direction is parallel to the $\langle \bar{1}\bar{1}1 \rangle$ crystallographic axis. A continuous visibility of the (011) lattice planes indicates further material with nearly similar orientation. The surface of the tube wall is faceted (emphasized by white lines) and terminated with (101) planes, indicating a tube morphology with minimized surface energies.²⁵ Wall thickness can be estimated to about 7-10 nm with some visible variation.

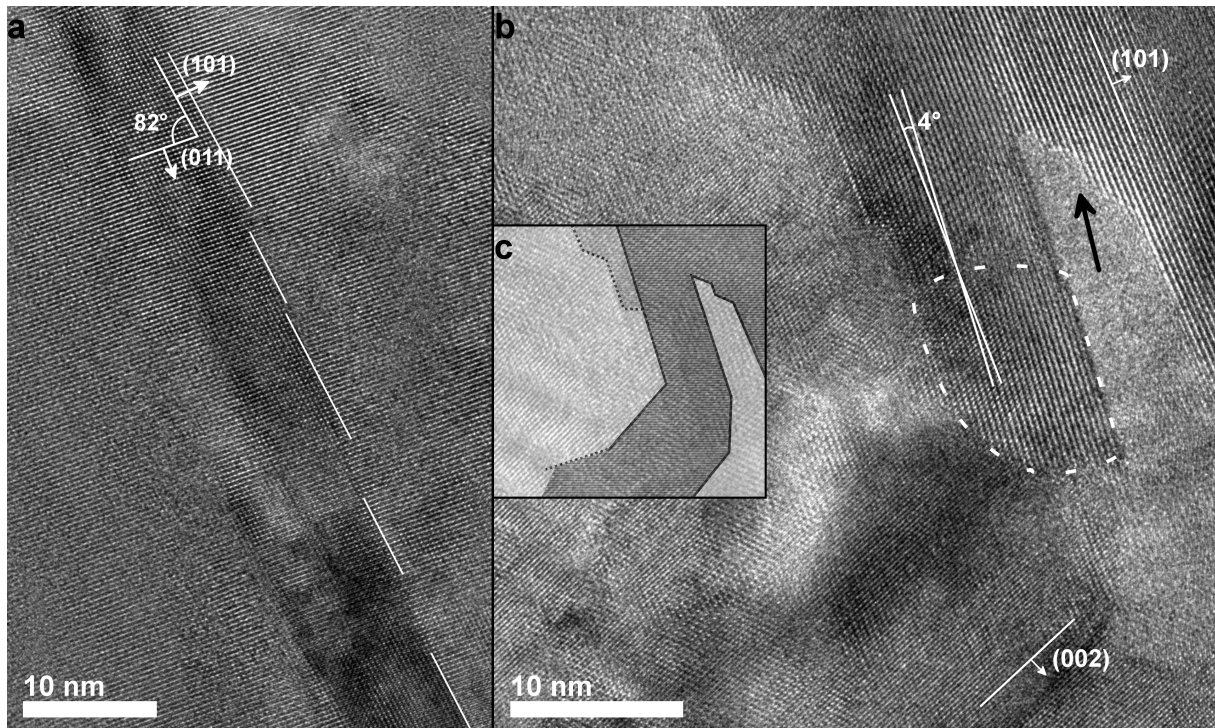


Figure 4.5: a) HRTEM micrograph of a tube wall of the 25 V sample shows faceting with a surface in (101) direction. This is known to be a preferred orientation due to minimized energies. b) HRTEM micrograph of a tube end of the 15 V sample. The area marked by a dashed white line shows a small crystal rotated by about 4° against the rest of the tube. The black arrow points out the connection to an adjacent tube. Inset c) clarifies the tube's boundaries.

Another important feature concerning the connection between adjacent nanotubes is shown in Figure 4.5b, which has been taken at the 15 V sample. To get a better impression of the surveyed area, its inset (Figure 4.5c) shows the silhouette of the tube end depicted in Figure 4.5b. The black arrow points at a direct junction of two nanotubes which clearly show the same crystallographic orientation. (101) lattice planes of the tubes possess a direct contact. This area suggests that the present material either separated into two tubes or that two adjacent nanotubes grew together during annealing. As already indicated in the DF images of Figure 4.3, annealing also caused the same crystal orientation in groups of adjacent nanotubes. A dashed white line in Figure 4.5b points out a small part of the tube wall which is slightly rotated by 4° against the remaining area. This means that some of the rotated crystals which have been observed by Moiré fringes may also be caused by minor bending effects within the tubes.



In order to evaluate the suitability of the nanotube arrays for applications in hybrid solar cells, they were sensitized with the widely-used ruthenium dye Z907 and infiltrated with P3HT, a hole conducting, highly absorbing conjugated polymer, well-known from applications in fully organic bulk heterojunction solar cells.^{26,27} Figure 4.6 shows I-V curves of a typical device, where the solid line represents the cell tested under simulated solar illumination. Only moderate power conversion efficiencies (PCEs) of approximately 0.2 % are found, which is mainly caused by the small short circuit current densities (I_{SC}), whereas the cells show reasonable open circuit voltages (V_{OC}) between 0.5 and 0.55 V and high fill factors (FF) of around 60 %.

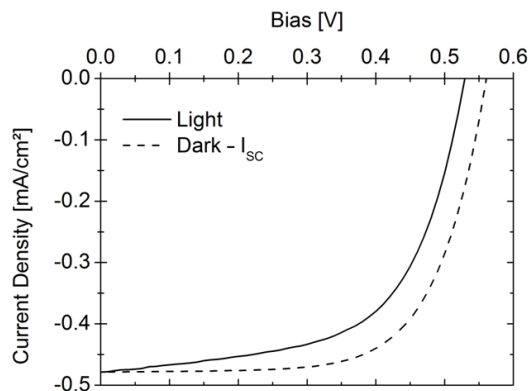


Figure 4.6: Current density - voltage characteristic of a typical hybrid solar cell with P3HT as hole conductor based on TiO₂ nanotubes anodized at 25 V. The solid line corresponds to illumination with simulated solar light, whereas the dashed line is the I-V curve measured in the dark and shifted by the photocurrent measured under solar illumination.

Discussion

One of the most important questions of the foregoing analysis is the conductivity of the TiO₂ nanotubes based on a purposive view on material properties. This is of particular interest when using TiO₂ nanotubes as structured layer in dye-sensitized or hybrid polymer-metal oxide solar cells. In this regard, the elaborated results are very promising. All three anodization voltages resulted in grain sizes which exceed the findings of previous studies. Albu et al.¹⁹ as well as Li et al.¹⁶ observed and expected large crystals of more than 100 nm, although the former conducted TEM measurements only on single nanotubes detached from the substrate and the latter assumed large crystals due to an absent peak broadening in XRD spectra. However, both investigations have been conducted at considerably larger structures (length 12-25 μm ; diameter ≈ 150 nm) than the ones presented here. Hsiao et al.¹⁵ also used larger structures during their research and derived grain sizes of $35(\pm 1)$ nm from the Debye-Scherrer equation applied to their XRD patterns. They, as well as Albu et al., observed a random crystal orientation. From our observations by ED, DF imaging and HRTEM, we could show that there is a strong correlation of the crystal orientation within one cluster of nanotubes. Further investigation is required to provide proof of a possible tendency towards tube surfaces terminating with (101) planes.

As mentioned previously, large crystallites along the tube walls facilitate excellent electron conductivity from top to bottom of the tube, but also the lateral expansion of same crystal orientations can be beneficial to charge transport. This might be the case e.g. if the charge transfer from one tube end to the electrode is blocked for any reason. Here,

the electrons can easily circumvent the affected contact by conduction to an adjacent nanotube. In case of polycrystalline material with grain sizes of 5-15 nm, charge trapping resulting in a conductivity-restraining potential or increased charge recombination would be inevitable. One remaining question is, how much of an impact on conductivity is made by bending as well as small crystal rotations along the tube walls. However, this should be only a minor decline compared to an alternative appearance of distinct grain boundaries.

Another point which was shown in our work is the sample structure's dependence on the anodization voltage. Increasing the voltage resulted in an increased tube length. Wider tube diameters and thicker tube walls as predicted in previous studies¹⁷ could not be discerned with absolute certainty. What in turn could be observed is an increasing crystal size at increased anodization voltage. This results in a potential trade-off: For many applications, a high surface area of the TiO₂ nanotubes is desired. Taking into account decreasing tube dimensions like lower pore-to-pore distance and tube wall thickness at lower voltages, these would basically be the favored ones. However, as these applications often are in need of good conductivity, higher anodization voltages would be preferable. In the end, a suitable compromise ought to be found in an empirical way, although the effect of other anodization parameters like bath temperature or electrolyte concentration should not be disregarded. It is obvious that, at least concerning the lower limit, extreme anodization voltages are not expedient. Evaluating these results, it must be pointed out that TEM sample preparation is rather harsh, and mechanical handling or ion milling can induce damage or bending of the tube structure. This means that the reported crystalline appearance may be worse than it is in an untreated sample.

The low photocurrents of our P3HT-based hybrid solar cells can be attributed to two main issues. Point one, we did not optimize the structure filling, which most likely leads to the lower parts of the relatively long tubes being not infiltrated with P3HT. Thus, the resulting interfacial area between polymer and metal oxide is reduced. Additionally, due to being sensitized with Z907, the TiO₂ that is not covered with P3HT is filtering light. Consequently the light intensity is reduced at the sites where charges are actually separated, since incident light goes through the lower part of the nanotubes first. More importantly point two, the interface between TiO₂ and P3HT is not optimized, probably resulting in a comparatively low exciton-to-charge conversion efficiency. Even though Z907 has proven highly efficient in solid state dye-sensitized solar cells, other sensitizers appear to be better suited for applications with P3HT.^{23,28} For our preliminary experiments, however, we focused on the well-known standard material Z907 since its properties have been extensively described in literature.²⁹ Besides, for the sake of simplicity we did not subject the nanotubes to an additional TiCl₄ treatment or use any additives like 4-*tert*-butylpyridine or lithium salts, all of which are known to have positive effects on the cell's V_{OC} and especially I_{SC}.^{30,31}

Nevertheless, we find FFs of around 60 % for our solar cells, which are remarkable within the aforementioned context. High FFs indicate slow charge carrier recombination and high and balanced charge carrier mobilities, which prevent the built-up of space charge



regions.^{32,33} This is especially interesting when comparing these values to FFs reported for solar cells based on mesoporous TiO₂ and P3HT. Even though significantly higher V_{OC} and I_{SC} have been reported for such systems, the FF appears to be smaller there. Coakley et al. reported a FF of 51 % for a solar cells with I_{SC} of 1.4 mA/cm² and V_{OC} of 0.72 V, i.e. much higher PCE than ours.³⁴ Zhu et al. could show PCEs of 2.6 % with mesoporous TiO₂ and P3HT using organic dyes and additives.³⁵ There, they found an even higher FF of 61 %. However, these high FFs were possible only for the ideal combination of additives, whereas FF between 29 and 55 % have been reported if no or only one type of additive was used. Even lower FFs are present when directly blending TiO₂ nanoparticles with P3HT.^{36,37} Mor et al. investigated TiO₂ nanotube arrays which are closely related to our system.⁷ While focusing on the influence of differently concentrated dyes, the measured FFs in that work are between 50 and 70 %.

We assume that in general anodized TiO₂ nanotubes feature larger crystals than those which occur in mesoporous TiO₂. In addition, areas of similar oriented tubes are present in dependence of an existing contact between them. This results in high electron mobility. In contrast, average grain sizes in mesoporous TiO₂ are expected to be in range of only 10-30 nm and do not exceed the diameter of individual nanoparticles.³⁸ Accordingly, considerably slower electron transport is expected in these structures.

Finally the high diode quality of solar cells based on TiO₂ nanotube arrays is also apparent when comparing the I-V curve under illumination with the curve measured in the dark and shifted by I_{SC}, shown as dashed line in Figure 4.6. For an ideal solar cell without recombination losses these curves should overlay.³⁹ Even though this is not the case for our solar cells, the main difference lies in the higher virtual V_{OC} of the shifted dark curve, whereas the general shape of the curves is very similar. This indicates only small recombination losses.

Conclusion

Our TEM analysis on anodized TiO₂ nanotubes shows that they possess an anatase crystal structure and grain sizes considerably exceeding anticipated values, with possible extents of more than 300 nm along tube walls, which is remarkable at tube lengths of around 500 nm. Nearly similar oriented, though slightly rotated crystals have been found over wide areas. This has to our knowledge never been reported for nanostructured TiO₂ anatase system so far and can be explained by inter tube connections which enable an extension of crystal grains across tube edges. These features provide good preconditions for the transfer of electrons towards the electrode, as was demonstrated by our solar cell measurements. In addition to crystal properties, the dependence between anodization voltage and tube dimensions i.e. length and to a certain extent wall thickness, meaning longer tubes and thicker tube walls for higher voltages, was shown.

All this leads to the conclusion that the efforts of implementing this tube system into sophisticated applications like hybrid solar cells should be well rewarding, since perfor-

mance is expected to be excellent after further optimization of dye/polymer combination and respective treating. In the end, electrons have to be removed swiftly from interfaces to avoid charge recombination and realize efficient and loss-free photo-current generation.

Addition to the Published Data

In addition to the three samples discussed in the previous sections, another sample which was anodized at 10 V has been investigated. First of all, at some areas, the long duration of the anodization causes the underlying FTO to corrode (see figure 4.7). As seen in figure 4.8, the morphology of the tubes is clearly distorted compared to the previous growth conditions. The resulting length of the nanotubes is visibly shorter, since the process of anodization dissolves the material over time. As an anodization voltage of 10 V causes a slower conversion rate from Ti to TiO_2 and therefore longer reaction times, this is an obvious effect. On the lower right, there is also some damage in the TiO_2 flat film visible. Taking a closer look at the tubes, figure 4.9 shows that the thickness of the tube walls is with 5-6 nm considerably smaller than those of the previous samples. Some tubes appear amorphous, as the one in figure 4.9a, while there can be found nanotubes with a crystallinity which can be attributed to anatase.

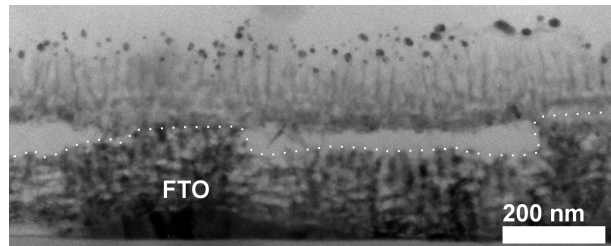


Figure 4.7: Damaged FTO is found as an indication for the harmfulness of a long anodization step.

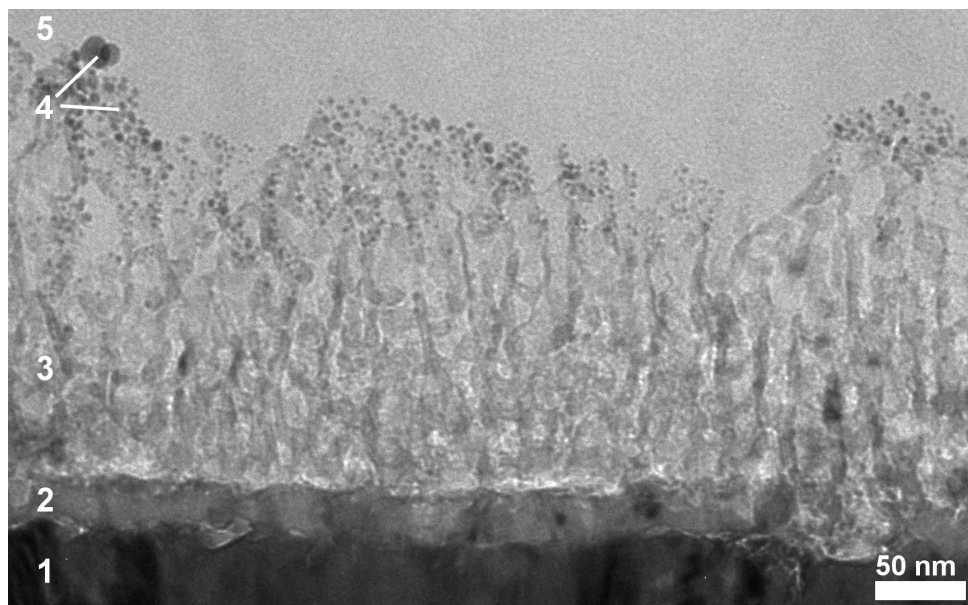


Figure 4.8: Bright-field image of a TiO_2 nanotube array which has been anodized at 10 V. From bottom to top there is the FTO layer (1), the TiO_2 thin-film (2), the TiO_2 nanotubes, gold nanoparticles stemming from sputtering for SEM (4) and glue (5).



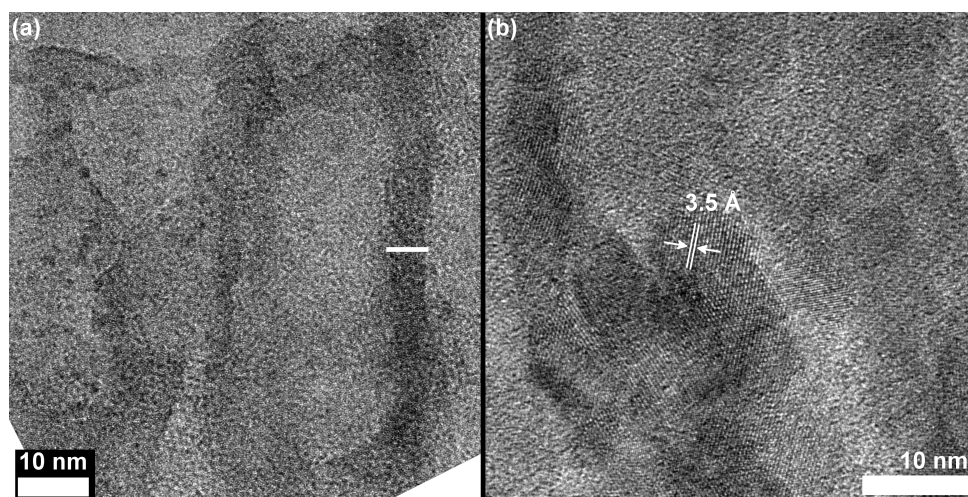


Figure 4.9: HRTEM images of the 10 V sample shows the residues of tubes. a) The tube wall thickness is around 6 nm. b) Some crystalline areas remain which are most likely anatase.

Bibliography

- [1] X. Chen and S. S. Mao, "Titanium dioxide nanomaterials: Synthesis, properties, modifications, and applications," *Chemical Reviews (Washington, DC, U. S.)*, vol. 107, no. 7, pp. 2891–2959, 2007.
- [2] G. K. Mor, O. K. Varghese, M. Paulose, K. Shankar, and C. A. Grimes, "A review on highly ordered, vertically oriented TiO₂ nanotube arrays: Fabrication, material properties, and solar energy applications," *Solar Energy Materials and Solar Cells*, vol. 90, no. 14, pp. 2011–2075, 2006.
- [3] P. Roy, S. Berger, and P. Schmuki, "TiO₂ nanotubes: Synthesis and applications," *Angewandte Chemie International Edition*, vol. 50, no. 13, pp. 2904–2939, 2011.
- [4] C. A. Grimes, "Synthesis and application of highly ordered arrays of TiO₂ nanotubes," *Journal of Materials Chemistry*, vol. 17, no. 15, pp. 1451–1457, 2007.
- [5] B.-Y. Yu, A. Tsai, S.-P. Tsai, K.-T. Wong, Y. Yang, C.-W. Chu, and J.-J. Shyue, "Efficient inverted solar cells using TiO₂ nanotube arrays," *Nanotechnology*, vol. 19, no. 25, pp. 255202/1–255202/5, 2008.
- [6] J. Weickert, R. B. Dunbar, H. C. Hesse, W. Wiedemann, and L. Schmidt-Mende, "Nanostructured organic and hybrid solar cells," *Advanced Materials (Weinheim, Ger.)*, vol. 23, no. 16, pp. 1810–1828, 2011.
- [7] G. K. Mor, J. Basham, M. Paulose, S. Kim, O. K. Varghese, A. Vaish, S. Yoriya, and C. A. Grimes, "High-efficiency Förster resonance energy transfer in solid-state dye sensitized solar cells," *Nano Letters*, vol. 10, no. 7, pp. 2387–2394, 2010.
- [8] O. K. Varghese, M. Paulose, and C. A. Grimes, "Long vertically aligned titania nanotubes on transparent conducting oxide for highly efficient solar cells," *Nature Nanotechnology*, vol. 4, no. 9, pp. 592–597, 2009.
- [9] G. F. Ortiz, I. Hanzu, P. Knauth, P. Lavela, J. L. Tirado, and T. Djenizian, "TiO₂ nanotubes manufactured by anodization of Ti thin films for on-chip Li-ion 2D microbatteries," *Electrochimica Acta*, vol. 54, no. 17, pp. 4262–4268, 2009.
- [10] G. K. Mor, M. A. Carvalho, O. K. Varghese, M. V. Pishko, and C. A. Grimes, "A room-temperature TiO₂-nanotube hydrogen sensor able to self-clean photoactively from environmental contamination," *Journal of Materials Research*, vol. 19, no. 2, pp. 628–634, 2004.
- [11] G. K. Mor, O. K. Varghese, M. Paulose, K. G. Ong, and C. A. Grimes, "Fabrication of hydrogen sensors with transparent titanium oxide nanotube-array thin films as sensing elements," *Thin Solid Films*, vol. 496, no. 1, pp. 42–48, 2005.

- [12] O. K. Varghese, M. Paulose, K. Shankar, G. K. Mor, and C. A. Grimes, "Water-photolysis properties of micron-length highly-ordered titania nanotube-arrays," *Journal of Nanoscience and Nanotechnology*, vol. 5, no. 7, pp. 1158–1165, 2005.
- [13] J.-J. Gong, Y.-K. Lai, and C.-J. Lin, "Electrochemically multi-anodized TiO₂ nanotube arrays for enhancing hydrogen generation by photoelectrocatalytic water splitting," *Electrochimica Acta*, vol. 55, no. 16, pp. 4776–4782, 2010.
- [14] J. R. Jennings, A. Ghicov, L. M. Peter, P. Schmuki, and A. B. Walker, "Dye-sensitized solar cells based on oriented TiO₂ nanotube arrays: Transport, trapping, and transfer of electrons," *Journal of the American Chemical Society*, vol. 130, no. 40, pp. 13364–13372, 2008.
- [15] P.-T. Hsiao, Y.-J. Liou, and H. Teng, "Electron transport patterns in TiO₂ nanotube arrays based dye-sensitized solar cells under frontside and backside illuminations," *Journal of Physical Chemistry C*, vol. 115, no. 30, pp. 15018–15024, 2011.
- [16] K.-L. Li, Z.-B. Xie, and S. Adams, "Fast charge transport of titania nanotube arrays in dye-sensitized solar cells," *Zeitschrift für Kristallographie*, vol. 225, no. 05, pp. 173–179, 2010.
- [17] J. Weickert, C. Palumbiny, M. Nedelcu, T. Bein, and L. Schmidt-Mende, "Controlled growth of TiO₂ nanotubes on conducting glass," *Chemistry of Materials*, vol. 23, no. 2, pp. 155–162, 2011.
- [18] P. W. M. Blom, V. D. Mihailetschi, L. J. A. Koster, and D. E. Markov, "Device physics of polymer:fullerene bulk heterojunction solar cells," *Advanced Materials (Weinheim, Ger.)*, vol. 19, no. 12, pp. 1551–1566, 2007.
- [19] S. P. Albu, H. Tsuchiya, S. Fujimoto, and P. Schmuki, "TiO₂ nanotubes - annealing effects on detailed morphology and structure," *European Journal of Inorganic Chemistry*, no. 27, pp. 4351–4356, 2010.
- [20] J. Yu, G. Dai, and B. Cheng, "Effect of crystallization methods on morphology and photocatalytic activity of anodized TiO₂ nanotube array films," *Journal of Physical Chemistry C*, vol. 114, no. 45, pp. 19378–19385, 2010.
- [21] A. Jaroenworoluck, D. Regonini, C. R. Bowen, and R. Stevens, "A microscopy study of the effect of heat treatment on the structure and properties of anodized TiO₂ nanotubes," *Applied Surface Science*, vol. 256, no. 9, pp. 2672–2679, 2010.
- [22] A. Strecker, U. Salzberger, and J. Mayer, "Specimen preparation for TEM. reliable method for cross-sections and brittle materials," *Praktische Metallographie*, vol. 30, no. 10, pp. 482–95, 1993.
- [23] L. Schmidt-Mende, S. M. Zakeeruddin, and M. Grätzel, "Efficiency improvement in solid-state-dye-sensitized photovoltaics with an amphiphilic ruthenium-dye," *Applied Physics Letters*, vol. 86, no. 1, p. 013504, 2005.
- [24] J. Weickert, H. Sun, C. Palumbiny, H. Hesse, and L. Schmidt-Mende, "Spray-deposited PEDOT:PSS for inverted organic solar cells," *Solar Energy Materials and Solar Cells*, vol. 94, no. 12, pp. 2371–2374, 2010.
- [25] M. Lazzeri, A. Vittadini, and A. Selloni, "Structure and energetics of stoichiometric TiO₂ anatase surfaces," *Physical Reviews B*, vol. 63, no. 15, p. 155409, 2001.
- [26] G. Dennler, M. C. Scharber, and C. J. Brabec, "Polymer-fullerene bulk-heterojunction solar cells," *Advanced Materials*, vol. 21, no. 13, pp. 1323–1338, 2009.
- [27] H. Hoppe and N. S. Sariciftci, "Polymer solar cells," *Advances in Polymer Science*, vol. 214, pp. 1–86, 2008.
- [28] J. Weickert, F. Auras, T. Bein, and L. Schmidt-Mende, "Characterization of interfacial modifiers for hybrid solar cells," *Journal of Physical Chemistry C*, vol. 115, no. 30, pp. 15081–15088, 2011.
- [29] A. Hagfeldt, G. Boschloo, L. Sun, L. Kloo, and H. Pettersson, "Dye-sensitized solar cells," *Chemical Reviews*, vol. 110, no. 11, pp. 6595–6663, 2010.
- [30] G. K. Mor, S. Kim, M. Paulose, O. K. Varghese, K. Shankar, J. Basham, and C. A. Grimes, "Visible to near-infrared light harvesting in TiO₂ nanotube array-P3HT based heterojunction solar cells," *Nano Letters*, vol. 9, no. 12, pp. 4250–4257, 2009.
- [31] A. Abrusci, I. Ding, M. Al-Hashimi, T. Segal-Peretz, M. McGehee, M. Heeney, G. Frey, and H. Snaith, "Facile infiltration of semiconducting polymer into mesoporous electrodes for hybrid solar cells," *Energy & Environmental Science*, vol. 4, pp. 3051–3058, 2011.



- [32] M. S. Kim, B. G. Kim, and J. Kim, "Effective variables to control the fill factor of organic photovoltaic cells," *ACS Applied Materials & Interfaces*, vol. 1, no. 6, pp. 1264–1269, 2009.
- [33] V. D. Mihailesti, J. Wildeman, and P. W. M. Blom, "Space-charge limited photocurrent," *Physical Review Letters*, vol. 94, no. 12, p. 126602, 2005.
- [34] K. Coakley and M. McGehee, "Photovoltaic cells made from conjugated polymers infiltrated into mesoporous titania," *Applied Physics Letters*, vol. 83, no. 16, pp. 3380–3382, 2003.
- [35] R. Zhu, C. Jiang, B. Liu, and S. Ramakrishna, "Highly efficient nanoporous TiO₂-polythiophene hybrid solar cells based on interfacial modification using a metal-free organic dye," *Advanced Materials*, vol. 21, no. 9, pp. 994–1000, 2009.
- [36] J. Boucle, S. Chyla, M. S. P. Shaffer, J. R. Durrant, D. D. C. Bradley, and J. Nelson, "Hybrid solar cells from a blend of poly(3-hexylthiophene) and ligand-capped TiO₂ nanorods," *Advanced Functional Materials*, vol. 18, no. 4, pp. 622–633, 2008.
- [37] S. Günes, N. Marjanovic, J. Nedeljkovic, and N. Sariciftci, "Photovoltaic characterization of hybrid solar cells using surface modified TiO₂ nanoparticles and poly(3-hexyl)thiophene," *Nanotechnology*, vol. 19, p. 424009, 2008.
- [38] S. Guldin, S. Hüttner, P. Tiwana, M. Orilall, B. Ülgüt, M. Stefik, P. Docampo, M. Kolle, G. Divitini, and C. Ducati, "Improved conductivity in dye-sensitised solar cells through block-copolymer confined TiO₂ crystallisation," *Energy & Environmental Science*, vol. 4, pp. 225–233, 2010.
- [39] R. A. Street and M. Schoendorf, "Interface state recombination in organic solar cells," *Physical Reviews B*, vol. 81, no. 20, p. 205307, 2010.

Chapter 5

Model for Hydrothermal Growth of Rutile Wires and the Associated Development of Defect Structures

This chapter has been published as follows:

A. Wisnet, S. B. Betzler, R. V. Zucker, J. A. Dorman, P. Wagatha, S. Matich, E. Okunishi, L. Schmidt-Mende and C. Scheu; *Crystal Growth & Design*, **2014**, *14*(9), 4658-4663

Introduction

Hydrothermal growth of nanostructured metal oxides is a popular method to obtain homogeneous samples with large surface area. The resulting nanostructures can appear as free-floating porous spheres,¹ cubes² or wires,³⁻⁵ or as particle arrays attached to a substrate.^{6,7} Amongst the latter, TiO₂ nanowire arrays are of interest for a wide range of applications.⁸⁻¹⁰ Dye-sensitized solar cells can benefit from elongated, highly-crystalline rutile nanowire arrays because their high aspect ratio maximizes the surface area for electron-hole pair generation, while the material properties of TiO₂ ensure non-toxicity, chemical stability and good electron transport.¹¹⁻¹³

Methods to produce TiO₂ nanowires are well-developed. Hosono et al. presented a way to grow TiO₂ nanowires on borosilicate glass.¹⁴ Later, Feng et al. were the first to show a solvothermal fabrication of rutile nanowire arrays on conducting glass for use in dye-sensitized solar cells reaching efficiencies up to 5 %. HCl was found to be essential for the synthesis, which leads to the conclusion that chloride ions play a major role for the wires' anisotropic growth along the [001] direction.¹¹ Further investigations on hydrothermal growth conditions optimized the H₂O/HCl solvent concentration and the annealing treatment at elevated temperatures for solar cell applications.^{12,15-17} A detailed growth mechanism for solvothermally-synthesized rutile nanowires was proposed by Li et al., although with a focus on the development of branches occurring at the {101} facets of



the nanowires. Their model assumed that free-floating anatase particles form first, then attach to the growing rutile wire in one of two possible orientations, and then transform to rutile.¹⁸

In this paper, we present an alternative growth model, supported by detailed scanning electron microscopy (SEM) and transmission electron microscopy (TEM) observations of the defect cascades present in hydrothermally-grown rutile nanowires.

Experimental

For this work, the synthesis procedure presented by Liu et al. was followed.¹⁵ A fluorine-doped tin oxide (FTO) substrate was cleaned using acetone, isopropanol and ethanol and placed vertically in a Teflon liner. 5 mL of distilled water was mixed with 5 mL concentrated HCl (37 wt%). NaCl was added in varying concentrations up to 0.25 mol/L. 0.1 – 0.2 mL titanium butoxide, Ti(OBu)₄ (Sigma Aldrich), was added under vigorous stirring, then the liquid was transferred to the Teflon liner containing the substrate, which was subsequently inserted into an autoclave. The solution was treated at a temperature of 150 °C for three hours in an oven. All chemicals were used as delivered by the supplier without further purification. The initial concentration of the Ti source is kept low in comparison to the concentration of HCl in order to maintain a constant pH throughout the reaction. SEM was performed in a Zeiss Gemini Ultra field emission scanning electron microscope equipped with an in-lens detector at 4 kV. TEM observations were performed in an FEI Titan S/TEM 80-300 equipped with an EDAX thin window energy dispersive X-ray (EDX) detector, operated at 300 kV, and for the secondary electron images a double corrected JEOL JEM-ARM200F equipped with a secondary electron detector was used. TEM sample preparation was performed by scratching the wires from the substrate with a scalpel onto TEM grids coated with a holey carbon film. Cross-sections of the wires for TEM analysis were prepared with a Zeiss NVision focused ion beam. Growth conditions for the samples shown (A-C) can be found in Table 5.1 in the Supporting Information.

Results

Fig. 5.1a shows a typical top-view SEM image of a nanowire array grown for 3 h (sample A). By varying synthesis time and reactant concentration, different lengths (Fig. 5.1b) and widths (Figs. 5.1b, c) can be achieved. After a time of approx. 1.5 – 2 h, wire growth begins abruptly (also see supplemental Figure 1). The delay could be due to the time it takes for the synthesis solution to reach the reaction temperature, as the Teflon liner is thermally insulating. Wire length and width increase with elapsed time but plateau after approx. 8 h. This could be because the starting Ti(OBu)₄ has been exhausted, or that defects prevent further growth (this possibility is addressed further in the Discussion section). The wires contain roughly 1 % of the total Ti in the system, but free-floating

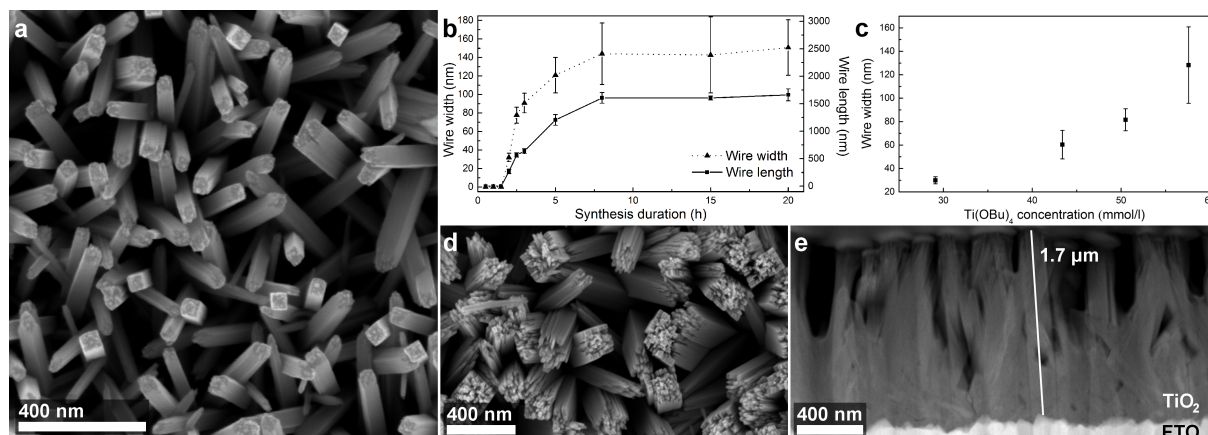


Figure 5.1: a) SEM top-view micrograph of rutile nanowires as-grown on the FTO substrate. b) Wire length & width as a function of synthesis duration. $c_{\text{Ti}(\text{OBu})_4} = 0.58 \text{ mmol/L}$ c) Wire width as a function of the initial $\text{Ti}(\text{OBu})_4$ concentration. $t_{\text{synthesis}} = 3 \text{ h}$ d) SEM top-view micrograph of a sample displaying the distinct defect structure. e) STEM cross-section view of the sample shown in d).

particles and growth on the Teflon walls may have incorporated the remaining Ti. No detectable Cl signal was found in any EDX measurements performed on the wires, whether in bulk or at defects (not shown). A rough, blocky morphology can already be recognized at the wire tops in Fig. 5.1a, but these features are more evident after longer synthesis times. Figs. 5.1d and e show SEM and scanning TEM (STEM) micrographs of a sample grown for 20 h, which prominently displays the characteristic defect structure (sample B).

The TEM bright field (BF) image shown in Fig. 5.2a is of a rutile nanowire broken off of the array (sample C). This nanowire shows a V-shaped defect cascade that begins at the center of the wire (region highlighted in Fig. 5.2e) and radiates out as growth proceeds. Fig. 5.2c indicates that the resulting defects are free internal surfaces, and the intervening regions are single crystalline. We refer to these subwires as "fingers" and to the free internal surfaces generally as "defects". The fingers are all in the same orientation and connect continuously to the bottom of the wire. The electron diffraction (ED) pattern (Fig. 5.2b) of the wire shown in Fig. 5.2a was taken in the

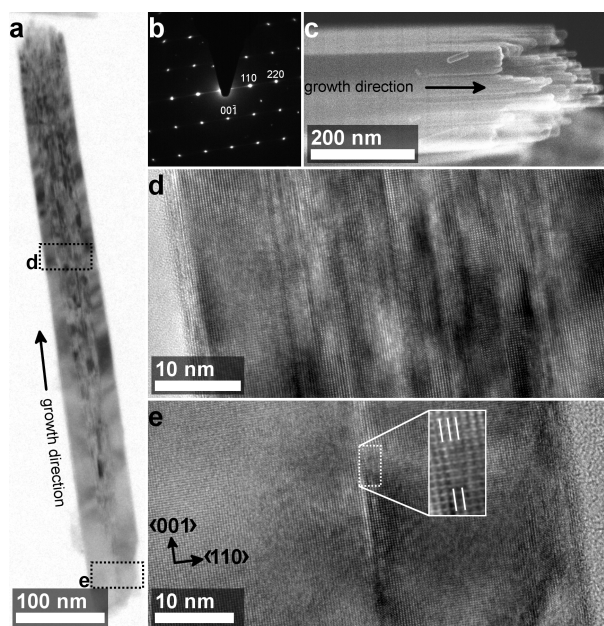


Figure 5.2: a) BF image of a rutile nanowire on carbon film. b) The ED pattern of the sample shown in a) indicates that the growth direction is [001] and the streaks emanating from the {110} reflexes arise from the small width of the fingers. c) The secondary electron TEM image of a different wire tip shows the fingers breaching the {110} surfaces just below the wire top. d) HRTEM micrograph of the region about 250 nm below the top of the wire. A multitude of overlapping fingers is visible. e) HRTEM micrograph at the bottom of the wire. A single defect starts the cascade out of a single-crystalline area. The inset shows the involved edge dislocation (filtered image).



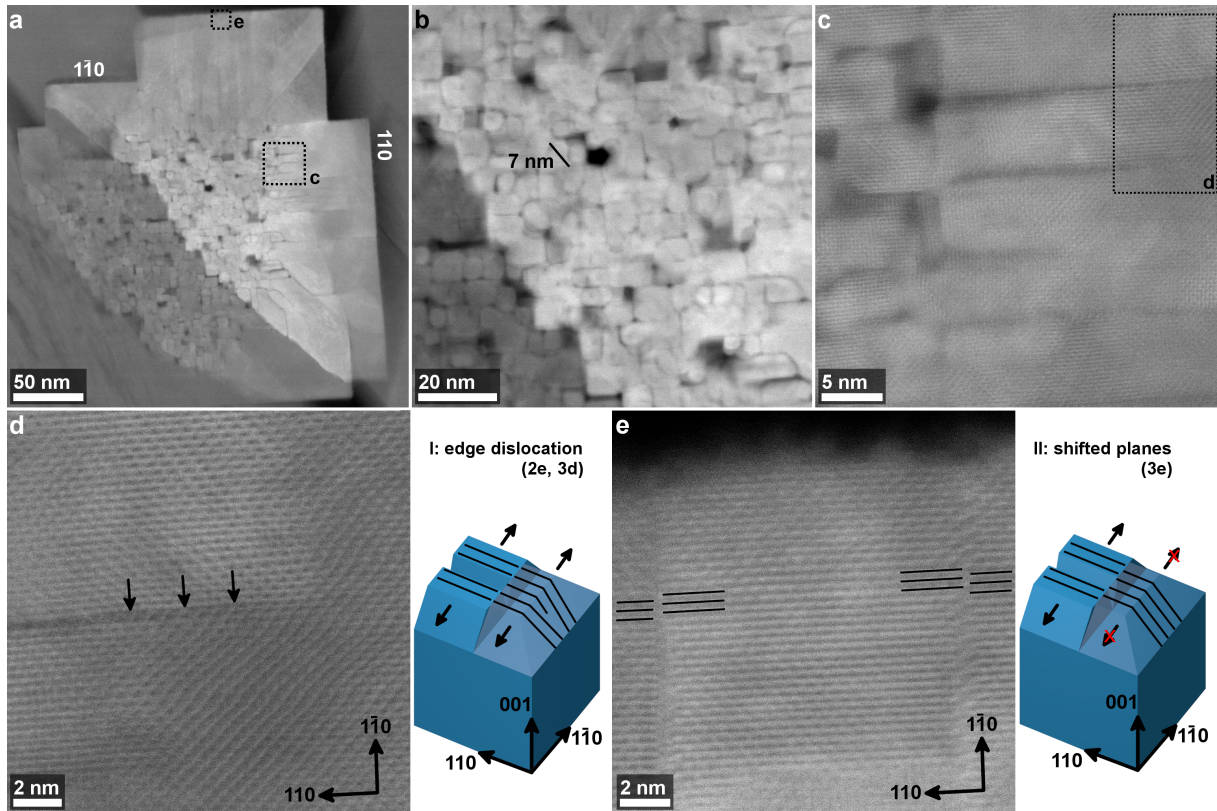


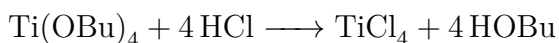
Figure 5.3: a) STEM image of a wire cross-section, image taken in the $\langle 001 \rangle$ axis. There is a concentration of fingers in the center. b) Higher magnification of the wire shown in a). The fingers have rectangular base areas with a diagonal width of about 7 nm . c) Detail of a) at the boundary between fingers and single-crystalline area. d) Detail of a defect which shows that an additional plane is inserted at the single-crystalline area (marked by arrows). This leads to an edge dislocation in the adjacent area, as shown in the schematic. e) Detail of the interface between fingers shows a shift by half of a lattice plane in the $[1\bar{1}0]$ direction along the arrow. This results when the adjacent crystal does not compensate the defect by an inserted lattice plane.

$[1\bar{1}0]$ zone axis and demonstrates growth along the $[001]$ direction as well as confirming that the wires have the rutile crystal structure. While the reflexes in the diffraction pattern of the bottom of the wire are spots, streaks are observed in the diffraction patterns of the middle and top part of the nanowire (see supplemental Figure 2). The streaks arise due to elongated rods in reciprocal space which are caused by the small width of the fingers compared to their length. The direction of the streaks is perpendicular to the (110) surface of the fingers, i.e., along the $\langle 110 \rangle$ directions. A secondary-electron TEM micrograph (Fig. 5.2c) gives a three-dimensional impression of a nanowire tip (sample B) and indicates a width of around $5\text{--}10 \text{ nm}$ for the fingers. High resolution TEM (HRTEM) images of the defect structure are shown in Figs. 5.2d and e (sample C). Fig. 5.2d shows the area roughly 250 nm below the top. Here, a large number of fingers overlap and the outer edges of the wire are still single crystalline. Fig. 5.2e shows the single-crystalline area around a first line defect, which is an edge dislocation as emphasized by the filtered detail (inset). Fig. 5.3a and b show STEM micrographs of a wire in cross-section, about $200\text{--}300 \text{ nm}$ below the wire tip (sample B). Here, fingers are densely packed at the center of the wire, and cavities between them are visible. The lower left part of the wire

is in weaker contrast because of a fracture running diagonally through the wire, removing a part of it parallel to the image plane. The fingers have diagonal widths around 7 nm (statistics from 50 fingers) and have rectangular bases with partially rounded edges. Fig. 5.3c depicts the border area between the fingers and the single-crystalline area, which is partly penetrated by defects. Fig. 5.3d shows that an additional (110) crystal plane was inserted to compensate for the widening caused by the internal free surface, which was accommodated by an edge dislocation as shown in Fig. 5.2e. Fig. 5.3e indicates that fingers or larger crystallites can be shifted by half of the lattice plane spacing relative to each other when no additional lattice plane is inserted in the single-crystalline area adjacent to the defect.

Discussion

In the following, we present a possible mechanism to explain the formation of the finger structures. First, the titanium butoxide is transformed to TiCl_4 in solution:



Seeding of the wires can be performed by small crystals, whether formed in solution or attached to the FTO. A typical crystal shape associated with rutile is depicted in Fig. 5.4a, showing $\{110\}$ and $\{111\}$ as the largest facets, as according to Goldschmidt.¹⁹

$\{111\}$ facets have been shown to frequently occur on rutile nanoparticles, especially wires.^{4,21–24} However, density functional theory calculations show that these facets possess a high surface energy, leading to other facets like $\{101\}$ or $\{221\}$ being present at the tips.^{25–29} In all such cases, rutile nanowires present a pointed tip. In addition, a (001) facet blunting the wire tip, as shown in Fig. 5.4b, has previously been observed.²² This facet is present in HRTEM micrographs of single fingers (Fig. 5.4c). It is challenging to predict which facets form during hydrothermal growth due to the system being very far from equilibrium. Among $\{101\}$, $\{001\}$ and $\{111\}$ facets, the $\{111\}$ facet is most likely to facilitate wire growth because it has the highest surface energy ($E_{101} \approx 0.98\text{ J/m}^2$ vs. $E_{001} \approx 1.15\text{ J/m}^2$ vs. $E_{111} \approx 1.33\text{ J/m}^2$).²⁹ The $\{110\}$ facets bound the nanowire sides because they have a much lower surface energy ($E_{110} \approx 0.42\text{ J/m}^2$), and therefore grow very slowly.

Fig. 5.5 gives a scheme of the proposed growth steps. Initially, the (111) facet is terminated by $\text{TiO}(\text{OH})_2$. In the first step, a new layer starts to grow from the outside edges of the $\{111\}$ facets towards the center, depicted in Fig. 5.5a. Because these edges are convex, they present the lowest steric hindrance from adjacent dangling OH^- groups.

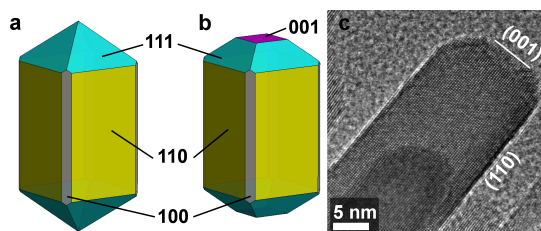


Figure 5.4: a) Crystal shape of macroscopic rutile.¹⁹ b) Assumed crystal shape during growth showing a small (001) facet. c) Visible flatness of a finger tip possessing a (001) facet. a)+b): Qualitative depiction generated using Wulffmaker.²⁰



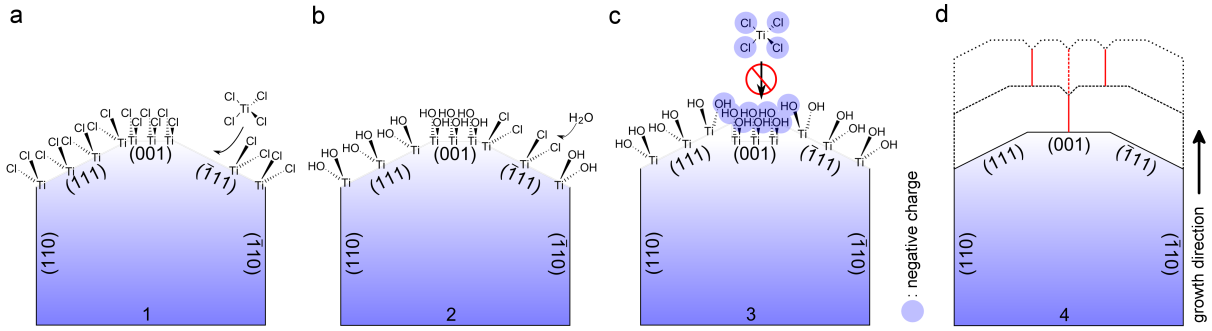
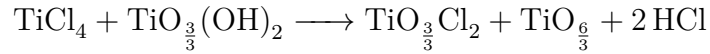
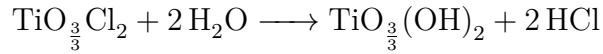


Figure 5.5: Schematic drawing of the hydrothermal growth process of TiO₂ rutile nanowires and the related formation of a defect cascade, involving the bonding of TiCl₄ to the {111} facets (a), exchange of the dangling Cl⁻ for OH⁻ (b), excessive steric hindrance in conjunction with a negative potential on the (001) facet repelling the TiCl₄ molecules (c), and the subsequent formation of defects (d).

Therefore, they are the most likely place for nucleation of a new layer, consistent with previous observations involving other techniques of crystal growth.^{30–32} A TiCl₄ releases two Cl⁻ ions into the solution and attaches to the {111} crystal surface, leaving two dangling Cl⁻ ions on the Ti:



The notation of $\frac{3}{3}$ at the oxygen emphasizes that the Ti at the (111) surface is bonded to the bulk crystal. While this continues across the nanowire tip, the dangling Cl⁻ ions are substituted for OH⁻ groups. This is the reaction associated with Fig. 5.5b:



A detailed schematic of the reactions for steps 1 and 2 is shown in Fig. 5.6. The same reactions must also take place on the small (001) facet at the top of the wire for overall growth (Fig. 5.5c). However, the nucleation barrier is expected to be much higher on this facet. This is because the surface density of oxygen atoms on the (001) facet is about twice as high as that of the (111) facet ($\delta_{001}(\text{O}) \approx 9.5 \text{ atoms/nm}^2$ vs. $\delta_{111}(\text{O}) \approx 4.3 \text{ atoms/nm}^2$, calculated assuming no surface reconstruction). Because the Ti⁴⁺ of the TiCl₄ is tetrahedrally surrounded by negatively-charged Cl⁻ ions, strong steric hindrance must be overcome for bonding to the nanowire. The new (111) layer would obstruct access to the (001)/(111) edge and further increase the nucleation barrier. Given the statistical nature of nucleation, one of two things is expected: either Case A, the {111} facets will at some point outpace the (001) facet by one or more atomic layers, or Case B layer growth over the (001) is nucleated by the {111} facet layers continuing into the (001) interior. In Case A, the {111} facets will terminate with {110} facets where they meet the (001) facet out of geometric necessity. The absence of convex corners means that nucleation must occur in the facet interior, which is very unlikely due to steric hindrance, particularly given the already high surface density of dangling oxygen atoms. Therefore,

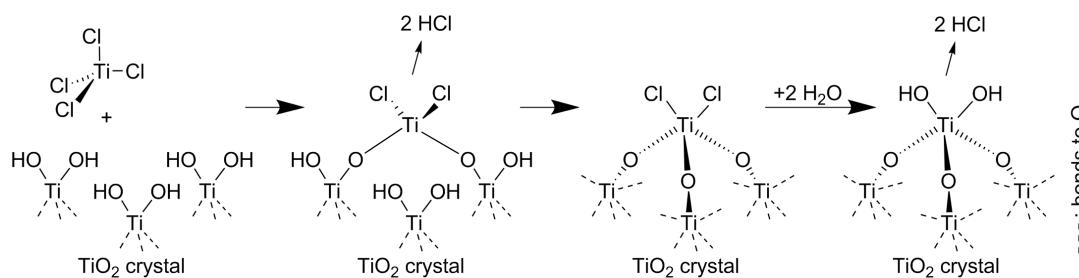


Figure 5.6: Scheme of the chemical transformation which leads to layered growth of TiO_2 .

growth is extremely slow or even stops on the (001) facet, while the surrounding $\{111\}$ facets continue to grow quickly. The $\{110\}$ facets surrounding the lagging (001) also grow slowly, but because the (001) is very small, just a few atomic layers can fill the cavity. In Case B, the layer on the (001) facet grows from the outsides in, as each of the four $\{111\}$ facets can contribute to covering the (001). Where the growing layers meet, there is one final row or cluster of unreacted sites with dangling OH^- that must react with TiCl_4 . However, the steric hindrance is extreme because the large TiCl_4 ion must overcome repulsion from a high density of OH^- groups on all sides of the reaction site. It is possible that the next atomic layer is added before this hole is filled, and access to the reaction site is permanently lost. Regardless of whether Case A or Case B occurs, the result is the same: a small void near the center of the nanowire. As subsequent growth occurs, the defect process is repeated wherever a (001) facet is present, resulting in a cascade of defects during continued wire growth (see Fig. 5.5d). A supporting scheme of possible defect configurations can be found in supplemental Figure 3. The principles of the model would not be altered if growth occurred on the $\{101\}$ facets instead of $\{111\}$ (as proposed by Li et al.,¹⁸ surface oxygen density $\delta_{101}(\text{O}) \approx 2.3 \text{ atoms}/\text{nm}^2$). The rising average width of the wires at higher reactant concentrations and synthesis times (Fig. 5.1b, c) indicates a slow simultaneous growth on the $\{110\}$ facets, which have a surface oxygen density similar to the (001) facet ($\delta_{110}(\text{O}) \approx 10.4 \text{ atoms}/\text{nm}^2$). While this increases the volume of the wire, it does not have an influence on the defect structure.

Under all synthesis conditions, the wires reached a particular length, and stopped growing. In all observed wires at their maximum length, the defect cascade reached the full width of the wire at the tip. It is possible that Ti reactant depletion causes cessation of growth, but it seems likely that the defects limit the total length of the wire. The fingers do grow with the bulk wire up to this point, so it is unclear what mechanism limits their growth beyond the point at which the wire tip is exclusively composed of fingers. If the defect cascade does set the maximum wire length, then modification or prevention of these defects will be essential for applications requiring high aspect-ratio wires.

A different growth mechanism for rutile nanowires in solvothermal environment has been proposed before by Li et al., although it was primarily developed to explain branching.¹⁸ Branching occurs when higher precursor concentrations are used. Single-directional nanowire growth can be explained to a certain extent by this model: First, an anatase



nanoparticle is formed in solution and subsequently transformed to rutile. Small anatase crystals can attach to the rutile due to a compatibility of the anatase $\{103\}$ and the rutile $\{101\}$ surfaces. After that, the anatase is transformed into rutile locally, and consequently integrated into the wire. Assuming that the small attached crystals have the same diameter as the individual finger structures, mechanisms which hinder their merging could be conceived as reason for the defect structure. However, this theory has some drawbacks for explaining finger formation: First, as stated in the work by Li et al., the two different possibilities of attachment of the anatase nanoparticles give rise to branching. Given a 50% chance of orientation mismatch, branches should be common in all solvothermally grown rutile nanowires, but they are not observed in many samples.^{9,11,15-17} Furthermore, the defect structure studied here is generally visible in hydrothermally-grown rutile wires, although in the majority of cases it is not commented upon.^{9,14,15,17,21}

Rutile nanowires synthesized with a larger electronegative group contain a much higher defect density, further supporting our model. The results of another synthesis route, where no HCl is present, can be found in supplemental Figure 4. When HCl is replaced by HNO₃, the results are cauliflower-like nodules with a fibrous internal structure. The addition of a small amount of NaCl during synthesis results in distinguishable nanowires, although they contain a high density of defects. The growth of these structures is due to the transformation of Ti(OBu)₄ into Ti(NO₃)₄ instead of TiCl₄. Adding NaCl probably does not result in the formation of TiCl₄ but an enrichment of Cl⁻ ions on the $\{110\}$ surfaces, enabling the growth of elongated nanowires, as has been stated in other studies.^{11,28,33} The overall increase in defects can be explained by the size difference between NO₃⁻ and Cl⁻ ions, since larger molecules on the (001) facet as well as the larger Ti(NO₃)₄ complex (Fig. 5.5, step 3) should dramatically increase the defect density by the mechanism proposed in this work.

Conclusion

We developed a growth model for TiO₂ rutile nanowires under hydrothermal conditions. For this purpose, rutile nanowire arrays were synthesized on FTO glass substrates with varying reactant concentrations and reaction times. TEM investigation revealed V-shaped defect cascades which initiate near the bottom of the wires and terminate in finger-like subwires at the tips. Observations of the wires in cross-section confirm that the predominant orientation of defects is along $\langle 110 \rangle$ directions, forming fingers with a rectangular base and diagonal widths averaging 7 nm. Edge dislocations were found that accommodate extra volume in the crystal necessitated by the defects. Layer-by-layer growth on the $\{111\}$ facets expedites the growth along the [001] axis. Steric hindrance from terminating OH⁻ groups together with coulombic repulsion account for the initiation of the defects on the (001) plane. Increasing the size of the ions involved in the growth process significantly increases the defect density, further supporting the model.

A natural extension of this work would be efforts to determine the influence of these

defects on performance in applications, such as photovoltaic cells. Modification or elimination of these defects could dramatically improve the suitability of rutile nanowires for semiconductor devices, and allow for longer or higher aspect-ratio wires.

Supporting Information

Table 5.1: Hydrothermal synthesis conditions of the samples

Sample name	Temperature	Duration	Ti(OBu) ₄	NaCl
A	150 °C	3 h	58 mmol/L	0.25 mol/L
B	150 °C	20 h	58 mmol/L	0.00 mol/L
C	150 °C	3 h	58 mmol/L	0.06 mol/L

$V_{\text{H}_2\text{O}} = V_{\text{HCl}} = 5 \text{ mL}$

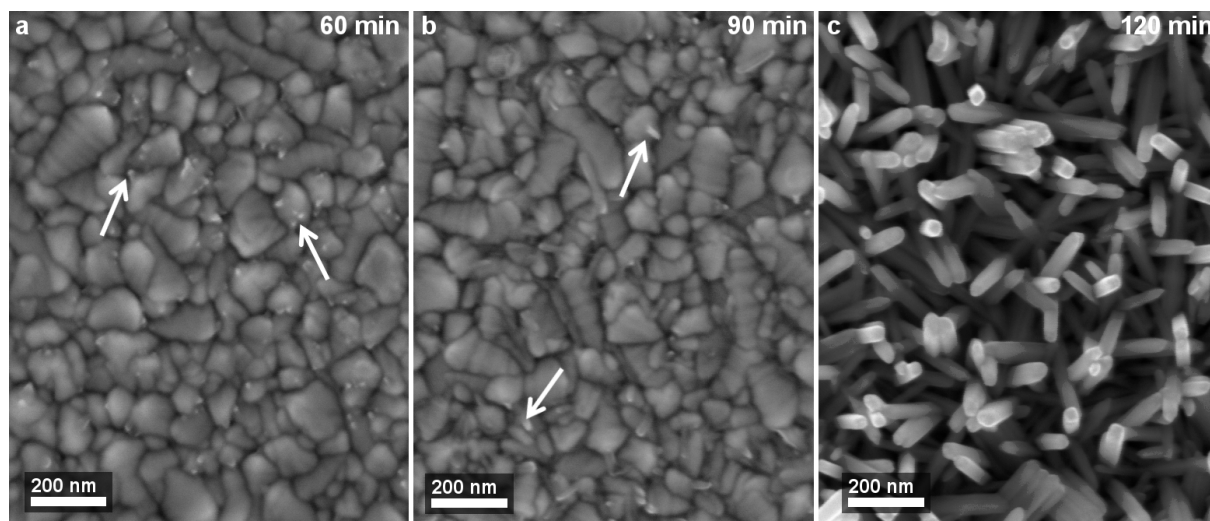


Figure 5.7: SEM images of the crystals at the start of the nanowire growth. a) After 60 minutes at 150 °C, the first crystallites can be seen on the FTO substrate. b) During the following 30 minutes, small nanowires start to develop. c) After 120 minutes, the FTO is covered by standing nanowires with an average width of 32 nm.



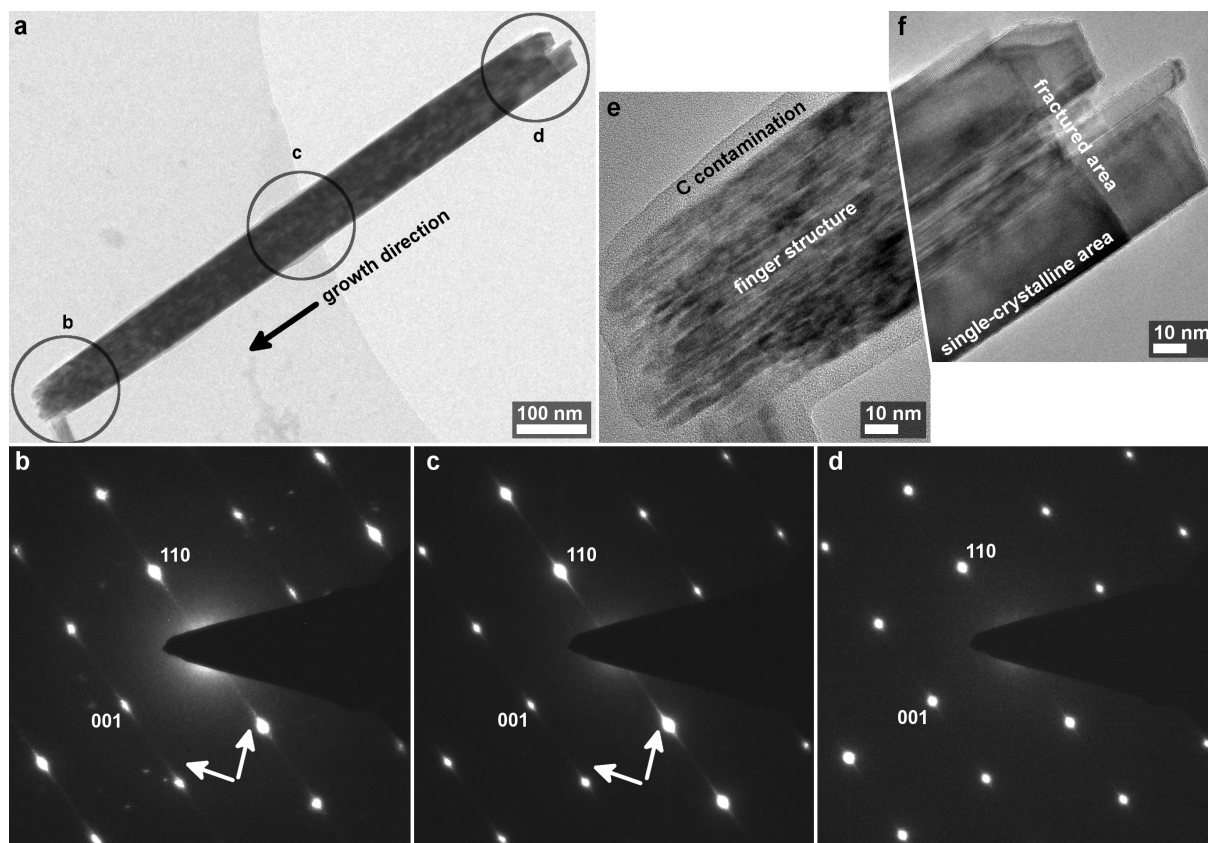


Figure 5.8: Single nanowire and corresponding diffraction patterns (left to right): a) BF image of a typical rutile nanowire. b-d) ED patterns as marked in a). The streaks caused by the finger structures are indicated by arrows in b) (top of the wire) and c) (middle of the wire), and are largely diminished in d) (near bottom of the wire). e) and f) show higher magnifications of e) the wire tip, prominently including the finger structure and f) the wire bottom at its fractured area, showing a wide single-crystalline area surrounding the first fingers in the center of the wire.

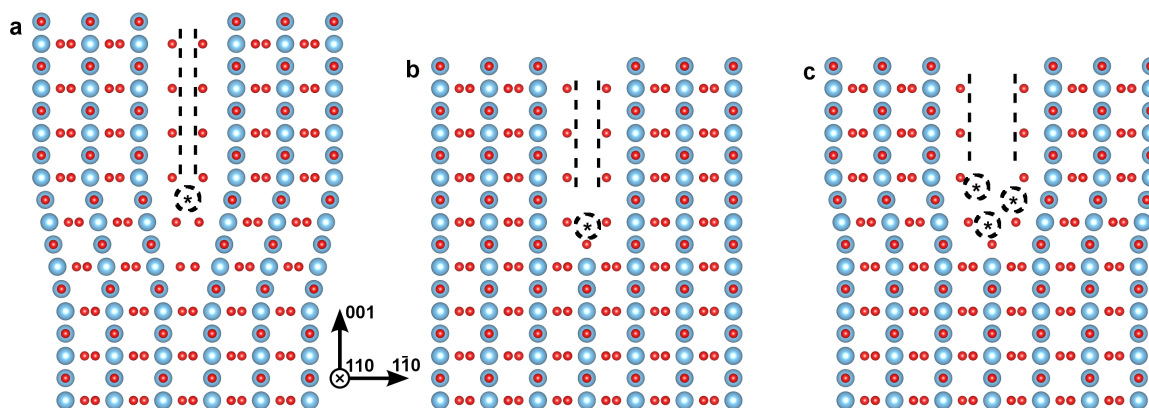


Figure 5.9: a), b) and c) show possible projected atomic configurations at the origin of the finger structure. Blue spheres represent Ti ions, red spheres represent O ions. The black dashed lines indicate the free internal surfaces. An asterisk indicates possible positions of growth-constricting ions. N.B., these schematics are presented only to benefit the readers' understanding of the proposed defect structure. The respective atomic configuration might be far more disarranged than proposed here, specifically at the free internal surfaces. For a more accurate understanding of the atomic configuration, DFT calculations would be needed. Additionally, one could imagine a variety of modifications at the free internal surfaces, including oxygen vacancies, double-bonded oxygen, residues like OH^- groups and Cl^- , etc.

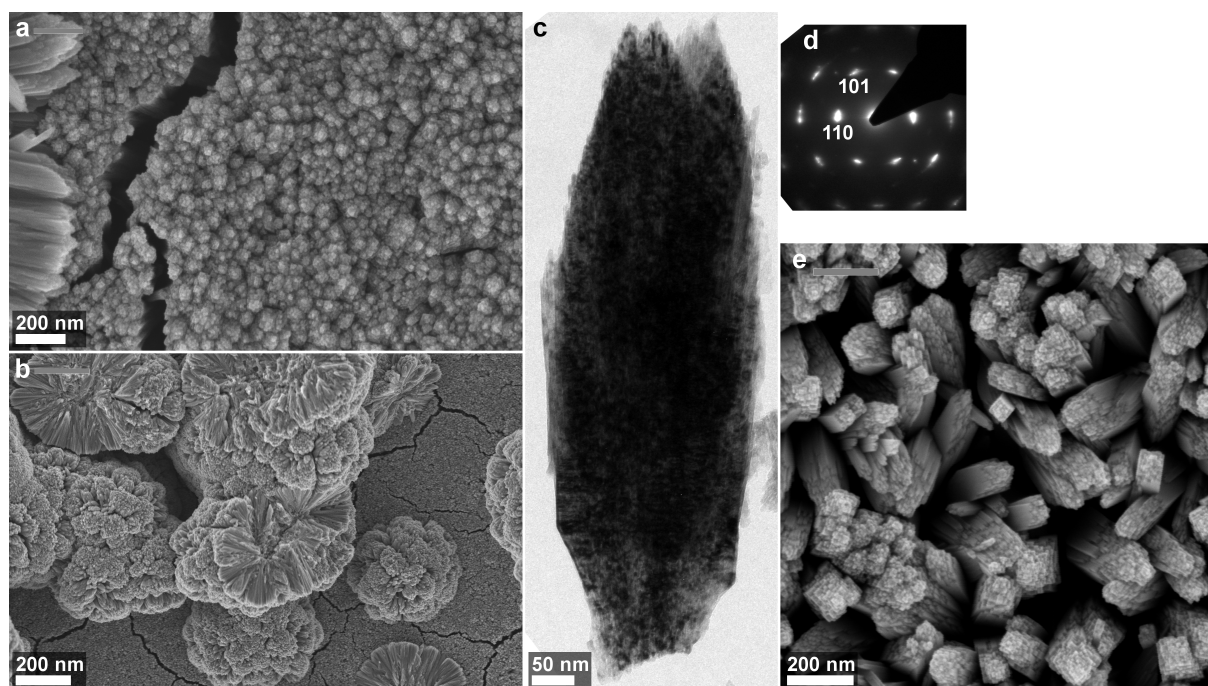


Figure 5.10: Morphology of the nanostructures obtained from an HNO_3 -based synthesis. a,b) SEM top view shows a compact layer and larger, flower-like spherical structures. c) TEM BF image of a wire stemming from the sample shown in a). The diameter of the nodule seems to be defined by the packing of the wires. A speckled contrast hints towards a multitude of defects. d) The ED pattern from the nodule in c) shows that the optical axis is $[11\bar{1}]$ and the crystal phase is rutile. e) SEM top view of the structures obtained from the HNO_3 -based synthesis with 0.3 mol/L NaCl. The single rutile nanowires are distinguishable.

Bibliography

- [1] Z. Zhao, Z. Sun, H. Zhao, M. Zheng, P. Du, J. Zhao, and H. Fan, "Phase control of hierarchically structured mesoporous anatase TiO_2 microspheres covered with $\{001\}$ facets," *Journal of Materials Chemistry*, vol. 22, pp. 21965–21971, 2012.
- [2] X. Xiao, X. Liu, H. Zhao, D. Chen, F. Liu, J. Xiang, Z. Hu, and Y. Li, "Facile shape control of Co_3O_4 and the effect of the crystal plane on electrochemical performance," *Advanced Materials*, vol. 24, no. 42, pp. 5762–5766, 2012.
- [3] G. Zou, H. Li, Y. Zhang, K. Xiong, and Y. Qian, "Solvothermal/hydrothermal route to semiconductor nanowires," *Nanotechnology*, vol. 17, no. 11, p. 313, 2006.
- [4] X. Huang and C. Pan, "Large-scale synthesis of single-crystalline rutile TiO_2 nanorods via a one-step solution route," *Journal of Crystal Growth*, vol. 306, no. 1, pp. 117 – 122, 2007.
- [5] B. Liu and H. C. Zeng, "Hydrothermal synthesis of ZnO nanorods in the diameter regime of 50 nm," *Journal of the American Chemical Society*, vol. 125, no. 15, pp. 4430–4431, 2003.
- [6] X. Xia, J. Tu, Y. Zhang, X. Wang, C. Gu, X.-b. Zhao, and H. J. Fan, "High-quality metal oxide core/shell nanowire arrays on conductive substrates for electrochemical energy storage," *ACS Nano*, vol. 6, no. 6, pp. 5531–5538, 2012.
- [7] G. Shen, P.-C. Chen, K. Ryu, and C. Zhou, "Devices and chemical sensing applications of metal oxide nanowires," *Journal of Materials Chemistry*, vol. 19, pp. 828–839, 2009.
- [8] K. Shankar, J. I. Basham, N. K. Allam, O. K. Varghese, G. K. Mor, X. Feng, M. Paulose, J. A. Seabold, K.-S. Choi, and C. A. Grimes, "Recent advances in the use of TiO_2 nanotube and nanowire arrays for oxidative photoelectrochemistry," *Journal of Physical Chemistry C*, vol. 113, no. 16, pp. 6327–6359, 2009.
- [9] Q. Zhou, S. Zhang, X. Yang, Q. Wu, H. Zhao, and M. Wu, "Rutile nanowire array electrodes for photoelectrochemical determination of organic compounds," *Sensors and Actuators B*, vol. 186, pp. 132 – 139, 2013.



- [10] J. Guo and J. Liu, "Topotactic conversion-derived $\text{Li}_4\text{Ti}_5\text{O}_{12}$ -rutile TiO_2 hybrid nanowire array for high-performance lithium ion full cells," *RSC Advances*, vol. 4, pp. 12950–12957, 2014.
- [11] X. Feng, K. Shankar, O. K. Varghese, M. Paulose, T. J. Latempa, and C. A. Grimes, "Vertically aligned single crystal TiO_2 nanowire arrays grown directly on transparent conducting oxide coated glass: Synthesis details and applications," *Nano Letters*, vol. 8, no. 11, pp. 3781–3786, 2008.
- [12] A. Kumar, A. R. Madaria, and C. Zhou, "Growth of aligned single-crystalline rutile TiO_2 nanowires on arbitrary substrates and their application in dye-sensitized solar cells," *Journal of Physical Chemistry C*, vol. 114, no. 17, pp. 7787–7792, 2010.
- [13] J. A. Dorman, J. Weickert, J. B. Reindl, M. Putnik, A. Wisnet, M. Noebels, C. Scheu, and L. Schmidt-Mende, "Control of recombination pathways in TiO_2 nanowire hybrid solar cells using Sn^{4+} dopants," *The Journal of Physical Chemistry C*, vol. 118, no. 30, pp. 16672–16679, 2014.
- [14] E. Hosono, S. Fujihara, K. Kakiuchi, and H. Imai, "Growth of submicrometer-scale rectangular parallelepiped rutile TiO_2 films in aqueous TiCl_3 solutions under hydrothermal conditions," *Journal of the American Chemical Society*, vol. 126, no. 25, pp. 7790–7791, 2004.
- [15] B. Liu and E. S. Aydil, "Growth of oriented single-crystalline rutile TiO_2 nanorods on transparent conducting substrates for dye-sensitized solar cells," *Journal of the American Chemical Society*, vol. 131, no. 11, pp. 3985–3990, 2009.
- [16] E. Enache-Pommer, B. Liu, and E. S. Aydil, "Electron transport and recombination in dye-sensitized solar cells made from single-crystal rutile TiO_2 nanowires," *Physical Chemistry Chemical Physics*, vol. 11, pp. 9648–9652, 2009.
- [17] Y. Zhao, X. Gu, and Y. Qiang, "Influence of growth time and annealing on rutile TiO_2 single-crystal nanorod arrays synthesized by hydrothermal method in dye-sensitized solar cells," *Thin Solid Films*, vol. 520, no. 7, pp. 2814 – 2818, 2012.
- [18] D. Li, F. Soberanis, J. Fu, W. Hou, J. Wu, and D. Kisailus, "Growth mechanism of highly branched titanium dioxide nanowires via oriented attachment," *Crystal Growth & Design*, vol. 13, no. 2, pp. 422–428, 2013.
- [19] V. Goldschmidt, *Atlas der Krystallformen, Band VII, Pyroaurit-Rutil*. Carl Winters Universitätsbuchhandlung, Heidelberg, 1913.
- [20] R. V. Zucker, D. Chatain, U. Dahmen, S. Hagège, and W. C. Carter, "New software tools for the calculation and display of isolated and attached interfacial-energy minimizing particle shapes," *Journal of Materials Science*, vol. 47, no. 24, pp. 8290–8302, 2012.
- [21] K. Kakiuchi, E. Hosono, H. Imai, T. Kimura, and S. Fujihara, "{111}-faceting of low-temperature processed rutile TiO_2 rods," *Journal of Crystal Growth*, vol. 293, no. 2, pp. 541 – 545, 2006.
- [22] C. B. Mendive, T. Bredow, A. Feldhoff, M. Blesa, and D. Bahnemann, "Adsorption of oxalate on rutile particles in aqueous solutions: a spectroscopic, electron-microscopic and theoretical study," *Physical Chemistry Chemical Physics*, vol. 10, pp. 1960–1974, 2008.
- [23] N. Murakami, A. Ono, M. Nakamura, T. Tsubota, and T. Ohno, "Development of a visible-light-responsive rutile rod by site-selective modification of iron(III) ion on {111} exposed crystal faces," *Applied Catalysis B*, vol. 97, pp. 115 – 119, 2010.
- [24] L. Sun, Y. Qin, Q. Cao, B. Hu, Z. Huang, L. Ye, and X. Tang, "Novel photocatalytic antibacterial activity of TiO_2 microspheres exposing 100% reactive {111} facets," *Chemical Communications*, vol. 47, pp. 12628–12630, 2011.
- [25] M. Ramamoorthy, D. Vanderbilt, and R. D. King-Smith, "First-principles calculations of the energetics of stoichiometric TiO_2 surfaces," *Physical Review B*, vol. 49, pp. 16721–16727, 1994.
- [26] P. M. Oliver, G. W. Watson, E. Toby Kelsey, and S. C. Parker, "Atomistic simulation of the surface structure of the TiO_2 polymorphs rutile and anatase," *Journal of Materials Chemistry*, vol. 7, pp. 563–568, 1997.
- [27] T. Ohno, K. Sarukawa, and M. Matsumura, "Crystal faces of rutile and anatase TiO_2 particles and their roles in photocatalytic reactions," *New Journal of Chemistry*, vol. 26, pp. 1167–1170, 2002.
- [28] A. S. Barnard and L. A. Curtiss, "Prediction of TiO_2 nanoparticle phase and shape transitions controlled by surface chemistry," *Nano Letters*, vol. 5, no. 7, pp. 1261–1266, 2005.

- [29] T. P. Hardcastle, R. M. D. Brydson, K. J. T. Livi, C. R. Seabourne, and A. J. Scott, “Ab-initio modelling, polarity and energetics of clean rutile surfaces in vacuum and comparison with water environment,” *Journal of Physics: Conference Series*, vol. 371, no. 1, p. 012059, 2012.
- [30] S. H. Oh, M. F. Chisholm, Y. Kauffmann, W. D. Kaplan, W. Luo, M. Rühle, and C. Scheu, “Oscillatory mass transport in vapor-liquid-solid growth of sapphire nanowires,” *Science*, vol. 330, no. 6003, pp. 489–493, 2010.
- [31] A. D. Gamalski, C. Ducati, and S. Hofmann, “Cyclic supersaturation and triple phase boundary dynamics in germanium nanowire growth,” *Journal of Physical Chemistry C*, vol. 115, no. 11, pp. 4413–4417, 2011.
- [32] C.-Y. Wen, J. Tersoff, K. Hillerich, M. C. Reuter, J. H. Park, S. Kodambaka, E. A. Stach, and F. M. Ross, “Periodically changing morphology of the growth interface in Si, Ge, and GaP nanowires,” *Physical Review Letters*, vol. 107, p. 025503, 2011.
- [33] H. Cheng, J. Ma, Z. Zhao, and L. Qi, “Hydrothermal preparation of uniform nanosize rutile and anatase particles,” *Chemistry of Materials*, vol. 7, no. 4, pp. 663–671, 1995.



Chapter 6

Defeating Loss Mechanisms in 1D TiO₂-Based Hybrid Solar Cells

This chapter has been submitted as follows:

A. Wisnet, K. Bader, S. B. Betzler, M. Handloser, J. Weickert, A. Hartschuh L. Schmidt-Mende, C. Scheu and J. A. Dorman; submitted to *Advanced Functional Materials*

Introduction

Owing to their chemical stability, availability, and intrinsic semiconducting properties, titanium dioxide (TiO₂) nanostructures have extensively been studied for application in next generation technologies such as solar cells, Li-ion battery electrodes, photocatalysts, and memristors.¹⁻⁵ Commonly, 25 nm particle TiO₂ films are annealed, forming a high surface-area mesoporous scaffolding, ideal for applications in hybrid, dye-sensitized (DSSC), and perovskite solar cells with devices reaching conversion efficiencies of 3.2, 12.3, and 19.3 %, respectively.⁶⁻⁹ Previously, in an attempt to improve the metal-oxide material, groups have substituted the mesoporous film with nanostructured ones. Here, the TiO₂ exists for example as 3D single crystal by using a template method,¹⁰ or as 1D wires when using a hydrothermal method for a natural bottom-up approach.¹¹⁻¹⁴ While both of these approaches have successfully been implemented into perovskite and solid state (ss)-DSSCs, the improvement was not as drastic as expected. For example, an efficiency improvement of 10 % was achieved for the electrochemical ss-DSSC gyroid structure (from 2.67 % to 2.97 %).^{10,15} Alternatively, a semi-ordered array of rutile nanowires is formed via a hydrothermal growth process directly on a fluorine-doped tin oxide (FTO) substrate. This process allows the separate tuning of wire diameters between 70 and 200 nm and wire lengths up to 10 μm. These nanowires are said to be single-crystalline rutile due to the growth processing, producing a high-mobility electron transporter, roughly 1 cm² V⁻¹ s⁻¹, without the obstacle of multiple grain boundaries during charge transport which is present in the mesoporous films.¹⁶ Additionally, the nanostructured arrays allow for direct transport to the electrode, as opposed to mesoporous diffusive transport. While

the hydrothermal nanowires start to grow in a single-crystalline manner, distinct defects and internal surfaces have been reported to appear axially throughout the length of the crystal in what has been called a finger-like structure.¹⁴ The fingers are believed to form due to Coulombic and steric hindrance at the (001) surface present during growth, prohibiting the titanium precursor from reacting and condensing in a uniform single crystal. The structure can be termed a quasi-single crystal, since the fingers merge together in a defect-free structure near the nucleation point. One measure which has been previously discussed, albeit for an alternate reason, is a high-temperature (HT) post annealing at 500 °C.¹⁷ It was initially concluded that the annealing increased the contact with the FTO substrate while passivating the surface recombination sites at the interface. These effects can also be achieved using an additional TiCl₄ treatment and subsequent annealing at 450 °C, which is commonly used for mesoporous films with the additional benefit of increased dye absorption.¹⁸ It is necessary to understand the role of defects in general, and the finger-like structures in particular, with regard to loss mechanisms and electrical performance in TiO₂ devices, where electron transport is vital. Photovoltaic devices are a suitable model system to extract the photophysical and electronic properties of such TiO₂ electrodes.

In this work, the relationship of annealing and chemical treatment, crystal defect structure and charge transport in the nanowires is probed in order to develop strategies to enhance the electrical conductivity of the electrode. With this approach the band structure and defect density near the metal oxide-polymer interface is engineered, allowing for direct control of the charge density and mobility. HT annealing makes it possible to eliminate the fingers, simultaneously reducing recombination sites, and thus canceling a number of loss mechanisms. A combination of electrical, optical and structural characterization techniques is used to investigate the role of the finger structures and crystal defects in general, and a model is developed to describe the carrier transport in hybrid and DSSC type solar devices. Scanning- (SEM) and transmission electron microscopy (TEM) give insight into morphology and crystal characteristics. Charge recombination is discussed using time-resolved photoluminescence (PL), transient photovoltage (TPV), and impedance spectroscopy (IS), all of which indicate a reduction of radiative trap state-assisted recombination typical for these structures, favoring non-radiative and/or long-living recombination mechanisms after annealing at elevated temperatures. Additionally, a noticeable improvement is seen when comparing these hybrid nanowire devices to their mesoporous counterparts, as reported in literature, with similar material combination. It is expected that these results can be extended to Li batteries and photocatalysts, where rapid transport of charges through a trap-free energy landscape is necessary for improved device performance. In general, our findings indicate that the crystal quality of metal oxides ought to be carefully examined to counter detrimental effects.



Results and Discussion

Nanowire arrays with nanowire dimensions of approximately 80-100 nm in diameter and 1 μm in length were grown using the hydrothermal method reported previously.¹³ A TiCl_4 treatment was conducted in order to mitigate surface defects and to increase the total surface area by roughening of the surface layer. After an initially single-crystalline growth, the wires tend to form a finger structure featuring free internal surfaces parallel to the wire during growth due to a combination of steric and Coulombic repulsion at the (001) growth layer, as recently discussed.¹⁴ In order to remove these finger structures, the annealing temperature of some samples was increased from 450 $^\circ\text{C}$ to 600 $^\circ\text{C}$ at two distinct times during the sample fabrication process: before (Sample 600/450) and after (Sample 450/600) the TiCl_4 treatment. These two annealing points were chosen in order to distinguish the role of annealing on the wire structure from that of the shell structure which requires an annealing step. A reference sample was annealed two times at 450 $^\circ\text{C}$ (Sample 450/450). A detailed description of the synthesis procedure can be found in the Supporting Information. High-resolution SEM images of the nanowire arrays are shown in Figure 6.1 a)-c), highlighting the change in surface structure with annealing processes (low-magnification top views in Figure 6.6). A rough, dense layer is observed in the case of Samples 450/450 (a)) and 600/450 (b)), resulting in a high surface area where dye adsorption and charge separation can occur. When the HT annealing occurs after the TiCl_4 treatment for Sample 450/600 (c)), the surface roughness appears to decrease with only small bumps located across the wires. For all cases, the annealing does not fully remove the truncated finger structure at the tip of each wire. No distinct difference was seen in X-ray diffraction (XRD) spectra after different annealing temperatures since the nanowires naturally form a rutile crystal structure and the volume of the shell layer is below the sensitivity of the measurement (shell thickness < 2 nm) (Figure 6.7). Figure 6.1 d)-f) shows detailed high-resolution TEM (HRTEM) micrographs of the respective samples (bright-field images of the wires are shown in Figure 6.8). The particles attached to the wire surfaces usually have a thickness of about 5 nm. Particles found in Samples 450/450 (d)) and 600/450 (e)) can be attributed to anatase ($\{101\}$ anatase lattice planes marked by an asterisk), while Sample 450/600 (f)) features rutile particles which are epitaxially bonded to the wire. This coincides with the observations made in Figure 6.1 c) and suggests that the TiCl_4 treatment forms a polycrystalline anatase layer after annealing at 450 $^\circ\text{C}$, but transforms to rutile during the 600 $^\circ\text{C}$ annealing. The atomic arrangement of the wire core acts as a seed layer for the epitaxial rearrangement of the shell layer. Scanning TEM (STEM) images of the three samples are presented in Figure 6.1 g)-i). The contrast in Sample 450/450 (g)) shows stripes running along the length of the wire, indicating a finger structure in the hydrothermally-grown core throughout the length of the wire.¹⁴ Compared to this, Samples 600/450 (h)) and 450/600 (i)) show homogeneous single-crystalline areas at the edge of the wires, while their cores feature a number of voids. These features are a result of the annealing steps at 600 $^\circ\text{C}$ which allows for dif-

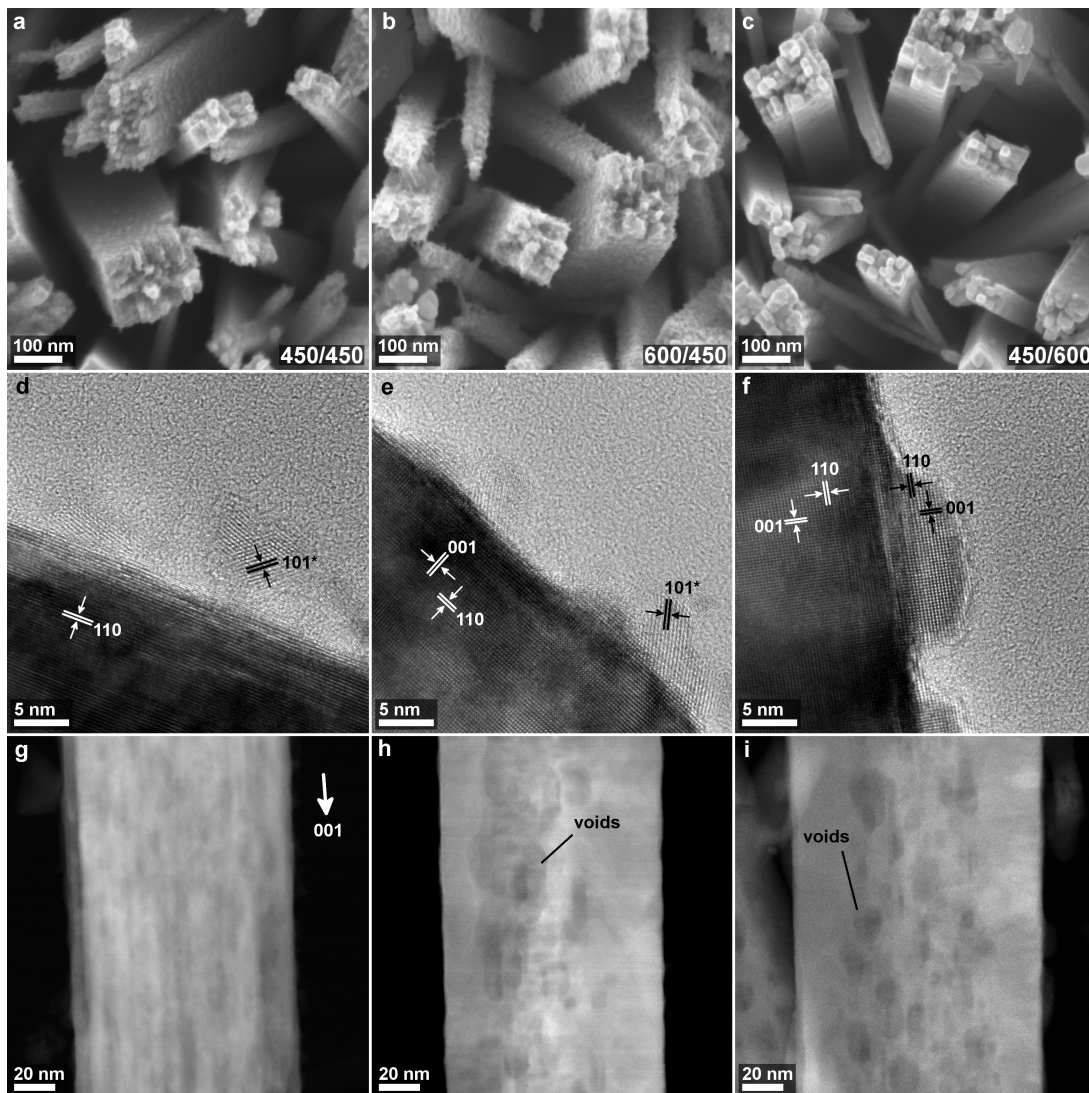
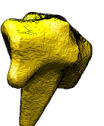


Figure 6.1: High magnification SEM images of a) Sample 450/450, b) Sample 600/450, and c) Sample 450/600 show the surface roughness and external finger structure after the annealing treatment. d)-f) HRTEM micrographs show the rutile modification for the wires. Particles featuring the anatase crystal structure are found for Samples 450/450 and 600/450 (d), e), indices marked by an asterisk). Sample 450/600 shows rutile particles which attached epitaxially during annealing of the wire. g)-i) STEM images of the respective wires show that annealing at 450 °C does not considerably change the finger structure, which can be identified by brighter lines along the nanowires in g). Annealing at 600 °C results in homogeneous single crystalline areas at the outer edges of the wires, while voids are formed inside the wires (h, i).

fusion processes as discussed on the basis of Figures 6.9 and Figure 6.10. The volume previously enclosed by the free internal surfaces (the finger structure) is accumulated as voids roughly resembling the Wulff shape of rutile.

PL spectra of bundles of nanowires from the three different samples were taken after femtosecond-pulsed excitation at 800 nm. The investigated material volume was kept larger than the excitation volume (pump flux was kept constant) for each sample during the measurement to allow for comparing the resulting PL intensities. For TiO₂ the PL emission is mainly generated by emissive trap states at the surface of the material, as described before, and is strongly influenced by different fabrication methods or anneal-



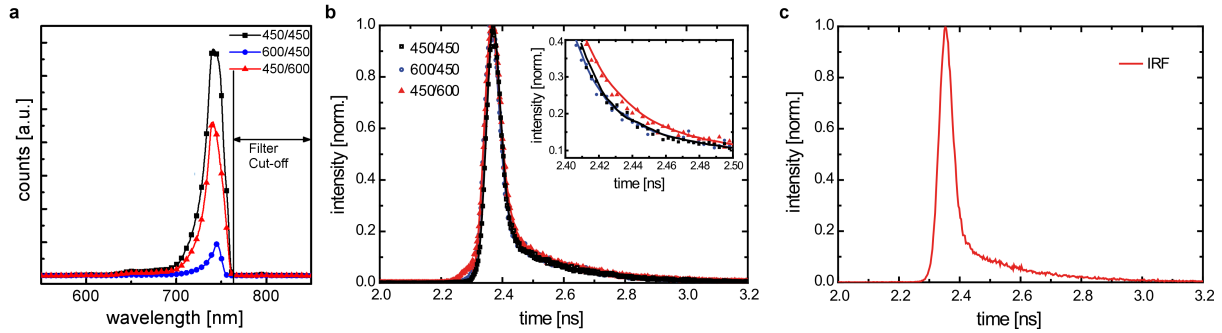


Figure 6.2: a) PL spectra after two-photon excitation at 1.55 eV. Sample 450/450 exhibits the highest signal intensity. Direct quenching of the PL emission after annealing is stronger for Sample 600/450 than for Sample 450/600, indicating a fast non-radiative recombination channel in the former. b) TCSPC characteristics are measured after a short excitation pulse. The inset shows the detailed area of interest. Resulting lifetimes are listed in Table 6.1. c) Instrument response function for b). A FWHM of ≈ 20 ps in combination with the ultrashort excitation pulse of 150 fs allows for a time resolution of 3 ps.²² Additional experimental details can be found in the supporting information.

ing treatments.^{19–21} In Figure 6.2 a) the PL spectra after two photon excitation of the different sample types are shown. They are spatially averaged to minimize the influence of heterogeneities. The spectral position is roughly centered around 820 nm reflecting the value reported in literature.¹⁹ Sample 450/450 features the highest PL intensity and thus quantum yield, assuming constant absorption cross sections for all samples. Sample 450/600 still exhibits a considerably stronger signal than Sample 600/450. The intensity data was complemented with PL lifetime measurements using time-correlated single photon counting (TCSPC) with a time resolution of about 3 ps to distinguish radiative and non-radiative decay rates (Figure 6.2 b)).²² This technique is independent of the investigated material volume. For Sample 450/450, an intensity averaged lifetime of about 10 ps was observed pointing towards a fast radiative decay at emissive trap states, which gives a high intensity due to the large number thereof. Sample 600/450 features a similar lifetime of 9 ps, but connected to a much lower PL intensity. This indicates faster non-radiative recombination, suppressing the radiative decay predominant in Sample 450/450, leading to a lower quantum yield and thus weaker PL.

The faster non-radiative decay could result from a reduced trap density and the anatase shell layer introducing a band bending that facilitates charge separation, preventing radiative recombination but opening a non-radiative channel at the interface.²³ Sample 450/600 features neither an internal defect structure, nor the external anatase-rutile interface. This is prominently demonstrated by a substantially longer PL lifetime of 21 ps. However, the electron-hole pairs can possibly also recombine in the "bulk" of the nanowires at slower rates, displaying an additional radiative recombination channel visible in the increased fraction of the slow component used in the fit-routine to obtain the presented intensity averaged lifetime values. This channel is probably suppressed in Sample 600/450 due to the fast, non-radiative decay. Hence, the interface between anatase shell layer and rutile wire facilitates the charge separation, while the absence of internal surfaces results in a substantial decrease of recombination sites within the charge-transporting

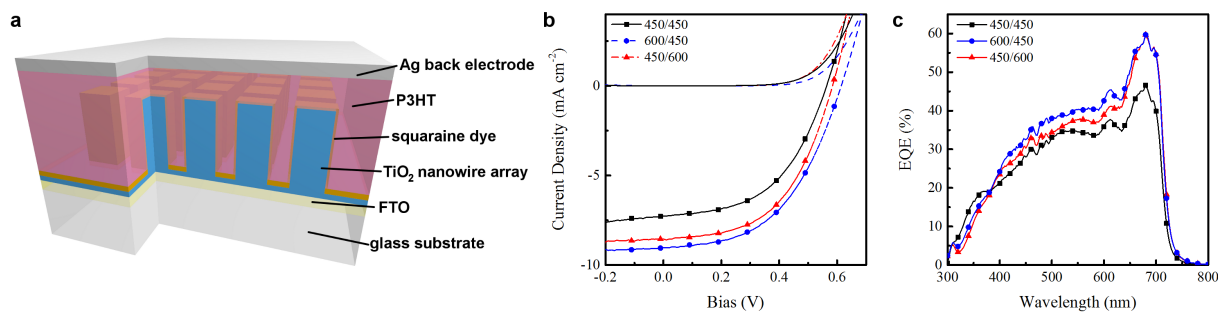


Figure 6.3: a) Schematic of the device structure. b) J-V curves for the three samples show increased J_{SC} and V_{OC} for the samples annealed at higher temperatures, with Sample 600/450 providing the highest PCE (see Table 6.1). c) EQE spectra for the respective samples.

wires, underlining the suitability of Sample 600/450 for solar-cell applications.

To demonstrate the influence of the finger structures on the performance of a photovoltaic device, inverted hybrid devices were fabricated using a squaraine dye (SQ2) as a light absorber and poly(3-hexylthiophene) (P3HT) as a hole transport layer (Figure 6.3 a)). This material combination was specifically chosen due to the alignment of the lowest unoccupied molecular orbital (LUMO) of SQ2 being between that of the P3HT and the conduction band of the TiO₂, allowing for charge extraction from both, SQ2 and P3HT.²⁴ Absorption spectra of SQ2 on the three different TiO₂ surfaces show a change in the aggregation of dye molecules depending on annealing treatment, leading to an enhanced absorption of higher energies in Sample 600/450 (Figure 6.11). J-V curves with and without illumination were measured for the three sample types, with the best performance for each device being plotted (Figure 6.3 b)). After annealing, the devices show a sound improvement in performance due to increases in both, the short-current density (J_{SC}) and open-circuit voltage (V_{OC}), as can be seen in Table 6.1. The experiments were repeated several times with all sample sets showing the same trend, indicating that the improvement is not due to individual deviations. Additional experimental results can be found in the supporting information for a second sample set (Figure 6.12).²⁵ Sample 450/450 exhibited a $J_{SC} = -7.27 \text{ mA cm}^{-2}$ and $V_{OC} = 0.57 \text{ V}$ ($\eta = 2.03 \%$). In contrast, Sample 600/450 produced a $J_{SC} = -9.02 \text{ mA cm}^{-2}$ and $V_{OC} = 0.61 \text{ V}$ ($\eta = 2.71 \%$) compared to that of Sample 450/600 at $J_{SC} = -8.54 \text{ mA cm}^{-2}$ and $V_{OC} = 0.59 \text{ V}$ ($\eta = 2.53 \%$). The efficiency of Sample 450/450 is comparable to those that are achieved for a semi-optimized mesoporous TiO₂(500nm)/SQ2/P3HT device with various pyridine surface modifiers for

Table 6.1: The key figures of merit including short circuit current density (J_{SC}), open circuit voltage (V_{OC}), fill factor (FF), conversion efficiency (η) are collected for the working devices. Additional values are included to highlight recombination, such as the quality factor (α), TPV recombination lifetimes (τ_{Rec}), and TiO₂ PL emission lifetimes (τ).

Sample	J_{SC} mA cm^{-2}	V_{OC} V	FF %	η %	α	$\tau_{Rec}(\text{PVD})$ μs	$\tau(\text{PL})$ ps
450/450	-7.27	0.564	51	2.03	0.936	88	10
600/450	-9.02	0.614	50	2.71	0.980	81	9
450/600	-8.26	0.585	53	2.53	0.976	106	21



increased surface interactions.^{24,26}

Charge generation was investigated by measuring the external quantum efficiency (EQE), shown in Figure 6.3 c). In comparison, Sample 450/450 shows reduced charge generation across the whole spectrum except a small region in the range of 350-380 nm. This feature can be attributed to the defects within the core which are removed during HT annealing in the other two samples, leading to a diminished charge generation within the TiO₂. The increase of charge generation within the dye is similarly enhanced for both of these two samples at its main peak at 670 nm, while the second peak related to the dye (at 615 nm) and the whole region related to absorption in P3HT exhibits the highest EQE for Sample 600/450. This suggests that the main SQ2 EQE feature is limited through light absorption after annealing and no longer through charge injection into the TiO₂, in contrast to the other regions of the spectrum. The different behavior between Samples 600/450 and 450/600 at the peak of 615 nm is probably related to the aggregation of the dye, as discussed on the basis of the absorption peak in Figure 6.11.

The charge transport within the devices was probed by intensity-dependent measurements, and lifetimes of the charges were extracted from transient photodecay measurements (full description in Figure 6.13). Fitting J_{SC} as a function of light intensity using the relationship $J_{SC} = \beta P_i^\alpha$ (P_i as incident light power, α and β power law coefficients) gives the quality factor α , serving as an indicator for trap state recombination.²⁷ Consequently, the respective values of $\alpha = 0.936$ for Sample 450/450, $\alpha = 0.980$ for Sample 600/450 and $\alpha = 0.976$ for Sample 450/600 correspond to a strongly reduced number of trap states in the latter two samples. Transient photovoltage decay (TPV) curves showed a decreasing carrier lifetime for increasing background illumination intensities. The related charge recombination lifetimes resulted in 88 μ s for Sample 450/450, 81 μ s for Sample 600/450 and 106 μ s for Sample 450/600 at standard illumination, reflecting the trend shown by the PL measurements. Finally, to probe the dynamics under various working conditions, and in particular around the maximum power point, IS measurements were conducted with and without illumination between 0 and 0.5 V bias. The measured impedance curves were simulated using the model shown in Figure 6.14. In this model, a series of parallel RC circuits represents the interface between TiO₂ and the organic along the nanowire side walls. An additional RC circuit is included in order to allow for successful data modeling, which is attributed to effects due to slightly non-Ohmic external contacts. The results of the fitting for the recombination

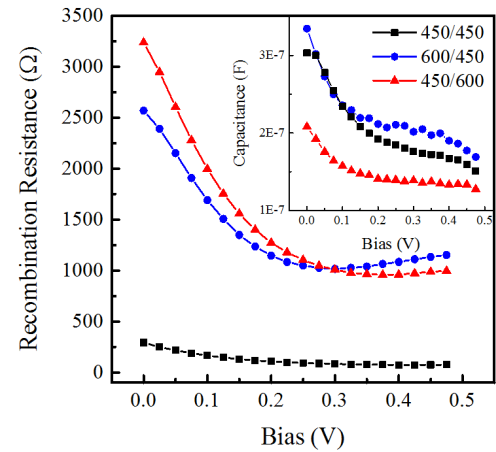


Figure 6.4: Recombination resistance (R_{Rec}) and chemical capacitance (C_μ , inset) are plotted as a function of bias voltage from the model IS data. The model used can be found in Figure 6.14. An order of magnitude increase in R_{Rec} is seen after annealing the nanowire arrays at 600 °C. The R_{Rec} of the annealed wires have a crossover around 0.3 V. The C_μ trend observed matches the recombination lifetimes extracted from the TPV data.

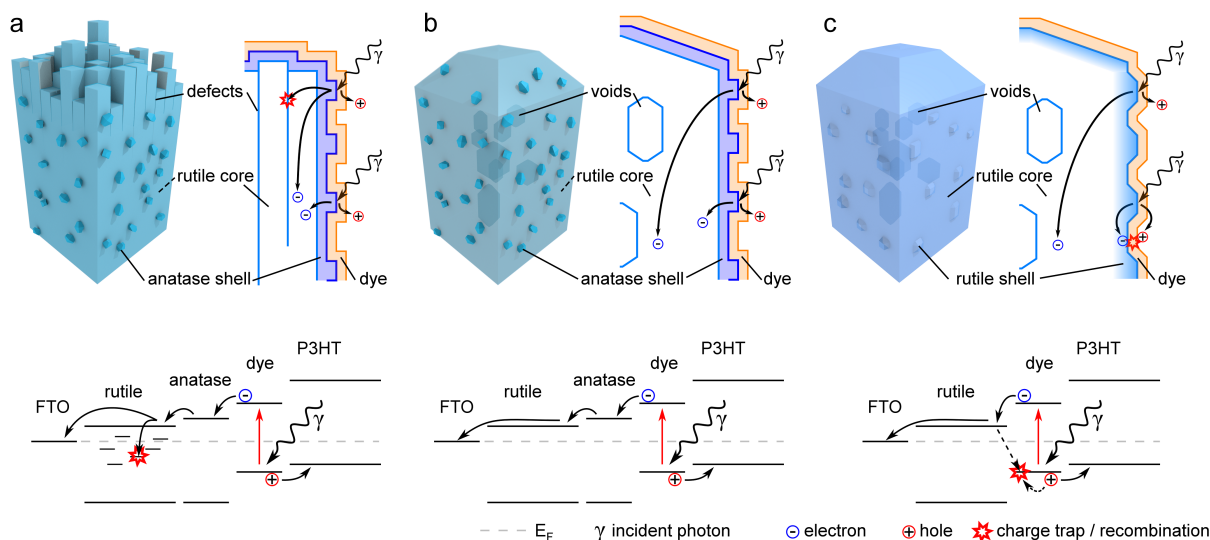


Figure 6.5: A schematic to illustrate the effect of annealing on the nanowire arrays at various time points in the fabrication process (a) 450/450, b) 600/450, c) 450/600). After annealing at higher temperatures, the finger structures that form during the growth process are converted into voids within the wire. Additionally, the shell layer is converted to a rutile film when annealed after TiCl₄ treatment in c). The generated electron is able to move throughout the whole of the nanowire structure in b) and c), instead of an individual finger as in a). Furthermore, the probability of recombination is decreased with a pre-TiCl₄ annealing (a, b) due to the formation of the anatase shell layer which decreases the electron density at the shell. A brief energy level scheme is presented for each sample to highlight the location of trap states and charge recombination probabilities that are present in the device.

resistance (R_{Rec}) and the chemical potential (C_{μ}) are plotted in Figure 6.4. The annealing increases R_{Rec} by an order of magnitude across the full bias range, which corroborates with the increased current densities discussed above. At low biases R_{Rec} is lower for the 600/450 sample than that of the 450/600 sample but this trend inverts around 0.3 V, resulting in a slightly higher R_{Rec} at the maximum power point. The probable cause of this inversion is the interfacial area changed by the annealing process. Specifically, at low forward bias, charges are transported through diffusion, increasing the recombination probability at the imperfect TiO₂/dye/P3HT interface of Sample 600/450 due to residual recombination sites within the anatase shell layer, as against to the defect-free rutile surface of Sample 450/600. At higher forward biases, the charges are not extracted as quickly but the energy offset between the rutile and anatase phases prevents the electrons from reaching the active interface in Sample 600/450, thus reducing the recombination probability. Sample 450/600 does not feature this step in the conduction band, and thus suffers from enhanced recombination at the interface. When C_{μ} is plotted as a function of the bias voltage the capacitance decreases when approaching V_{OC} (inset). Furthermore, C_{μ} shows an inverse trend to the TPV measurements with Sample 450/450 between the high capacitance of Sample 600/450 and the low one in Sample 450/600, indicating a higher charge density in the 600/450 sample and lowest in the 450/600 sample.²⁸ This is attributed to the shell layer, which allows a higher amount of separated charges (electrons in TiO₂, holes in P3HT) near the interface in case of the anatase shell due to the step in



the conduction band for Sample 600/450. The absence of this step allows free spreading of the electrons in Sample 450/600, considerably lowering C_{μ} .

Based on the electrical, optical and structural characterizations, a summarizing schematic is presented in Figure 6.5 to explain the various loss mechanisms present within the system. Sample 600/450 significantly outperforms both, Sample 450/450 and Sample 450/600, in efficiency (2.71 % vs. 2.03 and 2.53 %) due to a quenching in the charge recombination. This is visible in the reduced charge trap density proven by PL, highest EQE and highest recombination resistance near the maximum power point. Lowest lifetime in TPV measurements indicate the highest electron mobility. This improvement is underlined by increased V_{OC} and J_{SC} . These qualities are rendered possible by: (i) a good charge separation made possible via the thin anatase layer covering the rutile core of the wires, introducing a cascading conduction band descending from dye to shell to core, which has been shown to play a beneficial role; (ii) removal of free internal surfaces (i.e., the fingers) and the consequential possibility for charges to spread throughout the nanowires; and (iii) a strong reduction of charge traps due to a cured and mostly defect-free electrode made up by the rutile wire array. The voids which are observed in TEM apparently do not have a severe detrimental effect. As Sample 450/600 is lacking the anatase layer and thus the band cascade, electrons near the TiO_2 /dye interface run the risk of recombining with newly created adjacent holes within the dye layer.

Conclusion

Hydrothermally-grown rutile nanowires were subjected to chemical $TiCl_4$ treatment and a series of HT annealing steps. This enabled the elucidation of the relationship between defect structure and charge dynamics when used as an electrode material, with the aim to identify loss mechanisms detrimental to device performance. By annealing the nanowire arrays at different time points within the fabrication process, it was possible to selectively probe both, the role of the finger structures that naturally form during the growth process and the function of the shell layer on charge separation and transport. The higher annealing temperatures generally boosted device performance. The best overall device performance of 2.71 % (a 35 % improvement compared to the reference) was obtained when the samples were annealed at 600 °C before the $TiCl_4$ surface treatment. In this case, the nanowire core was allowed to rearrange, forming a single crystal throughout the length of the wire, while an anatase shell was formed during the second annealing at 450 °C after the $TiCl_4$ treatment. This process countered three major loss mechanisms within the rutile wires: (i) recombination at the active interface, (ii) the confinement of electrons within a narrow spatial band promoting enhanced recombination, and (iii) a multitude of trap states within the rutile wire core at the free internal surfaces enfolding the fingers. While voids in the wire could be detected after the annealing at 600 °C, they had no observable negative impact on device performance. EQE measurements indicated that the annealing process allowed for more efficient communication with both

the dye and polymer, the latter of which was influenced by the crystal type of the shell layer. The devices with the best performance showed an overall decrease in the recombination lifetime, probed using both TPV and PL of the TiO₂ wires, which indicated a fast non-radiative recombination channel opened by the anatase shell layer when charges are not extracted. A shell layer of rutile instead of anatase increased the electron lifetimes in all characterization methods, suggesting the need to take an effort to understand and engineer the alignment of the energy levels within devices. In general, the presented results strongly suggest that particular caution has to be exercised when dealing with metal-oxide structures. Crystal defects might not be discerned easily in SEM and XRD data, yet still have major influence on device performance, whether that be photovoltaics, energy storage or catalysis.

Supporting Information

Experimental

Film Formation

Nanowire films were grown following the same recipe as previously reported.¹¹ In short, fluorine-doped tin oxide (FTO) substrates (1.4 cm × 1.4 cm) (Solaronix, 8 Ω/□) were cleaned in water, acetone, and 2-propanol for 30 min prior to use. Clean FTO substrates were placed in a Teflon-lined autoclave with 15 mL H₂O, 15 mL concentrated HCl (Sigma-Aldrich), and 525 μL titanium *tert*-butoxide (Sigma-Aldrich, > 99 %) after stirring for 15 min. The autoclaves were heated in an oven for 3 h at 180 °C, after which they were rapidly cooled in a water bath. The nanowire arrays were removed from the solution and washed in DI H₂O three times to remove any excess salt ions. Three sample sets were designated at this point and labeled 450/450, 600/450, and 450/600. Sample 450/450 followed the previous standard recipe with a 450 °C annealing step before and after TiCl₄ treatment, Sample 600/450 was annealed at 600 °C before TiCl₄ and 450 °C after, and Sample 450/600 had a 450 °C step before and 600 °C after TiCl₄ treatment. All samples were annealed for 3 h at the final temperature with a 1 h ramp and a natural cool down.

TiCl₄ Surface Treatment

In order to remove surface defects and increase the surface area, a TiCl₄ (Sigma-Aldrich) surface treatment was performed after the hydrothermal growth and the first annealing step. The pure mesoporous films were treated in a 100 mM TiCl₄ solution. All samples were submerged in the TiCl₄ solution and placed in a water bath for a uniform heating profile. The solution was heated to 70 °C for 3 h and washed with copious amounts of water before the second annealing was performed to remove any hydroxyl ions that form.



Solar Cell Fabrication

Solar-cell fabrication proceeded by emerging the surface treated nanowire arrays in a squaraine dye (SQ2) (Solaronix) dissolved in ethanol (2 mM) for 3 h. Excess dye was removed by rinsing the nanowire arrays with 2-propanol and dried under N₂ gas. The samples were then heated at 120 °C for 1 min to remove any excess solvent that may be present. The samples were then submerged in chlorobenzene (Sigma-Aldrich) for 5 min before a 40 mg/mL poly(3-hexylthiophene-2,5-diyl) in chlorobenzene solution was spin-cast onto the array. The spin parameters were 2 min at 50 rpm to allow for polymer infiltration followed by 1.5 min at 1500 rpm to dry the polymer. The nanowire samples were heated a final time at 120 °C for 5 min in ambient air. Finally, a 130 nm Ag film was thermally evaporated through a shadow mask to complete the device fabrication. Three pixels were deposited with dimensions of 3 mm × 8 mm and an active size of 3 mm × 5 mm.

Device Characterization

Microstructural characterization of the nanowires was performed using a scanning electron microscope (SEM) (Zeiss Gemini Ultra Field Emission) operated at 4 keV accelerating voltage. Transmission electron microscopy (TEM) measurements were performed using a FEI Titan (S)TEM 80-300 operated at 300 kV. Samples were suspended on a 400 mesh carbon-coated TEM grid. X-ray diffraction (XRD) measurements were performed on a Bruker D8 Discovery diffractometer with Cu K α radiation ($\lambda = 1.54 \text{ \AA}$) as X-ray source. The 2θ range was chosen from 20 to 80° and the scanning rate was 0.05°/s with a scanning speed of 0.1 s. UV-vis measurements were performed in a Cary 5000 series UV-vis-NIR spectrometer (Agilent Technologies). Samples were placed in the center of an attached integrating sphere. The absorption spectra were scanned from 800 - 300 nm at a rate of 1 nm/s, a spot size of 1 cm × 5 cm, and referenced to 100 and 0 % transmission. Additionally, the spectra were normalized so that the absorption at 750 nm was 0.

Current density-voltage (J-V) and external quantum efficiency (EQE) measurements were performed using a Keithley 2400 SourceMeter controlled with an in-house LabView program. Cells were enclosed in a light-tight sample holder covering sides and edges, and illuminated via a LOT-Oriel LS0106 solar simulator (AM 1.5G, 100 mW/cm²) through a shadow mask with a resulting active area of 0.125 cm². Light intensities were calibrated with a certified Si reference solar cell (Fraunhofer Institute) with a KG5 filter. Light from a 150 W Xe lamp was passed through a LOT-Oriel Omni 150 monochromator for the EQE measurements. All EQE spectra were normalized to the measured current density at 0 V (the J_{SC}) for accurate comparison. For the light-intensity measurements, the illumination light was passed through a series of neutral-density filters before illumination to obtain light intensities between 10 and 95 mW/cm².

For the transient photodecay measurements (Transient photovoltage decay (TPV) and transient photocurrent decay (TPC)), a pulsed laser (18 Hz, 532 nm) was focused through

the shadow mask onto the sample. The sample was background-illuminated with a LOT-Oriel LS0106 solar simulator with variable light intensities (10-95 mW/cm²). Signals were recorded with a Tekscope DPO 7254 digital oscilloscope. Termination resistances 1 MΩ and 50 Ω were used for TPV and TPC measurements, respectively. Data was fitted with monoexponential decays in order to get an estimate for the characteristic decay lifetimes. Impedance spectroscopy (IS) measurements were conducted with an Ecochemie Autolab Potentiostat/Galvanostat. The samples were placed in a dark, grounded metal box and the spectra were collected with and without a white-light diode at approximately 10 mW/cm². Additionally, the measurements were performed at biases between -0.2 V to 0.65 V with a small AC perturbation using frequencies between 0.1 Hz and 1 MHz. Time-correlated single photon counting (TCSPC) was used in combination with confocal microscopy for time-resolved photoluminescence (PL) measurements. In the studied nanowire samples, PL results from radiative exciton recombination at trap states and its intensity (I_{PL}) is proportional to the product of the absorbed laser fluence (I_{L}) and the PL quantum yield (Q_{PL}) of the material, $I_{\text{PL}} \propto I_{\text{L}} Q_{\text{PL}}$. The quantum yield is defined as the ratio between the radiative decay rate (k_{rad}) and the sum of radiative and non-radiative ($k_{\text{non-rad}}$) decay rates corresponding to $Q_{\text{PL}} = \frac{k_{\text{rad}}}{k_{\text{rad}} + k_{\text{non-rad}}} = k_{\text{rad}} \tau$. Here, we expressed the sum of all decay rates $\tau = (k_{\text{rad}} + k_{\text{non-rad}})^{-1}$ by the excited state lifetime (τ). The combination of PL intensity and lifetime measurements thus provides access to changes in the excited state relaxation and helps to distinguish radiative and non-radiative rate modifications. The material was excited by a Ti:Sapphire oscillator operating at a photon energy of 1.55 eV (800 nm), a repetition rate of 76 MHz and a pulse duration of 150 fs with linear polarization. The PL signal after two photon excitation was detected at higher photon energies between 550 and 750 nm.

Supporting Figures

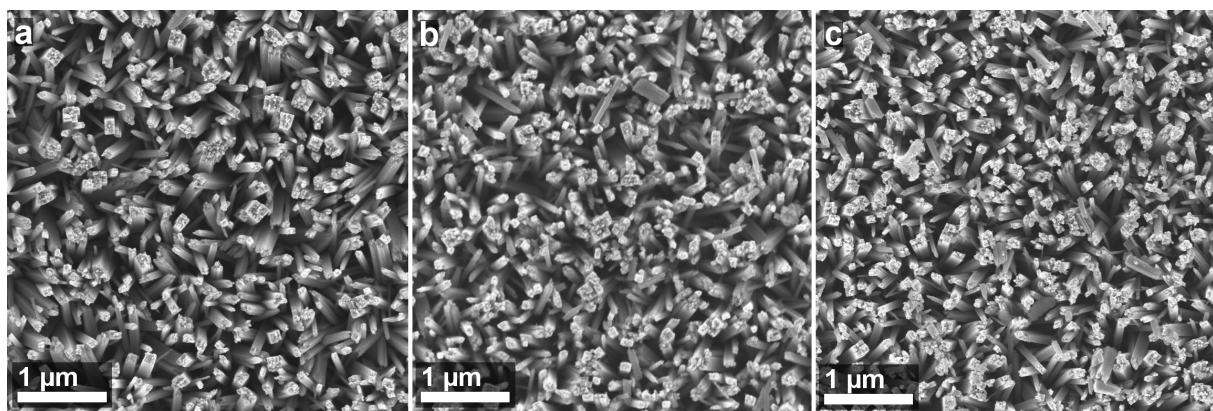


Figure 6.6: An overview of the morphology of the three different samples. The lower magnification SEM micrographs show a homogeneous growth of the wire arrays for all samples. a) 450/450, b) 600/450, and c) 450/600.



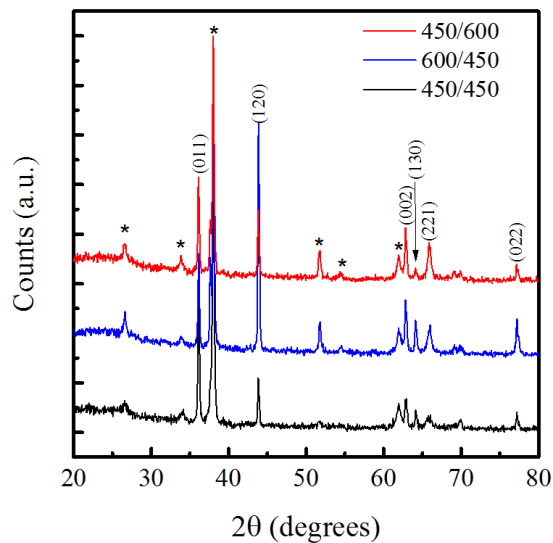


Figure 6.7: The XRD pattern shows rutile phase for all three samples, although the intensities of the peaks vary slightly. The asterisks mark peaks which are correlated to the FTO substrate.

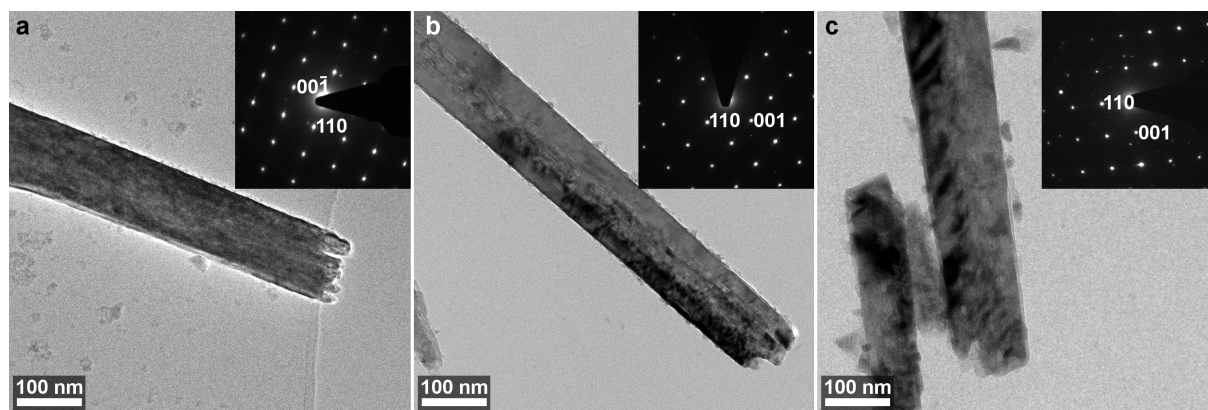


Figure 6.8: TEM bright-field images of exemplary wires. a) 450/450, b) 600/450, and c) 450/600. The finger structure is distinctly visible at the tip of the wire shown in a). b) and c) show wires which include a number of voids within their cores. A thin layer of particles covers the wire surfaces. Electron diffraction patterns are shown as insets and feature the rutile modification for all three samples.

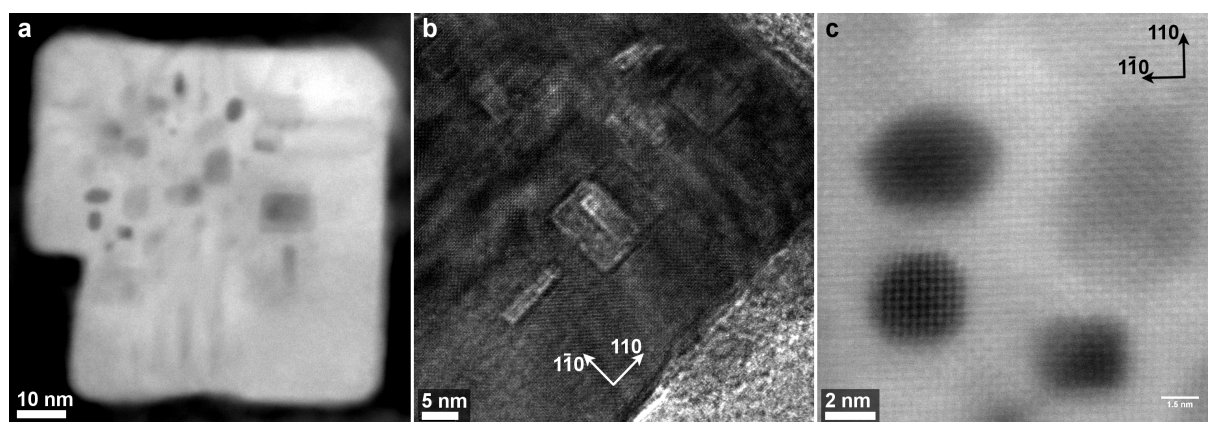


Figure 6.9: TEM cross section of a wire heated at 600 °C. a) STEM micrograph with rectangular voids of different sizes visible near the center of the wire. b) HRTEM micrograph which shows the parallel alignment of the voids with regard to the $\{110\}$ lattice planes. This corresponds to the projection of the Wulff shape of rutile. c) High resolution STEM image of a detail of a).

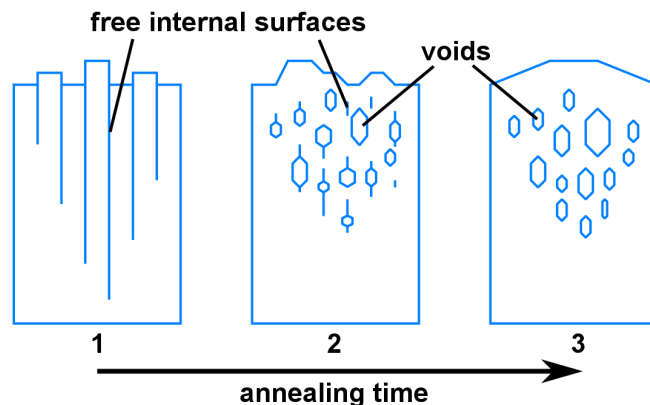
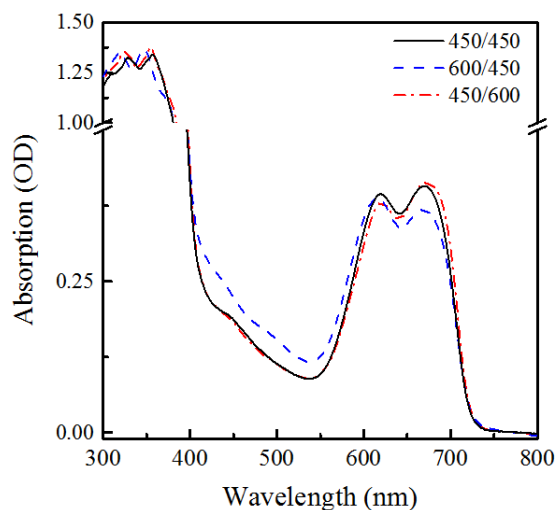


Figure 6.10: Schematic for the formation of the voids. At the beginning of the annealing (step 1), unfilled volume is aggregated along the free internal surfaces between the crystalline fingers. These are artifacts from the hydrothermal growth. During annealing, the rearrangement of the single crystal agglomerates this free volume in larger voids (step 2). At the end of the annealing, the finger structure is completely straightened out. The volume from the former free internal surfaces is now completely aggregated in voids which are roughly shaped in the Wulff shape of rutile (step 3).



Sample	Peak 1 nm	Intensity OD	Peak 2 nm	Intensity OD	Ratio (I_{620}/I_{670})
450/450	619	0.394	670	0.408	0.97
600/450	615	0.388	668	0.369	1.05
450/600	621	0.381	672	0.414	0.92

Figure 6.11: The absorption spectra of the SQ2 on the various TiO₂ surfaces indicate the orientation of the dye loading is directly dependent on when the samples were annealed. While the number of dye molecules is difficult to compare due to variations in light scattering for each sample, a relative comparison indicates no extreme change in the surface area. However, one can see an obvious shift in the peak position, separation, and ratio for the different samples (listed in the respective table), indicative of a direct relationship between core- and shell-layer surface energies with sample processing, forming an internal dipole and shifting electron density across the TiO₂-dye interface. Based on the SEM images discussed in Figure 1, one would expect the absorption between Samples 450/450 and 600/450 to have similar aspects. However, the 600/450 sample shows a blue shift of 4 and 2 nm for the 620 and 670 nm absorption peak, respectively. Additionally, the ratio of the peak intensities ($R_{\frac{620 \text{ nm}}{670 \text{ nm}}}$) is inverted for Sample 600/450 (1.05) with the peak at 620 nm being more intense than the peak at 670 nm when compared to Sample 450/450 (0.97). Sample 450/600 shows a shift of 2 nm for both absorption peaks and the peak ratio is further lowered to 0.92 des-



pite what appears to be a smoother surface than the other two samples. These results suggest that there is a change in the aggregation of the dye molecule with nanowire surface.²⁹ Specifically, it can be concluded that there is an increase in H-aggregation for Sample 600/450 resulting in a higher absorption for the 620 nm peak while Samples 450/450 and 450/600 show an increase in low energy absorption, below that of the monomer (662 nm), due to J-aggregation of the dye along the surface. While it is interesting that the dye aggregation is dependent on the annealing process, the reason for this difference is unclear and will be further investigated in the future.

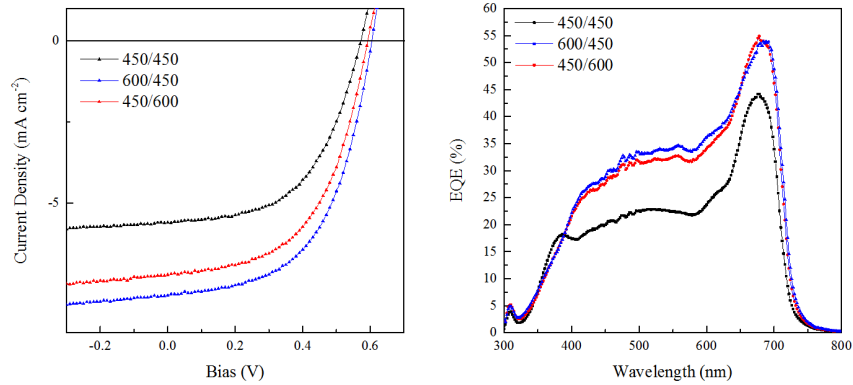


Figure 6.12: Additional device measurements show an identical trend as those in the main work.

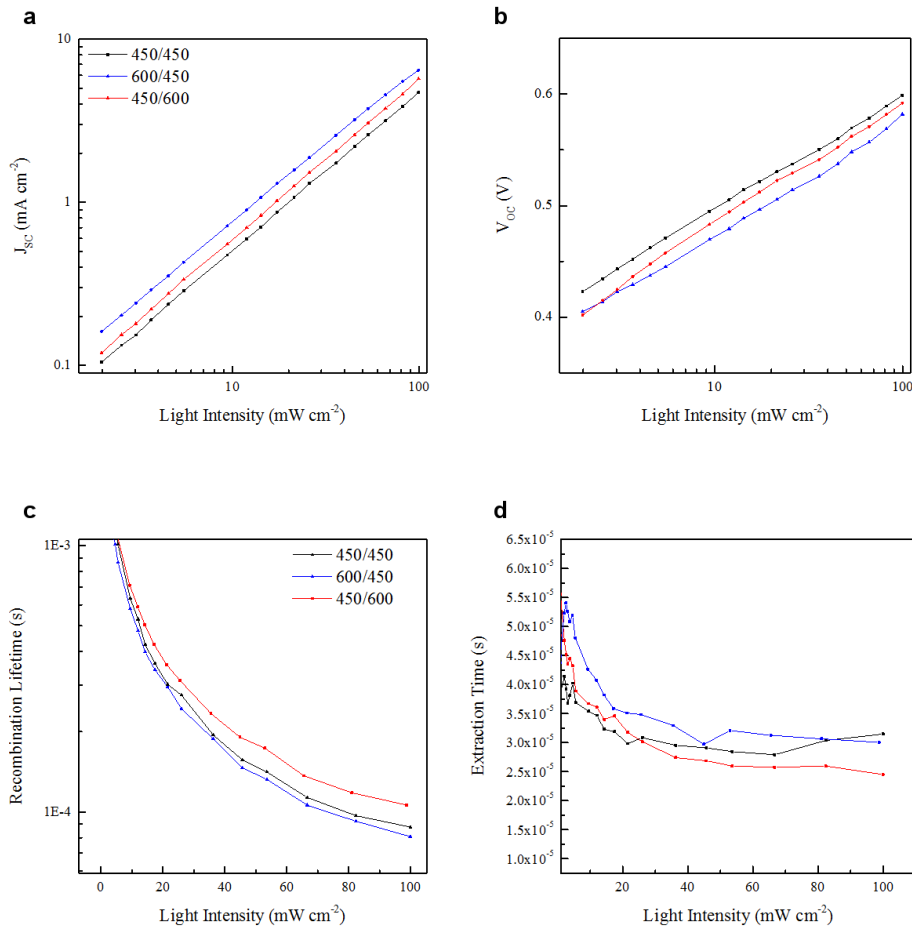


Figure 6.13: a) Light-intensity - current density response, b) - voltage response, c) light-intensity - voltage decay, and d) - current decay were measured to quantify the recombination dynamics at short circuit and open circuit conditions. Charge transport within the devices was probed using intensity-dependent and transient photodecay measurements to study the

changing dynamics with increasing charge density (a, b)). Since the J_{SC} is directly related to the trap state recombination, as there is no buildup of charge at the interface to have direct recombination across this boundary under short-circuit condition, it is possible to extract a qualitative relationship between annealing treatments using the relationship $J_{SC} = \beta P_i^\alpha$ (a)), where P_i is the incident light power and α and β are the power law coefficients.²⁷ A direct correlation between the annealing process and trap-state recombination can be observed from the measurements as Sample 450/450 has a quality factor (α) of 0.936, which can be improved to 0.980 for Sample 600/450 and 0.976 for Sample 450/600. Furthermore, while the difference between the samples annealed at higher temperatures is within error, the observed trend between these two values corresponds well to the J-V measurements presented above. This can be attributed to the rearrangement of the anatase to rutile on the TiO₂ nanowire. Simultaneously, the intensity-dependent voltage measurements were also collected (b)). However, as is common with these nanowire-based hybrid solar cells, the results are difficult to interpret, likely due to the thick overlayer that is required to prevent shortcuts. Lifetimes of the charges were extracted from the transient photodecay measurements to elucidate the charge dynamics at V_{OC} conditions. With the introduction of a small perturbation at the V_{OC} , it is possible to project the charge recombination across the interface at working conditions without directly placing the cell in this state, since there is no variable resistance within the oscilloscope. The transient photovoltage decay (TPV) curves were collected for the same range of illumination values as with the J_{SC} light intensity dependent measurements and fit using a single-exponential decay process. It can be seen in c) that the recombination lifetime for all samples is dependent on the light intensity, as expected, with decreasing carrier lifetimes for increasing background illumination intensities. However, the recombination lifetime of Sample 600/450 is slightly shorter than that of Sample 450/450, 81 vs. 88 μ s at AM 1.5G illumination. This is in accordance to the PL lifetime measurements and might be attributed to the increased charge density in Sample 600/450. An increase in recombination lifetime is observed for Sample 450/600 with a lifetime of 106 μ s at full illumination, the trend again coinciding with the PL lifetime. By annealing the nanowire array after shell deposition, a continuous textured rutile structure is obtained. While this reduces the charge injection, resulting in a lower overall current than shown by Sample 600/450, the charge recombination lifetime increases due to the ability of electrons to flow throughout the whole wire as opposed to being located solely at the interface as is the case with the finger structures that are present in Sample 450/450. Note that the wires have a smooth surface as discussed above, limiting the contact area with the P3HT. For a given recombination rate per unit area such a decrease in interfacial area results in a further increased macroscopic recombination lifetime.

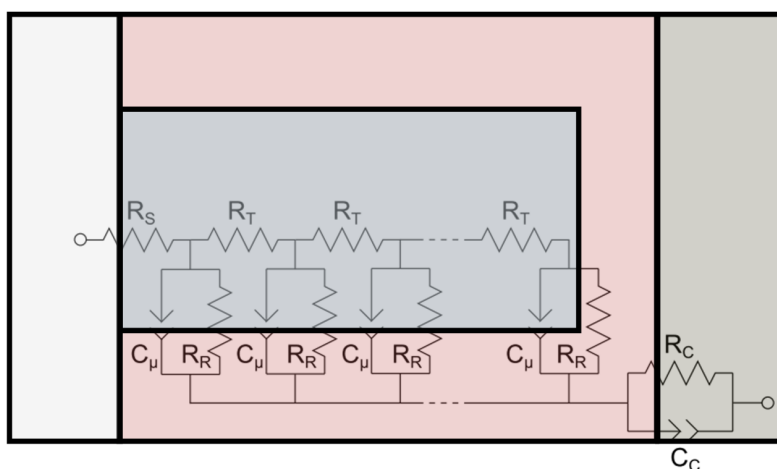


Figure 6.14: Impedance spectroscopy model used to fit the measured data. The model includes a series resistance (R_S) across the ITO-TiO₂ interface, a transmission resistance (R_T) through the TiO₂ nanowire, a RC circuit with recombination resistance R_R/R_{Rec} and chemical capacitance C_μ , and a second RC circuit (R_C and C_C) for the metal polymer interface.



Concluding Remarks on Pathways to More Efficient Hybrid Solar Cell Devices

The work on 1D nanostructured TiO₂ electrode materials presented here is considered as one cornerstone to a general route to improvement of hybrid solar cells. It concentrates on the elucidation of nanostructures, with a focus on intrinsic defect structures related to the growth conditions. However, it is only one part of a larger project, which comprises diverse starting points and perspectives on the according devices. First, some closely-related work was conducted on the incorporation of Sn⁴⁺ ions in hydrothermally-grown rutile wires by addition of a Sn:HCl precursor directly to the solution before hydrothermal growth.¹¹ TEM investigations were performed, which revealed that the TiCl₄ treatment lead to a uniform anatase layer decorated with small anatase nanoparticles. Notwithstanding that the concentration of Sn within the wires was below the detection limit of EDX and EELS its effect on solar cell performance was clearly visible. The EQE was strongly improved throughout ultraviolet (UV) and visible spectrum, with an emphasis on the range below 400 nm, indicating an enhanced absorption by the TiO₂. The PCE was boosted from 1.9 % to 2.5 %.

During the investigation on hydrothermal growth of rutile nanowires, additional experiments were performed with the aim of adding other metal-oxide shell layers.^{30,31} The device performance was only moderately improved. However, a new Nb₃O₇(OH) morphology was discovered during the different experiments.³² Consisting of a mesoporous network of single-crystalline nanowires which form larger hollow orthogonal cubes, the particles exhibited good photocatalytic activity. A peculiar crystalline structure could be detected at the junctions of the network, caused by the similarity of crystal parameters *b* and *c*. Here, the single nanowires are merging together, forming a cross without distinct grain boundaries. Yet, the suitability of these structures for hybrid solar cells is still to be investigated.

Another cornerstone of the project is the improvement of organic dyes, electrolyte and interfacial modifiers. Co-workers were able to find a highly beneficial combination of 4-mercaptopyridine (4-MP) and 4-*tert*-butylpyridine (*t*BP) sensitizers to boost the performance of a TiO₂/SQ2/P3HT solar cell.²⁴ The legacy TiO₂/SQ2/*t*BP/4-MP/P3HT cell displayed an efficiency increase from 1.3 % to 1.8 %. This was attributed to a favorable band alignment, as well as the face-on assembly of P3HT due to the modifiers. The importance of the P3HT alignment has been discussed before within the scope of a different project.³³

Considering the results gathered here, it is but natural to strongly suggest the incorporation of all findings into a fully optimized hybrid solar cell. The characteristics of a device implementing an Sn-doped rutile nanowire electrode heated at 600 °C before TiCl₄ treatment, together with an SQ2 dye, *t*BP and 4-MP sensitizers, and P3HT are eagerly awaited.

Bibliography

- [1] X. Chen and S. S. Mao, "Titanium dioxide nanomaterials: Synthesis, properties, modifications, and applications," *Chemical Reviews*, vol. 107, no. 7, pp. 2891–2959, 2007.
- [2] A. R. Armstrong, G. Armstrong, J. Canales, R. García, and P. G. Bruce, "Lithium-ion intercalation into TiO₂-B nanowires," *Advanced Materials*, vol. 17, no. 7, pp. 862–865, 2005.
- [3] J. Wu and R. L. McCreery, "Solid-state electrochemistry in molecule/TiO₂ molecular heterojunctions as the basis of the TiO₂ memristor," *Journal of The Electrochemical Society*, vol. 156, no. 1, pp. P29–P37, 2009.
- [4] L. Kavan, M. Kalbáč, M. Zukulová, I. Exnar, V. Lorenzen, R. Nesper, and M. Grätzel, "Lithium storage in nanostructured TiO₂ made by hydrothermal growth," *Chemistry of Materials*, vol. 16, no. 3, pp. 477–485, 2004.
- [5] S. N. Habisreutinger, L. Schmidt-Mende, and J. K. Stolarczyk, "Photocatalytic reduction of CO₂ on TiO₂ and other semiconductors," *Angewandte Chemie International Edition*, vol. 52, no. 29, pp. 7372–7408, 2013.
- [6] G. K. Mor, S. Kim, M. Paulose, O. K. Varghese, K. Shankar, J. Basham, and C. A. Grimes, "Visible to near-infrared light harvesting in TiO₂ nanotube array-P3HT based heterojunction solar cells," *Nano Letters*, vol. 9, no. 12, pp. 4250–4257, 2009.
- [7] A. Yella, H.-W. Lee, H. N. Tsao, C. Yi, A. K. Chandiran, M. Nazeeruddin, E. W.-G. Diao, C.-Y. Yeh, S. M. Zakeeruddin, and M. Grätzel, "Porphyrin-sensitized solar cells with cobalt (II/III)-based redox electrolyte exceed 12 percent efficiency," *Science*, vol. 334, no. 6056, pp. 629–634, 2011.
- [8] S. A. Bretschneider, J. Weickert, J. A. Dorman, and L. Schmidt-Mende, "Research update: Physical and electrical characteristics of lead halide perovskites for solar cell applications," *APL Materials*, vol. 2, no. 4, 2014.
- [9] H. Zhou, Q. Chen, G. Li, S. Luo, T.-b. Song, H.-S. Duan, Z. Hong, J. You, Y. Liu, and Y. Yang, "Interface engineering of highly efficient perovskite solar cells," *Science*, vol. 345, no. 6196, pp. 542–546, 2014.
- [10] E. J. W. Crossland, N. Noel, V. Sivaram, T. Leijtens, J. A. Alexander-Webber, and H. J. Snaith, "Mesoporous TiO₂ single crystals delivering enhanced mobility and optoelectronic device performance," *Nature*, vol. 495, pp. 215–219, 2013.
- [11] J. A. Dorman, J. Weickert, J. B. Reindl, M. Putnik, A. Wisnet, M. Noebels, C. Scheu, and L. Schmidt-Mende, "Control of recombination pathways in TiO₂ nanowire hybrid solar cells using Sn⁴⁺ dopants," *The Journal of Physical Chemistry C*, vol. 118, no. 30, pp. 16672–16679, 2014.
- [12] X. Feng, K. Zhu, A. J. Frank, C. A. Grimes, and T. E. Mallouk, "Rapid charge transport in dye-sensitized solar cells made from vertically aligned single-crystal rutile TiO₂ nanowires," *Angewandte Chemie International Edition*, vol. 51, no. 11, pp. 2727–2730, 2012.
- [13] B. Liu and E. S. Aydil, "Growth of oriented single-crystalline rutile TiO₂ nanorods on transparent conducting substrates for dye-sensitized solar cells," *Journal of the American Chemical Society*, vol. 131, no. 11, pp. 3985–3990, 2009.
- [14] A. Wisnet, S. B. Betzler, R. V. Zucker, J. A. Dorman, P. Wagatha, S. Matich, E. Okunishi, L. Schmidt-Mende, and C. Scheu, "Model for hydrothermal growth of rutile wires and the associated development of defect structures," *Crystal Growth & Design*, vol. 14, no. 9, pp. 4658–4663, 2014.
- [15] E. J. W. Crossland, M. Nedelcu, C. Ducati, S. Ludwigs, M. A. Hillmyer, U. Steiner, and H. J. Snaith, "Block copolymer morphologies in dye-sensitized solar cells: Probing the photovoltaic structure-function relation," *Nano Letters*, vol. 9, no. 8, pp. 2813–2819, 2009.
- [16] E. Hendry, M. Koeberg, B. O'Regan, and M. Bonn, "Local field effects on electron transport in nanostructured TiO₂ revealed by terahertz spectroscopy," *Nano Letters*, vol. 6, no. 4, pp. 755–759, 2006.
- [17] Y. Zhao, X. Gu, and Y. Qiang, "Influence of growth time and annealing on rutile TiO₂ single-crystal nanorod arrays synthesized by hydrothermal method in dye-sensitized solar cells," *Thin Solid Films*, vol. 520, no. 7, pp. 2814 – 2818, 2012.



- [18] A. Hagfeldt, G. Boschloo, L. Sun, L. Kloo, and H. Pettersson, "Dye-sensitized solar cells," *Chemical Reviews*, vol. 110, no. 11, pp. 6595–6663, 2010.
- [19] X. Wang, Z. Feng, J. Shi, G. Jia, S. Shen, J. Zhou, and C. Li, "Trap states and carrier dynamics of TiO₂ studied by photoluminescence spectroscopy under weak excitation condition," *Physical Chemistry Chemical Physics*, vol. 12, pp. 7083–7090, 2010.
- [20] H. Sezen, M. Buchholz, A. Nefedov, C. Natzeck, S. Heissler, C. D. Valentin, and C. Wöll, "Probing electrons in TiO₂ polaronic trap states by IR-absorption: Evidence for the existence of hydrogenic states," *Scientific Reports*, vol. 4, p. 3808, 2014.
- [21] T. Berger, T. Lana-Villarreal, D. Monllor-Satoca, and R. Gómez, "An electrochemical study on the nature of trap states in nanocrystalline rutile thin films," *The Journal of Physical Chemistry C*, vol. 111, no. 27, pp. 9936–9942, 2007.
- [22] T. Gokus, L. Cognet, J. G. Duque, M. Pasquali, A. Hartschuh, and B. Lounis, "Mono- and biexponential luminescence decays of individual single-walled carbon nanotubes," *The Journal of Physical Chemistry C*, vol. 114, no. 33, pp. 14025–14028, 2010.
- [23] J.-S. Yang, W.-P. Liao, and J.-J. Wu, "Morphology and interfacial energetics controls for hierarchical anatase/rutile TiO₂ nanostructured array for efficient photoelectrochemical water splitting," *ACS Applied Materials & Interfaces*, vol. 5, no. 15, pp. 7425–7431, 2013.
- [24] J. Weickert, E. Zimmermann, J. B. Reindl, T. Pfadler, J. A. Dorman, A. Petrozza, and L. Schmidt-Mende, "Synergistic effects of interfacial modifiers enhance current and voltage in hybrid solar cells," *APL Materials*, vol. 1, no. 4, 2013.
- [25] E. Zimmermann, P. Ehrenreich, T. Pfadler, J. A. Dorman, J. Weickert, and L. Schmidt-Mende, "Erroneous efficiency reports harm organic solar cell research," *Nature Photonics*, vol. 8, pp. 669–672, 2014.
- [26] E. V. Canesi, M. Binda, A. Abate, S. Guarnera, L. Moretti, V. D'Innocenzo, R. Sai Santosh Kumar, C. Bertarelli, A. Abrusci, H. Snaith, A. Calloni, A. Brambilla, F. Ciccacci, S. Aghion, F. Moia, R. Ferragut, C. Melis, G. Mallocci, A. Mattoni, G. Lanzani, and A. Petrozza, "The effect of selective interactions at the interface of polymer-oxide hybrid solar cells," *Energy & Environmental Science*, vol. 5, pp. 9068–9076, 2012.
- [27] J. van de Lagemaat, N.-G. Park, and A. J. Frank, "Influence of electrical potential distribution, charge transport, and recombination on the photopotential and photocurrent conversion efficiency of dye-sensitized nanocrystalline TiO₂ solar cells: A study by electrical impedance and optical modulation techniques," *The Journal of Physical Chemistry B*, vol. 104, no. 9, pp. 2044–2052, 2000.
- [28] J. Bisquert, "Chemical capacitance of nanostructured semiconductors: its origin and significance for nanocomposite solar cells," *Physical Chemistry Chemical Physics*, vol. 5, pp. 5360–5364, 2003.
- [29] G. Chen, H. Sasabe, Y. Sasaki, H. Katagiri, X.-F. Wang, T. Sano, Z. Hong, Y. Yang, and J. Kido, "A series of squaraine dyes: Effects of side chain and the number of hydroxyl groups on material properties and photovoltaic performance," *Chemistry of Materials*, vol. 26, no. 3, pp. 1356–1364, 2014.
- [30] S. B. Betzler, "Synthesis and characterization of TiO₂ and Nb_xO_y nanostructures." Master Thesis in Chemistry at the Ludwig-Maximilians-University Munich, 2012.
- [31] A. Folger, "Investigation of TiO₂/Nb_xO_y core-shell nanostructures for application in hybrid solar cells." Master Thesis in Chemistry at the Ludwig-Maximilians-University Munich, 2013.
- [32] S. B. Betzler, A. Wisnet, B. Breitbach, C. Mitterbauer, J. Weickert, L. Schmidt-Mende, and C. Scheu, "Template-free synthesis of novel, highly-ordered 3D hierarchical Nb₃O₇(OH) superstructures with semiconductive and photoactive properties," *Journal of Materials Chemistry A*, vol. 2, pp. 12005–12013, 2014.
- [33] M. Handloser, R. B. Dunbar, A. Wisnet, P. Altpeter, C. Scheu, L. Schmidt-Mende, and A. Hartschuh, "Influence of metallic and dielectric nanowire arrays on the photoluminescence properties of P3HT thin films," *Nanotechnology*, vol. 23, no. 30, p. 305402, 2012.

Chapter 7

Electron Tomography as Key to the Understanding of Particle Properties at the Nanoscale

7.1 DART Reconstruction of a Gold Nanoparticle

The following section describes the 3D reconstruction of a gold nanostar in detail. The result has been included in the publication mentioned below. The scientific conclusions from the paper are described accordingly.

Quantitative understanding of the optical properties of a single, complex-shaped gold nanoparticle from experiment and theory

E. M. Perassi, C. Hrelescu, **A. Wisnet**, M. Döblinger, C. Scheu, F. Jäckel, E. A. Coronado, J. Feldmann; *ACS Nano*, **2014**, 8(5), 4395-4402

Original Abstract We report on a combined study of Rayleigh and Raman scattering spectroscopy, 3D electron tomography, and discrete dipole approximation (DDA) calculations of a single, complex-shaped gold nanoparticle (NP). Using the exact reconstructed 3D morphology of the NP as input for the DDA calculations, the experimental results can be reproduced with unprecedented precision and detail. We find that not only the exact NP morphology but also the surroundings including the points of contact with the substrate are of crucial importance for a correct prediction of the NP optical properties. The achieved accuracy of the calculations allows determining how many of the adsorbed molecules have a major contribution to the Raman signal, a fact that has important implications for analyzing experiments and designing sensing applications.

Material and Scientific Interest

Gold nanoparticles can be fabricated in a solution-based chemical procedure at room temperature in a wide range of shapes.¹ By changing the concentrations of seed particles, the components of the solution, cetyltrimethylammonium bromide (CTAB) and H₂AuCl₄



(ascorbic acid), and the possible addition of AgNO_3 , cuboids, pyramids, dodecahedrons or more complex shaped particles like tetra-pods and multi-pods ("nanostars") can be synthesized. This multitude is possible due to the preferred binding of CTAB on $\{100\}$ gold facets.² The gold nanoparticles are drawn into focus of scientific research by their remarkable optical properties which are utilized, amongst others, in surface-enhanced Raman spectroscopy (SERS),³⁻⁷ tip-enhanced Raman spectroscopy,^{8,9} nanolithography¹⁰ and the design of tips for scanning near-field optical microscopy.¹¹ As these properties are strongly dependent on shape, size and composition of the particles, the determination of the parameters is of crucial importance. In particular, the excitation of localized surface plasmon resonances (LSPRs), which originate from collective oscillations of the conduction band electrons, are widely tunable and exhibit large field enhancements.¹² By combining the discrete dipole approximation (DDA) algorithm^{13,14} with the capabilities of electron tomographic reconstruction, it is possible to reach an in-depth understanding of the interdependence between particle morphology and electro-optical behavior.¹⁵ The central point of DDA is the reduction of the particle of interest to a finite number of small elements. When an external electrical field, i.e. an electromagnetic wave, is applied, each element behaves as a separate dipole which simultaneously interacts with the external electrical field and the field emanating from the surrounding elements. Thus, the scattering response of the particle can be calculated.

Reconstruction

Keeping in mind the overview given in Section 3.2, the description of the problem makes it clear that the SIRT algorithm can not be utilized alone to give reliable reconstructions which are suited to serve as input to the DDA algorithm. Two major problems can be identified here: First, the unconstrained SIRT algorithm tends to give small parts of the reconstruction gray values below zero, which in turn results in areas with too large material density, ending in the occurrence of artifacts. As these have a strong impact on the DDA,¹⁵ they have to be avoided. Secondly, due to a continuous range of gray values for the reconstruction, the segmentation has to be performed afterwards by manually setting the threshold. This is bound to introduce errors in shape and size of the reconstructed particle. The DART algorithm does not suffer from the aforementioned detriments, as the reconstruction can, in the present case, only consist of one positive gray value (apart from the vacuum zero level). In addition, this gray value is found by the application of the masked SIRT algorithm introduced by Zürner et al.¹⁶ combined with the determination of the lowest variation between projections and reprojections, and therefore more reliable. Figure 7.1a shows a BF overview of the gold nanoparticle with a highly irregular structure (thus nanostar). After careful subtraction of the background and application of the landmark-based alignment,¹⁷ which includes a rotation of the images, the resulting (HA)ADF projection at tilt angle 0° ("zero projection") is shown in Figure 7.1b with intensities ranging between 0 and 9710. An excerpt of the full

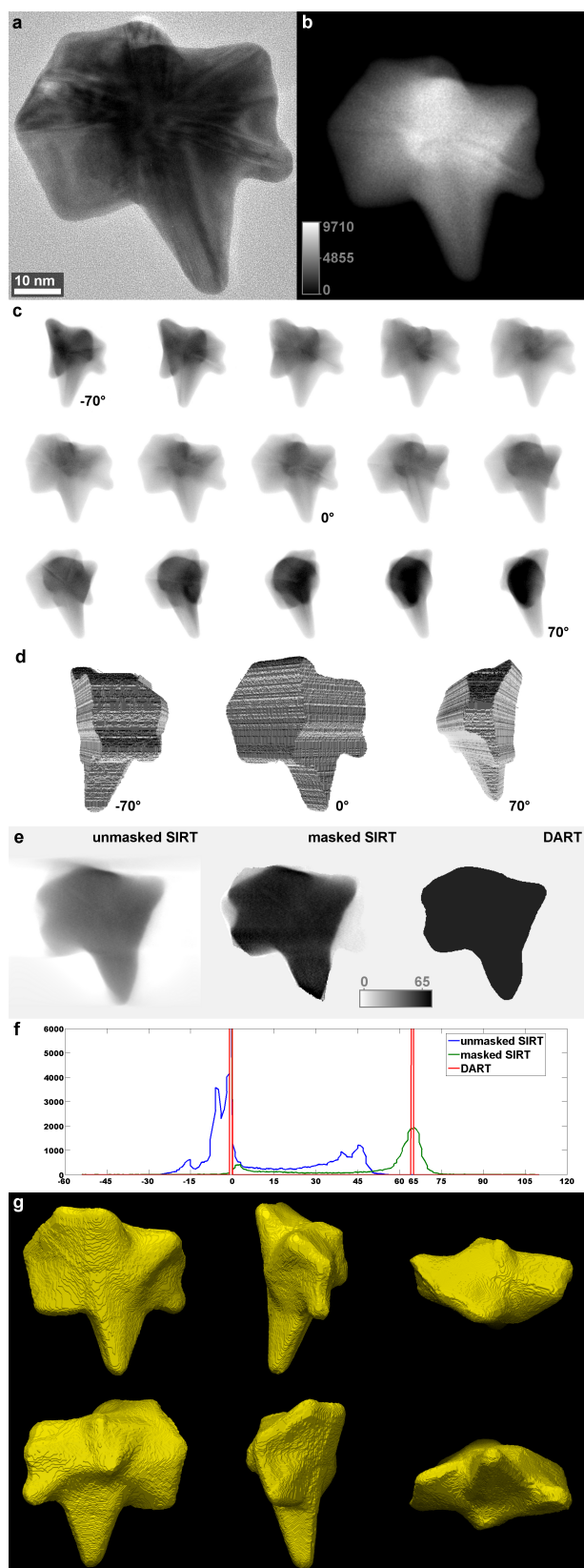


Figure 7.1: a) BF overview of the nanostar. b) (HA)ADF zero projection after alignment and background subtraction. c) Inverted excerpt of the aligned series at 10° increments from -70 to $+70^\circ$. d) Perspective images of the mask. e) Comparison of central slices after the three reconstruction algorithms. f) Histograms of the three slices in e). g) Final DART reconstruction.¹⁸ BF images and (HA)ADF series were recorded by Markus Döblinger.

tilt series, which has been recorded with tilt increments of 2° , is shown in Figure 7.1c. These are the inverted projections from -70 to $+70^\circ$, with tilt increments of 10° . Inhomogeneities within the projections point towards some residual Bragg contrast. However, due to the high number of projections, 71 in total, their influence on reconstruction is minimized. A simple algorithm was developed to generate a mask of the particle to enable a restricted SIRT reconstruction according to Zürner et al.¹⁶ For this purpose, three projections were picked (-70 , 0 and $+70^\circ$), all pixels with intensity below the mean value were set to zero and all above or equal mean to one. These 2D masks were back-projected at according angles to a volume containing only voxels with the value one. A strong constraint was applied that all voxels of the volume graced by a ray of one back-projection with the value 0 are set to 0. This method enables a fast and simple construction of a mask which is not subject to inaccurate estimates. The algorithm developed for this purpose can also be extended to use any number of projections for the generation of a mask. Figure 7.1d shows three perspectives of the mask resulting in case of the nanostar. To demonstrate the difference between masked and unmasked SIRT reconstruction, Figure 7.1e displays a slice through the final reconstructions after 30 iterations each, including the subsequent DART reconstruction. It is obvious, that the gray values for the masked SIRT



reconstruction are consistently higher. Figure 7.1f shows the histograms of the according slices in e). There is a distinct peak at the gray value of 65, which has therefore been chosen for DART reconstruction. The final DART reconstruction is shown in Figure 7.1g.

Results

The importance of the reconstruction described here becomes obvious when taking a look at the flowchart diagram presented in Figure 7.2. For the whole study, a single nanoparticle was chosen for experimental and theoretical examination. To add complexity to the investigation, its surface was functionalized by 4-mercaptobenzoic acid (MBA) which produces a Raman signal.¹²

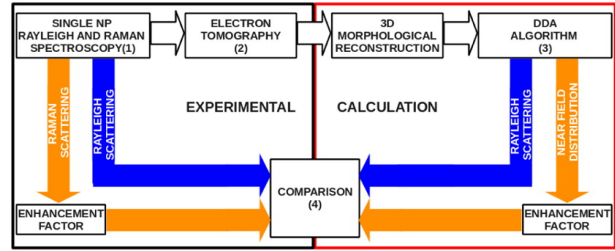


Figure 7.2: Flowchart of the experimental and theoretical approach.¹⁸

In short, experimentally determined Rayleigh and Raman spectra were measured and compared to the results of the DDA approach which was realized with the help of a 3D reconstruction of the nanostar morphology. Figure 7.3 shows the comparison between the measured and the calculated Rayleigh scattering spectra for different polarizations.¹⁸ It is obvious that the anisotropy of the nanostar has a considerable influence on the scattering process. When the incoming light is polarized along the longer axis (Figures 7.3a, b and g), the peak position tends to be reproduced more correctly. However, this is possible only due to the consideration of the MBA molecules, the substrate and the contact points of the nanostar to the substrate, which could be identified straight-forward due to the superior DART reconstruction. The complexity of the particle makes it harder to simulate the other polarization conditions, but the fact that the existence of two separate peaks in

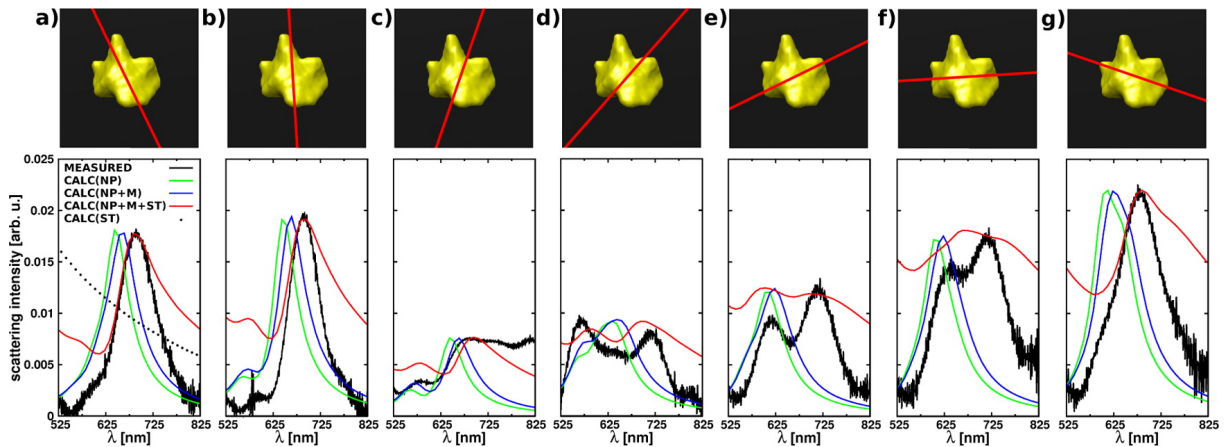


Figure 7.3: (a-g) Measured and simulated Rayleigh scattering spectra for each incident polarization which is indicated by a red line in the corresponding image in the top panel of each Figure. Black curves: measured scattering spectra (integration time = 120 s). Green curves: simulated scattering spectra without any substrate and molecules. Blue curves: simulated scattering spectra considering the MBA molecules. Red curves: simulated scattering spectra considering the MBA molecules and the substrate.¹⁸

Figures 7.3d and e can be reproduced by calculation is in itself a good accomplishment. As the influence of the substrate is evident, it is obvious that part of the error in the simulation spectra can be ascribed to the finite nature of the simulation thereof, which is confined to a certain size due to computing capacity.

Figures 7.4a and b show the Raman scattering signal from two distinct polarizations.¹⁸ The Raman shift is caused by the MBA molecules adsorbed on the surface of the nanostar. The stronger confinement of the electrical field in case **b** leads to a visibly higher signal. Calculating a simulated enhancement factor Γ led to the conclusion that in case **b** significant more molecules are excited than in case **a**, as is depicted in the models, where values

$\Gamma > 100$ were present only in case **b**. In conclusion, by combining experiment, 3D reconstruction and theory, the suitability of the DDA for the prediction of the optical response of nanoparticles could be corroborated. However, it is obvious that the quality of the tomographical efforts is decisive to the accuracy of the according simulations. DART has been proven as adequate reconstruction algorithm.

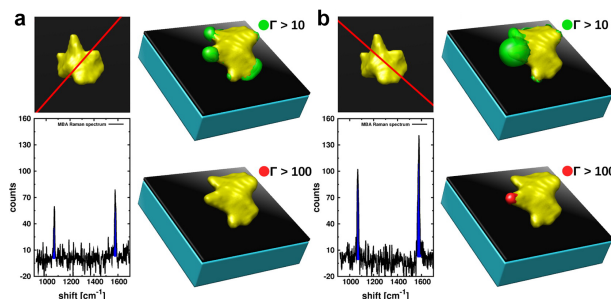


Figure 7.4: Measured Raman shift for two different polarizations (a, b) and the calculated enhancement factor Γ .¹⁸

7.2 Reconstruction of Multiple Iron-Based Particles on Few Trenched Layers of Graphene

The following section describes the 3D reconstruction of multi-layered graphene decorated with iron-based particles in detail. The result has been included in the publication mentioned below. The scientific conclusions from the paper are described accordingly.

A 3D insight on the catalytic nanostructuring of few-layer graphene

G. Melinte, I. Florea, S. Moldovan, I. Janowska, W. Baaziz, R. Arenal, **A. Wisnet**, C. Scheu, S. Begin-Colin, D. Begin, C. Pham-Huu, O. Ersen; *Nature Communications*, **2014**, *5*, 4109

Original Abstract The catalytic cutting of few-layer graphene is nowadays a hot topic in materials research due to its potential applications in the catalysis field and the graphene nanoribbons fabrication. We show here a 3D analysis of the nanostructuring of few-layer graphene by iron-based nanoparticles under hydrogen flow. The nanoparticles located at the edges or attached to the steps on the FLG sheets create trenches and tunnels with orientations, lengths and morphologies defined by the crystallography and the topography of the carbon substrate. The cross-sectional analysis of the 3D volumes highlights the role of the active nanoparticle identity on the trench size and shape, with emphasis on the



topographical stability of the basal planes within the resulting trenches and channels, no matter the obstacle encountered. The actual study gives a deep insight on the impact of nanoparticles morphology and support topography on the 3D character of nanostructures built up by catalytic cutting.

Material and Scientific Interest

Graphene, the single layer of sp^2 -bonded carbon atoms, possesses unique physical, chemical and mechanical properties.¹⁹ While strong improvements are made in the fields of electronics like touch screens, organic light-emitting diodes (OLEDs) and transistors,²⁰ its superior thermal and chemical stability make it suitable for the support in liquid- and gas-phase catalysis.²¹ Multi-layered graphene is easier to fabricate but equally usable for this application.^{21,22} The addition of layers naturally induces new sites of interest where the single layers end. These steps within the material are of particular interest during catalysis. The present study used Fe-based (Fe, Fe_2O_3) nanoparticles in an H_2 atmosphere to introduce trenches in the graphene layers, as has been shown before.²³ A 2D approach (i.e. two-dimensional TEM micrographs) can not give satisfying information about the behavior of the nanoparticles during catalysis. Thus, electron tomography was drawn on to learn more about the relationships between trenches and the location of the nanoparticles.

Reconstruction and Results

As most of the analytical work was done by the group of Prof. Ersen by the sophisticated use of SIRT reconstructions, the DART reconstructions done in this context are mainly performed to provide an overview of the positions of the nanoparticles on a large scale. One difference to the study described in Section 7.1 is that the data in this case does not consist of STEM micrographs but BF images. However, as the vacuum is depicted in each projection, background subtraction is straight forward. Alignment was done in advance by the Tomo3D software.²⁴ Figure 7.5a shows the aligned and background-subtracted zero projection. To allow for the specific masked SIRT and DART algorithms, the data were inverted and vacuum set to zero level, as depicted in Figure 7.5b. To provide a suitable mask is more complicated than in the case of single nanoparticles, due to a larger area that has to be reconstructed. Additionally, the substrate is of interest as well and has therefore to be included in the reconstruction. Figure 7.5c shows an xy-slice through the first SIRT reconstruction. The yellow line indicates the position of the xz-slice depicted in d). By careful consideration of the features present, a mask could be constructed by combining the method presented before with a limitation to a determined band in z direction (Figure 7.5e). The masked SIRT reconstruction is shown in Figure 7.5f, while g) and h) are a comparison of the original zero projection (g) with the reprojection derived from the DART model. A movie displaying the DART reconstruction can be found online.ⁱ

ⁱ<http://www.nature.com/ncomms/2014/140611/ncomms5109/extref/ncomms5109-s2.avi>

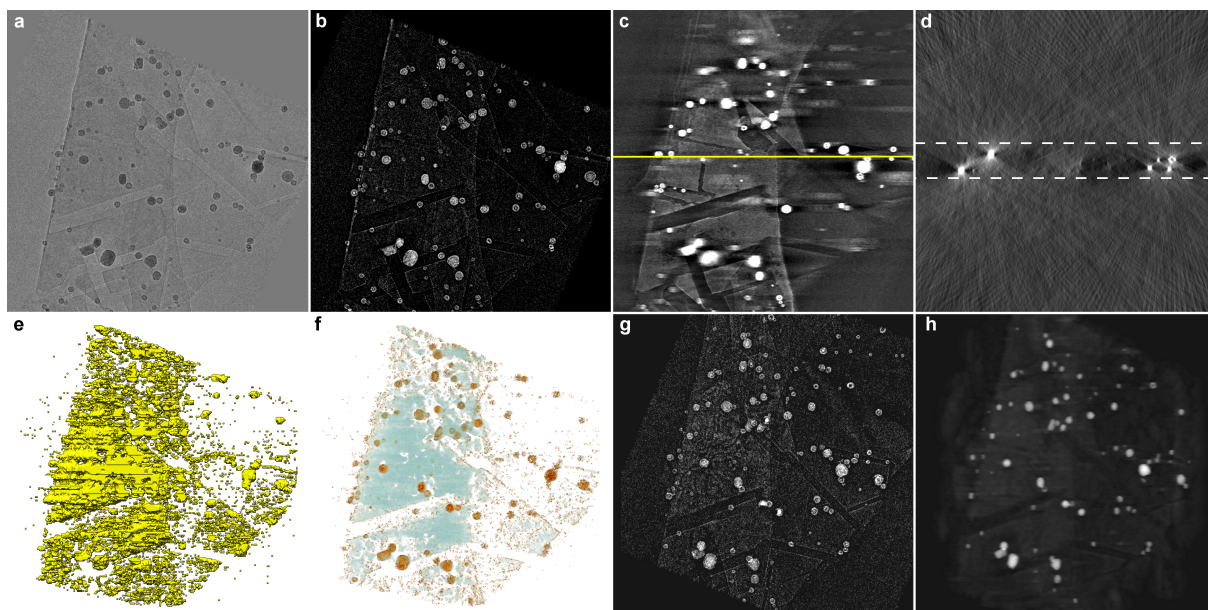


Figure 7.5: Reconstruction of few-layered graphene and incorporated Fe-based nanoparticles after catalysis. a) BF image of the area of interest. b) The same area as in a) after background subtraction and inversion for reconstruction. c) Xy-slice of the first SIRT reconstruction with a yellow line, marking d), an exemplary xz-slice, which were used for determination of the mask limits. e) Mask used for f), the masked SIRT reconstruction. g) Is the zero projection compared to h), the reprojection of the final DART reconstruction. Series acquisition by I. Florea.

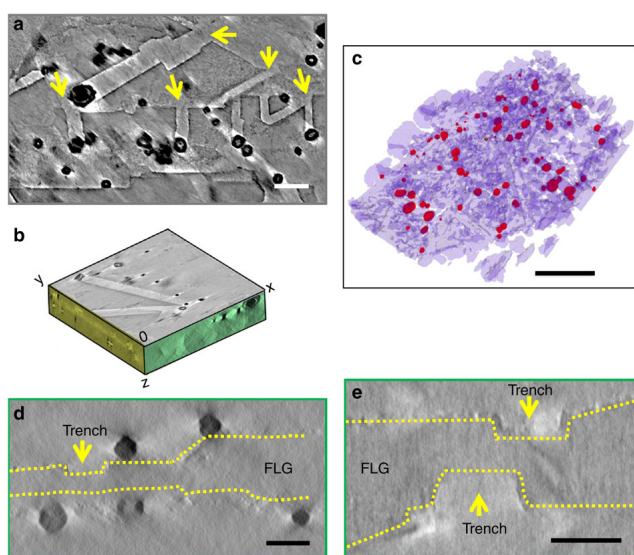


Figure 7.6: a), d) and e) show xy-, xz- and yz-slices of the SIRT reconstruction of the few-layered graphene covered by Fe nanoparticles. Yellow arrows mark the trenches in a), dotted lines in d) and e). b) Representation of the three possible slice directions. c) 3D model derived from the DART reconstruction. Scale bars: a=d=e=20 nm, c=500 nm.²⁵

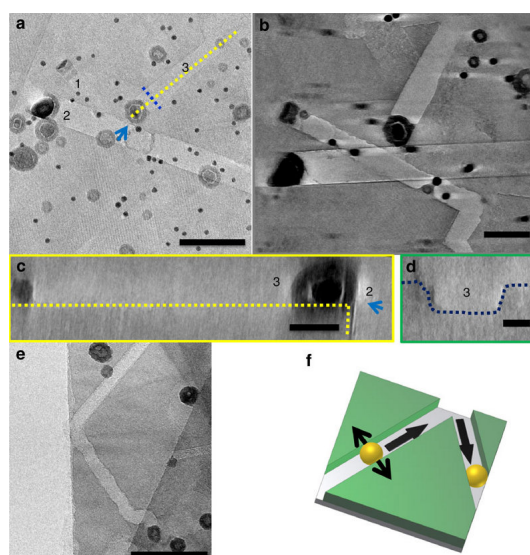


Figure 7.7: a) BF image with b) xy-slice, c) yz-slice and d) xz-slice from the according area. e) BF image displaying the action of an active nanoparticle at a free edge of the graphene. f) Schematic of the interaction forces affecting the Fe nanoparticle near the edge. Scale bars: a=e=50 nm, b=40 nm, c=20 nm, d=10 nm.²⁵

Despite that not all nanoparticles could be reconstructed adequately, and the carbon is not reconstructed perfectly at the edges due to the missing wedge and finite reconstruction volume, most of the particles and the major trenches are visible. Figure 7.6a shows an



xy-slice from the SIRT reconstruction done by the group of Prof. Ersen.²⁵ The trenches have been reconstructed distinctly and are marked by yellow arrows. The nanoparticles obviously cause these trails by reducing carbon to methane, CH₄, acting as catalyst in H₂ atmosphere. Figure 7.6b gives an overview of the different planes (xy, xz and yz) while c) is a model of the DART reconstruction discussed earlier. Figures 7.6d and e display xz-slices of the SIRT reconstruction which demonstrate that it is possible to determine the trenches within the few-layered graphene. A mechanism could be deduced from the electron tomography with regard of the interaction between active nanoparticle catalysts and an adjacent graphene sheet at the same height level. Attractive forces affect the particle at such a step, pulling it close to the sheet. Figure 7.7 shows BF images (a, e) and slices through the reconstruction (b-d), documenting cases of nanoparticles cutting through the graphene layer and reaching another edge of it.²⁵ The interaction is sketched in Figure 7.7f. While opposing edges compensate each other, the particle can change directions when arriving an external facet of the layer, as part of the compensating forces is relieved. In summary, while DART reconstructions can give more precise positions and particle diameter in the given case, SIRT reconstruction is preferable to the analysis of the trenches within the low-density carbon material. Ultimately, the interpretation has to be done manually by an experienced view of the appropriate reconstructions.

Bibliography

- [1] T. K. Sau and C. J. Murphy, "Room temperature, high-yield synthesis of multiple shapes of gold nanoparticles in aqueous solution," *Journal of the American Chemical Society*, vol. 126, no. 28, pp. 8648–8649, 2004.
- [2] C. J. Johnson, E. Dujardin, S. A. Davis, C. J. Murphy, and S. Mann, "Growth and form of gold nanorods prepared by seed-mediated, surfactant-directed synthesis," *Journal of Materials Chemistry*, vol. 12, pp. 1765–1770, 2002.
- [3] K. D. Osberg, M. Rycenga, N. Harris, A. L. Schmucker, M. R. Langille, G. C. Schatz, and C. A. Mirkin, "Dispersible gold nanorod dimers with sub-5 nm gaps as local amplifiers for surface-enhanced raman scattering," *Nano Letters*, vol. 12, p. 3828, 2012.
- [4] C. D'Andrea, J. Bochterle, A. Toma, C. Huck, F. Neubrech, E. Messina, B. Fazio, O. M. Marag, E. Di Fabrizio, and M. Lamy de La Chapelle, "Optical nanoantennas for multiband surface-enhanced infrared and raman spectroscopy," *ACS Nano*, vol. 7, p. 3522, 2013.
- [5] J. Ando, K. Fujita, N. I. Smith, and S. Kawata, "Dynamic SERS imaging of cellular transport pathways with endocytosed gold nanoparticles," *Nano Letters*, vol. 11, p. 5344, 2011.
- [6] T. Shegai, B. Brian, V. D. Miljković, and M. Käll, "Angular distribution of surface-enhanced raman scattering from individual au nanoparticle aggregates," *ACS Nano*, vol. 5, p. 2036, 2011.
- [7] Q. Zhang, N. Large, P. Nordlander, and H. Wang, "Porous Au nanoparticles with tunable plasmon resonances and intense field enhancements for single-particle SERS," *Journal of Physical Chemistry Letters*, vol. 5, p. 370, 2014.
- [8] S. Kawata, "Plasmonics for nanoimaging and nanospectroscopy," *Applied Spectroscopy*, vol. 67, p. 117, 2013.
- [9] M. D. Sonntag, J. M. Klingsporn, L. K. Garibay, J. M. Roberts, J. A. Dieringer, T. Seideman, K. A. Scheidt, L. Jensen, G. C. Schatz, and R. P. Van Duyne, "Single-molecule tip-enhanced raman spectroscopy," *Journal of Physical Chemistry C*, vol. 116, p. 478, 2012.
- [10] W. Srituravanich, N. Fang, C. Sun, Q. Luo, and X. Zhang, "Plasmonic nanolithography," *Nano Letters*, vol. 4, p. 1085, 2004.

- [11] L. Novotny and S. J. Stranick, “Near-field optical microscopy and spectroscopy with pointed probes,” *Annual Review of Physical Chemistry*, vol. 57, p. 303, 2006.
- [12] C. Hrelescu, T. K. Sau, A. L. Rogach, F. Jäckel, and J. Feldmann, “Single gold nanostars enhance raman scattering,” *Applied Physics Letters*, vol. 94, p. 153113, 2009.
- [13] H. DeVoe, “Optical properties of molecular aggregates. I. Classical model of electronic absorption and refraction,” *The Journal of Chemical Physics*, vol. 41, no. 2, pp. 393–400, 1964.
- [14] V. Myroshnychenko, E. Carbó-Argibay, I. Pastoriza-Santos, J. Pérez-Juste, L. M. Liz-Marzán, and F. J. García de Abajo, “Modeling the optical response of highly faceted metal nanoparticles with a fully 3D boundary element method,” *Advanced Materials*, vol. 20, no. 22, pp. 4288–4293, 2008.
- [15] E. M. Perassi, J. C. Hernandez-Garrido, E. E. R. Moreno, M. S. and, E. A. Coronado, and P. A. Midgley, “Using highly accurate 3d nanometrology to model the optical properties of highly irregular nanoparticles: A powerful tool for rational design of plasmonic devices,” *Nano Letters*, vol. 10, p. 2097, 2010.
- [16] A. Zürner, M. Döblinger, V. Cauda, R. Wei, and T. Bein, “Discrete tomography of demanding samples based on a modified SIRT algorithm,” *Ultramicroscopy*, vol. 115, pp. 41 – 49, 2012.
- [17] C. Sorzano, C. Messaoudi, M. Eibauer, J. Bilbao-Castro, R. Hegerl, S. Nickell, S. Marco, and J. Carazo, “Marker-free image registration of electron tomography tilt-series,” *BMC Bioinformatics*, vol. 10, no. 1, p. 124, 2009.
- [18] E. M. Perassi, C. Hrelescu, A. Wisnet, M. Döblinger, C. Scheu, F. Jäckel, E. A. Coronado, and J. Feldmann, “Quantitative understanding of the optical properties of a single, complex-shaped gold nanoparticle from experiment and theory,” *ACS Nano*, vol. 8, no. 5, pp. 4395–4402, 2014.
- [19] A. K. Geim and K. S. Novoselov, “The rise of graphene,” *Nature Materials*, vol. 6, pp. 183–191, 2007.
- [20] K. S. Novoselov, V. I. Fal’ko, L. Colombo, P. R. Gellert, M. G. Schwab, and K. Kim, “A roadmap for graphene,” *Nature*, vol. 94, pp. 192–200, 2012.
- [21] B. F. Machado and P. Serp, “Graphene-based materials for catalysis,” *Catalysis Science & Technology*, vol. 2, pp. 54–75, 2012.
- [22] H. Zhou, C. Qiu, Z. Liu, H. Yang, L. Hu, J. Liu, H. Yang, C. Gu, and L. Sun, “Thickness-dependent morphologies of gold on n-layer graphenes,” *Journal of the American Chemical Society*, vol. 132, no. 3, pp. 944–946, 2010.
- [23] S. S. Datta, D. R. Strachan, S. M. Khamis, and A. T. C. Johnson, “Crystallographic etching of few-layer graphene,” *Nano Letters*, vol. 8, no. 7, pp. 1912–1915, 2008.
- [24] J. I. Agulleiro and J. J. Fernandez, “Fast tomographic reconstruction on multicore computers,” *Bioinformatics*, vol. 27, no. 4, pp. 582–583, 2011.
- [25] G. Melinte, I. Florea, S. Moldovan, I. Janowska, W. Baaziz, R. Arenal, A. Wisnet, C. Scheu, S. Begin-Colin, D. Begin, C. Pham-Huu, and O. Ersen, “A 3D insight on the catalytic nanostructuring of few-layer graphene,” *Nature Communications*, vol. 5, p. 4109, 2014.



Chapter 8

Summary and Outlook

The conclusions that can be drawn from this work are as broad and diverse as its subjects. First of all, it can be stated that TEM proved its value as a reliable tool to obtain in-depth knowledge of a multitude of nanostructures. The crystallization behavior of the anatase nanotubes described in Chapter 4 exhibited some surprising characteristics. Specifically, the large size of crystallites along the tube walls was not expected based on SEM and XRD measurements and could only be deduced by elaborate HRTEM and DF measurements. As the corresponding reduction of grain boundaries within the nanotube walls facilitates charge transport, anodized TiO₂ nanotube arrays should be considered for further implementation in devices. However, the hybrid solar cell presented in this work suffers from several drawbacks. P3HT is a long-chained polymer and thus it is highly challenging to infiltrate it into nanotubes with inner diameters around 30 nm. Additionally, by omitting a suitable dye, light-harvesting has been insufficient to provide significant current density. Yet, these two problems can be conquered, as new organic semiconductors consisting of smaller molecules, like Spiro-OMeTAD, as well as a wide range of new organic dyes are now available. Consequently, further optimization of the TiO₂ nanotubes/dye/organic semiconductor system clearly appears advisable.

A promising alternative to the anodized anatase TiO₂ nanotubes was discussed in Chapters 5 and 6. Rutile TiO₂ nanowires, conveniently fabricated by a one-step hydrothermal process, are valued as electrode materials due to their high aspect ratio and seemingly single-crystalline appearance. However, a detailed analysis of the nanowires by HRTEM and STEM brought to light a peculiar defect structure along the wire cores. Combining the TEM results of conventional sample preparation with those from preparation of a FIB lamella of the wire array, it was possible to detect free internal surfaces running parallel to the {110} lattice planes within the wires. Beyond that, the arrangement of these defects gives rise to a V-shaped cascade of small single-crystalline fingers along the wire core. Based on this evidence it was possible to formulate a growth mechanism of the wires in Chapter 5, which comprises Coulombic repulsion and steric hindrance at the {001} crystal surface present at the tip of the wire during hydrothermal growth.

From there it was only natural to follow up and study the effect of the free internal surfaces on a sample hybrid solar cell device. As described in Chapter 6, a special annealing

treatment was successfully developed to remove the defect structure from the wires. Two distinct annealing steps at varying temperatures were tested, which allowed to understand the influence of an additional TiCl_4 treatment. Such a treatment is normally conducted to obtain a favorable band alignment and an enlarged surface area. HRTEM and STEM measurements were able to show that an annealing step of the wires at $600\text{ }^\circ\text{C}$ removed the free internal surfaces. Depending on the order of the heat treatment, the TiO_2 layer stemming from the TiCl_4 treatment consisted of anatase ($600\text{ }^\circ\text{C}$ annealing before TiCl_4 treatment) or rutile ($600\text{ }^\circ\text{C}$ annealing after TiCl_4 treatment). In the end, the removal of the defects boosted solar cell performance from 2.03 % to 2.71 % peak efficiency. Additionally, the advantage of a rutile-anatase core-shell structure was proven (rutile-rutile nanowire efficiency: 2.53 %). Based on TEM data, solar cell characteristics and PL and PVD live-time measurements, a model for charge transport and loss mechanisms was constructed. The reference cell was only annealed at $450\text{ }^\circ\text{C}$ to reflect the common heat treatment, causing the defects to persist. In this case, the finger structure near the active interfaces prevents electrons from reaching the inner core of the wire, leading to an accumulation of charges near the wire surfaces. At the same time, the free internal surfaces of the fingers provide a multitude of trap states, effectively lowering current density. The nanowire electrode annealed at $600\text{ }^\circ\text{C}$ after TiCl_4 treatment suffers from a transformation of the deposited TiO_2 shell layer from anatase to rutile. Consequently, the alignment of the conduction band is homogeneous, without an additional step near the interface. This leads to the electrons spreading throughout the wire, up to the TiO_2 /dye/P3HT interface, where recombination with adjacently generated holes limits current density. The sample annealed at $600\text{ }^\circ\text{C}$ before TiCl_4 treatment does not feature these detriments, resulting in the aforementioned superior PCEs.

Concluding the work on one-dimensionally nanostructured TiO_2 electrodes, the results of parallel studies which were conducted on other aspects of hybrid solar cells (including doping of electrodes and sensitizing of interfaces) were summarized at the end of Chapter 6. These results should be readily implementable in future solar cells, successfully furthering the quest for considerably improved devices.

Concerning the work done on tomographic reconstructions, it can be concluded that the DART algorithm combined with the masked SIRT algorithm as developed by A. Zürner in 2012 is a powerful tool to reconstruct nanostructures in an outstandingly accurate process. By implementing an algorithm which automates the masking step, as well as additional streamlining, a fast and powerful procedure could be established. A high-quality reconstruction of a gold nanostar was created for the theoretical simulation of its optical response by DDA. This proved successful, as the major characteristics of the actual measurements could be reproduced. As a second project, it was possible to accurately reconstruct the distribution of iron-based nanoparticles on a support of few-layered graphene after catalytic treatment in H_2 atmosphere. For the future it is planned to apply the tomographic procedure to various nanostructured TiO_2 based electrodes. Possible morphologies of interest are single anatase nanotubes for their inner morphology,



and hydrothermally-grown rutile nanowires after the annealing step at 600 °C, as these seem to incorporate a peculiar arrangement of voids presumably stemming from volume released from the free internal surfaces during annealing.

Chapter 9

Addendum

9.1 Cryfinder

Cryfinder is a program which can find possible matches of lattice plane values observed in ED patterns or HR images. Knowing at least two measured lattice plane spacings and the according angle between them, Cryfinder compares them to possible values of a given crystal structure. Figure 9.1 shows the GUI of the program. It uses the crystallographic formulas as found for example in *International Tables for the Determination of Crystal Structures* (IUCr)ⁱ to first calculate a set of possible lattice plane spacings within a given error range. Then it calculates the angles of all respective combinations, including different permutations and directions. This is necessary, as (110) and $(\bar{1}10)$ for example possess the same lattice plane distance but the angle between each of them and (111) will not be the same for crystal symmetries which are more complex than a cubic crystal. A brief overview of version 0.33 is given in figure 9.2. a): The crystal type panel is used to define the crystal system. Possible selections are cubic, tetragonal, orthorhombic, hexagonal, monoclinic, rhombohedral and triclinic. If this is used, panel b) can be used to enter the crystal parameters (size of unit cell and related angles). Alternatively, a preset can be loaded. These are saved in the file `cryfinder_presets.txt` in the Cryfinder folder. In this case, the crystal parameters (b) are fixed.

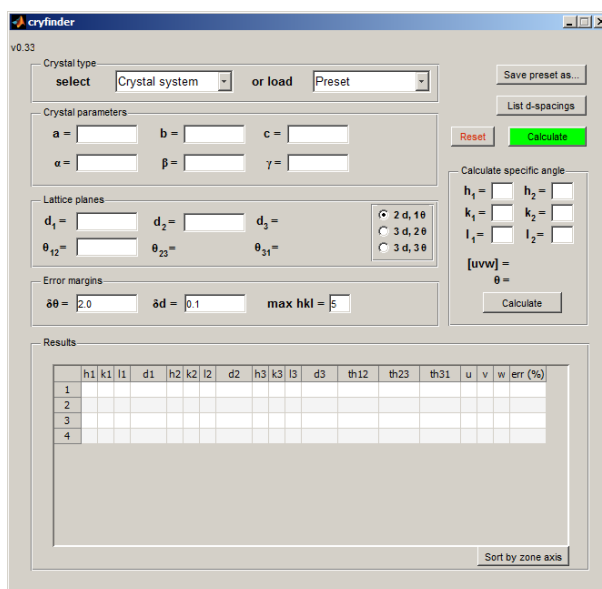
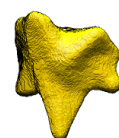


Figure 9.1: The cryfinder GUI.

ⁱ<http://it.iucr.org/>



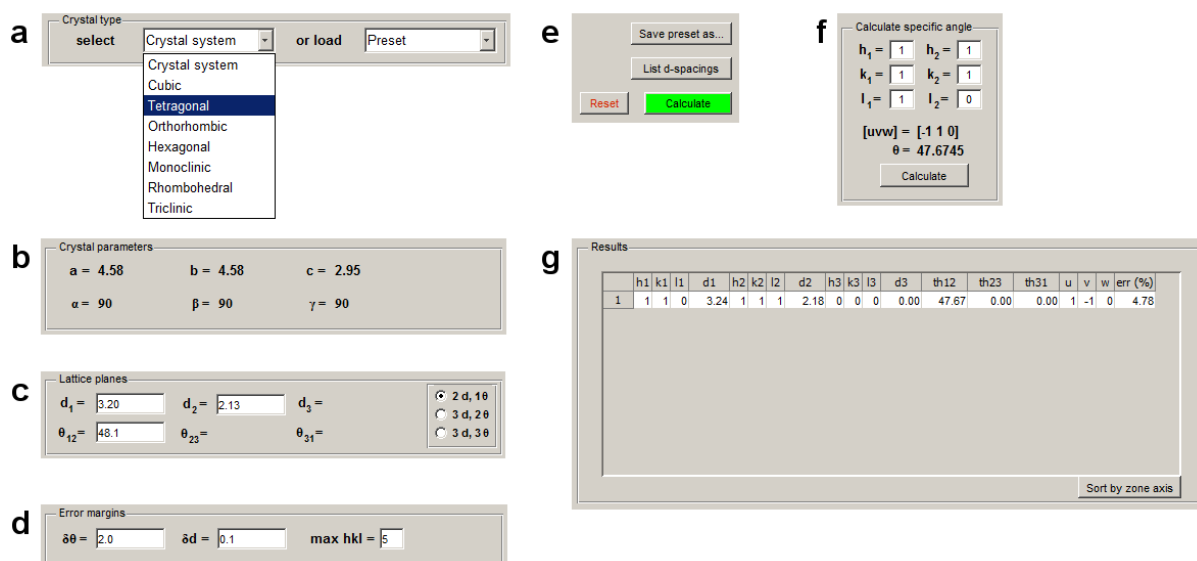


Figure 9.2: Detailed view of the cryfinder GUI. a) Crystal type. b) Crystal parameters. c) Measured lattice planes. d) Error margins. e) Executables. f) Calculation of specific angles. g) Results.

The Lattice planes panel (c) is used to enter the measured distances (d_1 , d_2 , d_3) and angles (Θ_{12} , Θ_{23} , Θ_{31}). More than two distances and one angle can be used to restrict and counter-check the results. d) shows the Error margins panel, where $\delta\Theta$, δd and the highest allowed number for h, k, and l can be varied. e): The button **Save preset as...** is used to include the actual crystal parameters in the preset file (they appear after restarting the program). **List d-spacings** calculates a table of lattice plane spacings, taking into account the **max hkl**-value is taken into account. **Reset** sets the program back to start condition. The green highlighted **Calculate** starts the main calculation, whose results appear in the Results panel (g), showing a set of possible matching values. They are grouped in miller index (**hkl**), the according lattice plane distance (**d**) and the angles between the planes (**th** for Θ). Additionally, the according viewing axis (**uvw**) and an additively calculated percentaged error is given. The results are sorted by this error (ascending) but can alternatively be sorted by order of zone axis ($|u| + |v| + |w|$). The program can also be used to calculate a specific angle between two lattice planes given by their respective miller index (f). The according normal crystallographic axis (or rather viewing axis) is given as well. Additional information about the program can be found in `cryfinder_readme.txt`.

9.2 Step-by-Step Instructions for Tomography

The processing of STEM tilt series for tomography presents a wide range of alternatives, from different alignment methods to reconstruction algorithms, and even a change in sequence may have an impact on the resulting 3D reconstruction. This section is meant to be a suggestion of steps to be performed from the beginning to the end. During this work, the process has been streamlined and a number of algorithms were created to facilitate and speed up the steps. However, as every sample and series is different, changes have to be made where appropriate.

Requirements

These are the requirements for the case of TIA files. The presented version numbers are the ones used in this work. Note that a 64 bit architecture was used. Files which are not further specified might be requested.ⁱⁱ

- Image J *1.45k*ⁱⁱⁱ, including the following:
 - Plugin: TomoJ *2.21*^{iv}
 - Plugin: HandleExtraFileTypes^v
 - Plugin: TIA reader^{vi}
 - Macro: Batch_Convert_TIA.txt
 - Macro: Batch_Convert_TIA_smooth_noscale.txt
 - Macro: Batch_Convert_TIA_smooth_noscale_backgrsubtr.txt
 - Macro: Batch_Convert_TIA_smooth_noscale_backgrsubtr_zero.txt
 - Macro: Batch_Convert_em.txt
 - Macro: Batch_backgroundsubtraction.txt
 - Macro: Batch_convert_em-to-tif.txt
 - Macro: Batch_normalization.txt
 - Macro: Batch_reprojcomparison.txt
- Matlab *7.11.0*^{vii} including
 - Image Processing Toolbox *V6.1*^{viii}
 - Tom toolbox *Release 2008*^{ix}, plus modifications from Andreas Zürner

ⁱⁱ Andreas.Wisnet@cup.lmu.de

ⁱⁱⁱ <http://imagej.nih.gov/ij/>

^{iv} <http://u759.curie.fr/fr/download/software/TomoJ>

^v <http://rsb.info.nih.gov/ij/plugins/file-handler.html>

^{vi} <http://rsb.info.nih.gov/ij/plugins/tia-reader.html>

^{vii} <http://www.mathworks.de/products/matlab/>

^{viii} <http://www.mathworks.de/products/image/>

^{ix} https://www.biochem.mpg.de/278655/tom_e



– Required files/algorithms:

- * `rnm9.m`
- * `setangles.m`
- * `markerssqueeze.m`
- * `mask2go.m`
- * `wholehist.m`
- * `reproj.m`
- * `progressbar.m`

– Optional files/algorithms:

- * `emsortsqueeze.m`
- * `eraseAOI.m`
- * `errloc.m`
- * `getangles.m`
- * `projnormalize.m`
- * `selfilt.m`
- * `subrebg.m`
- * `voldot.m`
- * `volsum.m`
- * `wholeprojhist.m`

- UCSF Chimera 1.8^x or a similar imaging program, like Amira

Series Conversion

Assuming to start with TIA files (.ser ending), the series has to be converted to tif, scaled and renamed:

- ImageJ: Convert series from .ser to .tif (e.g. `Batch Convert TIA smooth noscale`)
- File → Import → Image Sequence...: select folder, scale images as needed (25%, 50%)
- File → Save as → Image Sequence...: save series in right order to `proj_01...proj_xx`
- If angles are irregular create .txt file (one angle per line, order according to the projections)

^x<http://www.cgl.ucsf.edu/chimera/>

Series Preparation and Alignment

Now the series might have to be normalized, background subtracted and aligned:

- ImageJ: Depending on the data, apply **Batch normalization** and/or **Batch backgroundsubtraction**. It is imperative to understand and adapt the macros via `Plugins → Macros → Edit...`
- Now start the TomoJ plugin: `Plugins → TomoJ → TomoJ`
- Either load the file containing the angles or enter them as required
- On tab *Data information* select *normalization type: none* and *Fill blanks with: Zeros*
- On tab *Align tilt series* use the *Translation Correction* and *export aligned images*
- Close the TomoJ plugin and load the file containing the aligned series
- *Crop* the series to the area of interest
- Restart the TomoJ plugin as before and apply the landmark based alignment:
- On tab *Align tilt series* first *generate Landmarks*
- Wait for completion, then *align using 3D landmarks* – these two steps can take very long, depending on projection size and number
- *export aligned images* and close the TomoJ plugin
- Load the landmark-based aligned series again, crop as needed
- Sometimes the background subtraction can only be achieved purposefully after alignment – in this case, apply now
- `File → Save as → Image Sequence...`, again to `proj_01...proj_xx`
- Convert the series to `.em` via **Batch Convert em**

Reconstruction in Matlab

This is the working environment where the actual reconstruction takes place. First, SIRT reconstructions are performed with and without mask to get a starting volume as well as the segmentation of the gray values, then the DART reconstruction is performed. Reprojections can be generated to get a visible comparison and evaluation of the reconstruction quality.

- Matlab: Set working folder the one where the `.em` files are
- `rnm9` will rename the first nine projections from `proj_0x` to `proj_x`



- `setangles` will write the angles into the `.em` files (irregular angles: load file; else set algorithm)
- If an old markerfile (*marker.em*) is available: Run `markersqueeze` to adapt it to the current series; else: Use `tom_setmark` to create a dummy file
- Start `tom_Rec3dGUI`
- Project → Generate Project → singleaxis; follow instructions
- Alignment → No Alignment
- Reconstruction → Set Method
 - Method: `Sirt_neu`
 - Projections: Normalization off
 - Weighting: Apply Weighting off
 - SIRT: Iterations 10-25 (15 is a good start); Pathlength `Slab_org`
- Reconstruction → Do Reconstruction; no shape or starting volume! In case of problems first check/change bit depth of `.tif` files
- Check reconstruction via ImageJ: File → Import → Em reader
- Matlab: `mask2go` will create a mask; for large resolutions use binning to speed it up (can be checked likewise to the preceding step)
- Repeat the Do Reconstruction step; this time load the mask as shape
- `wholehist` generates a histogram from a volume; use it for both reconstructions
- The histogram of the masked reconstruction should contain one or several peaks (cut off 0 at the x-axis to find it) which represent the gray values of the present materials
- `tom_Rec3dGUI`: Reconstruction → Set Method: `DART`, rest as before
- Reconstruction → Do Reconstruction: starting volume should usually be the masked SIRT reconstruction; no shape!
- Matlab command:
 - `s` → Enter
 - Intensität Vakuum: 0
 - Set gray values for present material(s)
 - The none-used material slots should be given gray values far beyond realistic ones, e.g. 50000...

- Segmentation should be roughly 1/2 between grey values
- DART reconstruction will start after last segmentation is entered
- Import file via em reader in ImageJ
- Save as → MRC writer
- This MRC file can be read by UCSF Chimera and Amira
- In Matlab: `reproj` → Choose `.vol` file of the reconstruction(`.vol==.em`)
- In ImageJ: Batch `reprojcomparison` will give a sequence of images to verify the reconstruction quality

Additional Options

This will – in short – explain optional algorithms, all added by separate files.

- `emsortsqueeze`: When some of the projections have to be removed from the `.em` series, `emsortsqueeze` will bring the remaining ones back in order; afterwards use `markersqueeze`!
- `eraseAOI`: This will set the region of interest (pixel intensity above average) to the average; this can be used to reconstruct the environment of particles, create reprojections of this background reconstruction and subtract them from the original projections as a fancy method of background subtraction
- `subrebg`: Subtracts background reprojections (`reproj_xx`; see `eraseAOI`) from the original projections (`proj_xx`)
- `errloc`: This algorithm compares projections and reprojections of a series/reconstruction and gives the deviations from the area of interest and from the background (useful in case of a bad background reconstruction)
- `getangles`: Lists the angles extracted from a `.em` projection series
- `projnormalize`: Normalizes a projection series to its zero projection; useful for bright-field reconstructions
- `selfilt`: This is a crude algorithm which smoothes the background stronger than the area of interest (understand and adjust before usage!)
- `voldot`: Creates the dot product of two volumes and creates an according mask; useful when a mask is alternately iterated by reconstructions
- `volsum`: Gives the sum of two volumes and makes it a mask
- `wholeprojhist`: This creates a histogram of all projections within a folder



Appendix

Publications and Presentations

Publications

Defeating loss mechanisms in 1D TiO₂-based hybrid solar cells

A. Wisnet, K. Bader, S. B. Betzler, M. Handloser, J. Weickert, A. Hartschuh, L. Schmidt-Mende, C. Scheu and J. A. Dorman; submitted to *Advanced Functional Materials*

The effect of Ti(IV) doping on the morphology and optical properties of Nb₃O₇(OH) superstructures

S. B. Betzler, M. Beetz, A. Wisnet, K. Hengge and C. Scheu; in preparation

Unravelling the growth mechanisms of gold nanoplates by liquid transmission electron microscopy

D. Alloyeau, Y. Javed, W. Darchaoui, H. Belkahla, H. Lecoq, S. Ammar, O. Ersen, A. Wisnet, F. Gazeau and C. Ricolleau; to be submitted to *Nanoletters*

Model for hydrothermal growth of rutile wires and the associated development of defect structures

A. Wisnet, S. B. Betzler, R. V. Zucker, J. A. Dorman, P. Wagatha, S. Matich, E. Okunishi, L. Schmidt-Mende and C. Scheu; *Crystal Growth & Design*, **2014**, *14*(9), 4658-4663

Quantitative understanding of the optical properties of a single, complex-shaped gold nanoparticle from experiment and theory

E. M. Perassi, C. Hrelescu, A. Wisnet, M. Döblinger, C. Scheu, F. Jäckel, E. A. Coronado, J. Feldmann; *ACS Nano*, **2014**, *8*(5), 4395-4402

A 3D insight on the catalytic nanostructuring of few-layer graphene

G. Melinte, I. Florea, S. Moldovan, I. Janowska, W. Baaziz, R. Arenal, A. Wisnet, C. Scheu, S. Begin-Colin, D. Begin, C. Pham-Huu, O. Ersen; *Nature Communications*, **2014**, *5*, 4109

Template-free synthesis of novel, highly-ordered 3D hierarchical Nb₃O₇(OH) superstructures with semiconductive and photoactive properties

S. B. Betzler, **A. Wisnet**, B. Breitbach, C. Mitterbauer, J. Weickert, L. Schmidt-Mende and C. Scheu; *Journal of Materials Chemistry A*, **2014**, 2(30), 12005-12013

Control of recombination pathways in TiO₂ nanowire hybrid solar cells using Sn⁴⁺ dopants

J. A. Dorman, J. Weickert, J. B. Reindl, M. Putnik, **A. Wisnet**, M. Noebels, C. Scheu and L. Schmidt-Mende; *Journal of Physical Chemistry C*, **2014**, 118(30), 16672-16679

Cation exchange synthesis and optoelectronic properties of type II CdTe–Cu_{2-x}Te nano-heterostructures

I. Kriegel, **A. Wisnet**, A. R. S. Kandada, F. Scotognella, F. Tassone, C. Scheu, H. Zhang, A. O. Govorov, J. Rodriguez-Fernandez and J. Feldmann; *Journal of Materials Chemistry C*, **2014**, 2(17), 3189-3198

Shedding light on vacancy-doped copper chalcogenides: Shape-controlled synthesis, optical properties, and modeling of copper telluride nanocrystals with near-infrared plasmon resonances

I. Kriegel, J. Rodriguez-Fernandez, **A. Wisnet**, H. Zhang, C. Waurisch, A. Eychmueller, A. Dubavik, A. O. Govorov and J. Feldmann; *ACS Nano*, **2013**, 7(5), 4367-4377

Nanoscale investigation on large crystallites in TiO₂ nanotube arrays and implications for high-quality hybrid photodiodes

A. Wisnet, M. Thomann, J. Weickert, L. Schmidt-Mende and C. Scheu; *Journal of Materials Science*, **2012**, 47(17), 6459-6466

Influence of metallic and dielectric nanowire arrays on the photoluminescence properties of P3HT thin films

M. Handloser, R. B. Dunbar, **A. Wisnet**, P. Altpeter, C. Scheu, L. Schmidt-Mende and A. Hartschuh; *Nanotechnology*, **2012**, 23(30), 305402/1-305402/6

A novel buffering technique for aqueous processing of zinc oxide nanostructures and interfaces, and corresponding improvement of electrodeposited ZnO–Cu₂O photovoltaics

K. P. Musselman, A. Marin, **A. Wisnet**, C. Scheu, J. L. MacManus-Driscoll and L. Schmidt-Mende; *Advanced Functional Materials*, **2011**, 21(3), 573-58

Strong efficiency improvements in ultra-low-cost inorganic nanowire solar cells

K. P. Musselman, **A. Wisnet**, D. C. Iza, H. C. Hesse, C. Scheu, J. L. MacManus-Driscoll and L. Schmidt-Mende; *Advanced Materials*, **2010**, 22(35), E254-E258



Presentations

Tomography

A. Wisnet; *Mechanics meets Energy II, Winterberg, Germany, 01/2014*, Oral Presentation

The intricacies of electron tomography

A. Wisnet, M. Döblinger and C. Scheu; *NIM summer retreat, Lengries-Fall, Germany, 08/2013*, Poster (Best Poster Award)

A reconstruction spree – common problems of tomography

A. Wisnet; *Mechanics meets Energy, Düsseldorf, Germany, 03/2013*, Oral Presentation

Hydrothermal rutile wires - crystal growth and core-shell structures

A. Wisnet, S. B. Betzler, J. Weickert, L. Schmidt-Mende and C. Scheu; *MACAN Thermodynamics Workshop, Istanbul, Turkey, 11/2012*, Poster

An in-depth TEM study of anodized TiO₂ nanotube arrays

A. Wisnet, M. Thomann, J. Weickert, L. Schmidt-Mende and C. Scheu; *MRS Spring Meeting, San Francisco, USA, 04/2012*, Oral Presentation

TEM investigation of material properties of anodized TiO₂ nanotubes

A. Wisnet, M. Thomann, J. Weickert, L. Schmidt-Mende and C. Scheu; *CeNS Workshop, Venice, Italy, 09/2011*, Poster

TEM investigation of nanostructured hybrid solar cells

A. Wisnet, M. Thomann, J. Weickert, F. Gu, M. Döblinger, L. Schmidt-Mende and C. Scheu; *CeNS Workshop, Venice, Italy, 09/2010*, Poster

Curriculum Vitae

Personal Information

Andreas Wisnet
 Place of birth Burghausen
 Nationality German

Education

2010 - 2014 PhD in physical chemistry under supervision of Prof. Christina Scheu at the Ludwig-Maximilians-University, Munich
 2004 - 2010 Studies of Physics at the Ludwig-Maximilians-University, Munich; Degree: Dipl. Physicist (solid-state physics)
 1994 - 2003 Hertzheimer Gymnasium, Trostberg
 General qualification for university entrance (Abitur)

Work Experience

2010 - 2013 Supervision of Diploma and Master theses
 2011 Supervision as part of the NIM summer research program
 2009 - 2012 Tutorships in physical chemistry
 2007 Internship & student worker at the Dr. Johannes Heidenhain GmbH, Traunreut; Conception, construction and programming of control of a wafer prober (XY measuring table & measurement of sensor characteristics)
 2003-2004 Community service at the communal hospital, Trostberg

Skills

Analytics TEM, including CTEM, ED, HRTEM, STEM, EDX, general sample preparation
 Image analysis and processing (TIA, DM, ImageJ)
 Tomographic reconstruction (DART, SIRT)
 Computer languages Matlab (advanced), LabView (advanced), C++ (basics)
 IT administration Support for systems based on Windows
 Languages German (native), English (fluent), French (basics)



Acknowledgments

Well, that was fun.

I don't even know where to start. Maybe like this. No. Anyway. Ok, note the following: There is no particular order, so you will have to read through all of it. Tough luck.

I want to thank Tina. Together with the time I spent on my diploma thesis, it's been more than five years here. And during this time I got all, meaning ALL support from Tina one can wish for. An interesting topic ("A"? More like twenty thousand interesting topics!), scope for development wherever possible, advice whenever needed, fun wheresoever appropriate, bets, drinks, rollercoaster rides, the possibility to visit conferences at nice places featuring great people, and general ties of friendship. Most of all, Tina did support me in every way during some hard times I had to experience. For that, I am infinitely grateful. Thank you.

Speaking of interesting topics, I thank Lukas for all his commitment and many ideas for our projects, for the supervision of my diploma thesis plus seconding the PhD thesis, the feeling that I am working in context of a greater objective, and giving me the possibility to visit Konstanz on a more or less regular basis. Still concerning the interesting topics (who's gonna stop me?), I give a thankful greeting to all the people supplying me with interesting work which I was not able to turn down. ZnO nanowires from Kevin (Cheers to Canada), Cd/Cu₂Te nanoparticles from Ilka (Contamination, yay! Just kidding, was fun!), gold nanostars from Eduardo (my introduction to electron tomography!), a huge load of series for tomography from Ovidiu (we're still working on that) and much other stuff from many other people which we brought to varying levels of success.

To be able to achieve the least of such success, it took a good time of learning and practicing. Thus, I am very grateful that Markus took so much time in teaching us on Jeol and FEI TEMs, as well as giving essential advice on sample preparation and analysis of our data. And of course, a big Thank you! for giving me the chance to delve into the subject of tomography. I drew a huge amount of motivation from that! I also thank Steffen for his tips and tricks on all accounts of electron microscopy, as well as his calm demeanor when something went wrong.

Cheers to all colleagues working at the institute, making it the great place to work at. Especially I have to thank Matze for his friendship and advice, the possibility to let off steam and to be brought back to earth whenever the need arose.

Now I'll have to try not to forget anyone. I thank all of you who were daring enough to let yourself be supervised by me. Markus, who was at my side at the beginning of my PhD thesis, acting as a colleague and friend, closing ranks as physicists among chemists. Sophi - I am really proud of you. When the idea came up that you'd do some synthesis under my supervision I was a little doubtful that I could help you, but you made best use of the loose guidelines I gave you. Each time it was a pleasure to take a look at the

new marvels you brought to me. Alena, I am happy you could learn something here, if not from me, then at least from Sophi. ;) Have fun with tomography! And Derya, Franzi and Peter - thanks for your help, I hope you had some fun here. I certainly did.

Regards to the group formerly known as "Hybrid Nanostructures" in Munich, now operating under the name "Hybrid Nanostructures" in Konstanz (wait, what?) - I was always happy to stroll among physicists, watching them doing chemistry. I am still sad that some of our brilliant ideas were turned down by panicked chemists (like HF under pressure at high temperatures...). James, it's been a real pleasure to work with you. It is great to bounce ideas back and forth, especially when they are founded on our similar attitude towards our work! Jonas - you are amazing. I admire you for the constant pushing regarding the scientific progress. You want to do (or by now, get people doing it! ;)). I was sorry seeing you leave towards Konstanz early during our conjoint work, as it's always been a joy working face-to-face with you.

I am not done with rambling, yet! So, I thank all my co-workers of our group. You all know how lucky we were to build this companionship. Angi (fighting beside me from the beginning), Teresa, Ramona, Christoph, Christian, Sriram, Andrea, Anna, Stephan, Katha, and all others who were part of the group at some time. Alex, I was happy to find a like-minded person down there in the basement, who's every now and then holding me in check when my ideas get out of hand. At last, I sincerely thank Rachel for the great atmosphere she adds to our office. Finding the best - fitting! - Shakespearean phrase for a scientific subject is just hilarious.

I also have to thank my friends, always giving me motivating comments (HA!), with a special focus on my former flatmates, Andi and Kata & Michi, and David! My parents (all of them!), who always supported me in my decisions and gave me the possibility to do the things I really wanted to do. My sister, being closely connected as ever.

An incredibly big thank you is reserved for Kathrin, who kept me grounded throughout the last ten years at the university. Thank you. This is beyond words.

It is marvelous seeing this work, considering that I had thought I never finish anyth



